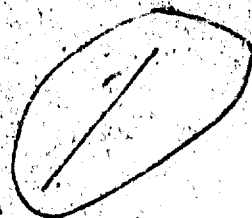


AD699218

RESEARCH DIRECTED TOWARD THE STUDY AND ANALYSIS OF ELECTROSTATIC ANALYZER DATA



by WILLIAM P. REIDY

AMERICAN
SCIENCE 
AND ENGINEERING

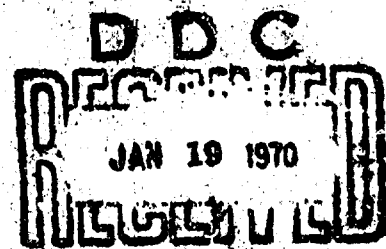
11 CARLETON STREET, CAMBRIDGE, MASSACHUSETTS 02142

CONTRACT NO. F19628-68-C-0287

PROJECT NO. 000D, 5710

TASK NO. 000D63

WORK UNIT NO. 000D6301



FINAL REPORT

PERIOD COVERED: 5 MARCH 1968 THROUGH 15 JULY 1969

15 AUGUST 1969

THIS DOCUMENT HAS BEEN APPROVED FOR PUBLIC
RELEASE AND SALE; ITS DISTRIBUTION IS UNLIMITED.

CONTRACT MONITOR: JOHN A. SANDOCK
IONOSPHERIC PHYSICS LABORATORY

THIS RESEARCH WAS SUPPORTED IN PART BY THE DEFENSE ATOMIC SUPPORT AGENCY
AND IN PART BY THE AIR FORCE IN-HOUSE LABORATORY INDEPENDENT RESEARCH FUND.

PREPARED FOR

AIR FORCE CAMBRIDGE RESEARCH LABORATORIES
OFFICE OF AEROSPACE RESEARCH
LAURENCE G. HANSCOM FIELD BEDFORD, MASSACHUSETTS 01730

AFCRL-69-0369

RESEARCH DIRECTED TOWARD THE STUDY AND
ANALYSIS OF ELECTROSTATIC ANALYZER DATA

by

William P. Reidy

American Science and Engineering
11 Carleton Street, Cambridge, Massachusetts 02142

Contract No. F19628-68-C-0287

Project No. 000D, 5710

Task No. 000D63

Work Unit No. 000D6301

Final Report

Period covered: 5 March 1968 - 15 July 1969

15 August 1969

This document has been approved for public
release and sale; its distribution is unlimited.

Contract Monitor: John A. Sandock
Ionospheric Physics Laboratory

This research was supported in part by the Defense Atomic Support Agency
and in part by the Air Force In-House Laboratory Independent Research Fund.

Prepared for

AIR FORCE CAMBRIDGE RESEARCH LABORATORIES
OFFICE OF AEROSPACE RESEARCH
LAURENCE G. HANSCOM FIELD
BEDFORD, MASSACHUSETTS 01730

Qualified requestors may obtain additional copies from the Defense Documentation Center. All others should apply to the Clearinghouse for Federal Scientific and Technical Information.

ABSTRACT

Section I - The OV3-2 satellite was instrumented with two electron electrostatic analyzers to measure the auroral electron spectrum between 10 and 100 kev, the electron pitch angle distribution, and the precipitated electron flux. The design and calibration of these instruments are documented. Initially the satellite measurements were tape recorded and played back at selected recording stations. After failure of the recording and playback system, real time recordings were made at Churchill and Thule. The analysis of this data is presented; including spectral form, spatial distribution, and limited pitch angle distributions.

Section II - Aerobee rocket 15.735 was instrumented with a high resolution ($\Delta E = 1E$) rapid (300 milliseconds per energy sweep) to measure the auroral electron spectrum between 2 and 35 kev and a thin window ionization chamber to measure the total energy deposition. The rocket was launched during the breakup of a visible aurora and penetrated a diffuse auroral region. The energy spectra temporal variation, and the variation in pitch angle distribution as a function of energy are presented.

TABLE OF CONTENTS

	<u>Page</u>
FOREWORD	
PART I - OV 3-2 Electron Spectral Measurements	1
1.0 INTRODUCTION	1
1.1 Experimental Objectives	1
1.2 Present Status of Analysis	1
2.0 INSTRUMENTATION	3
2.1 Description	3
2.2 Preflight Calibration	13
2.2.1 Plate Transmission and Geometric Factor	18
2.2.2 Calibration of Scintillator and Photomultiplier	22
2.2.3 Electronic Calibration Curves	22
2.3 Preflight and Inflight Performance and Sensitivity	45
2.4 Orbital Parameters	51
3.0 DATA REDUCTION AND ANALYSIS	59
3.1 Tape Recorded Data	59
3.2 Real Time Transmission in the Auroral Zone	71
3.3 Spatial Distribution	81
PART II - Rocket Measurements of Auroral Electrons	85
1.0 INTRODUCTION	85
2.0 INSTRUMENTATION	87

3.0	DATA REDUCTION AND ANALYSIS	91
	REFERENCES	103
APPENDIX A	Satellite Measurements of Low Energy Electrons	
APPENDIX B	Correlated Satellite and Ground Based Measurements from the OV3-2 Satellite and Churchill Research Range	
APPENDIX C	Coordinated Measurements from Two Multi- Experiment Rockets in an Aurora	
APPENDIX D	Charged Particle Transmission Through Spherical Plate Electrostatic Analyzers	

LIST OF ILLUSTRATIONS

PART I - OV 3-2 Spectral Measurements

<u>Figure</u>	<u>Page</u>
2.1 Analyzer and Logic Unit	4
2.2 \pm 15 KV Power Supply Unit	5
2.3 Analyzer and Logic Unit, Mechanical Layout	6
2.4 \pm 15 KV Power Supply Unit, Mechanical Layout	7
2.5 Electrostatic Analyzer Assembly Photograph	8
2.6 Electrostatic Analyzer Assembly Block Diagram	10
2.7 Electrostatic Analyzer Electronic Schematic	11
2.8 Orientation of ESA Units in OV 3-2 Satellite	12
2.9 Orientation of Magnetometer in OV 3-2 Satellite	16
2.10 Orientation of Solar Sensor in OV 3-2 Satellite	17
2.11 Electrostatic Analyzer Angular Transmission Response	20
2.12 Electrostatic Analyzer Energy Transmission Response	21
2.13 + 6.75 Volt Calibration SO-1	24
2.14 - 6.75 Volt Calibration SO-1	25
2.15 + 6.75 Volt Calibration SO-2	26
2.16 - 6.75 Volt Calibration SO-2	27
2.17 + 6.75 Volt Calibration SO-3	28
2.18 - 6.75 Volt Calibration SO-3	29
2.19 Photomultiplier High Voltage Calibration SO-1	30
2.20 Photomultiplier High Voltage Calibration SO-2	31
2.21 Photomultiplier High Voltage Calibration SO-3	32

<u>Figure</u>		<u>Page</u>
2.22	Log Current Amplifier Calibration SO-1	33
2.23	Log Current Amplifier Calibration SO-2	34
2.24	Log Current Amplifier Calibration SO-3	35
2.25	Positive Plate Equivalent Energy SN-5	36
2.26	Negative Plate Equivalent Energy SN-5	37
2.27	Positive Plate Equivalent Energy SN-6	38
2.28	Negative Plate Equivalent Energy SN-6	39
2.29	Positive Plate Voltage and Monitor Oscilloscope Trace SN-5	40
2.30	Negative Plate Voltage and Monitor Oscilloscope Trace SN-5	41
2.31	Positive Plate Voltage and Monitor Oscilloscope Trace SN-6	42
2.32	Negative Plate Voltage and Monitor Oscilloscope Trace SN-6	43
2.33	Oscilloscope Trace Calibration	44
2.34	Strip Chart Record Initial ESA Turn-on in Orbit	49
2.35	Minimum Detectable Flux	53
2.36	Sketch of ESA Orientation	54
2.37	Orbital Parameters THBAR ($\bar{\theta}$) and THETA (θ) as Function of Time	56
2.38	Orbital Parameters FIOSP ($\bar{\psi}$) and PHBAR ($\bar{\phi}$) as Function of Time	57
3.1	Strip Chart Record Playback orbit 101/102 - Record orbit 90	62
3.2	Electron Flux Measurements Playback orbit 101/102 - Record orbit 90	64
3.3	Composite Flux and Pitch Angle Dependence Sweep 2	65

<u>Figure</u>		<u>Page</u>
3.4	Composite Flux and Pitch Angle Dependence Sweep 3	66
3.5	Differential Energy Spectra Real Time Orbit 5817	79
3.6	Distribution of Electron Measurements in Local Time and Geomagnetic Latitude	82

PART II - Rocket Measurements of Auroral Electrons

<u>Figure</u>		<u>Page</u>
3.1	Rocket Trajectory	92
3.2	Rate of Energy Deposition and Pitch Angle (Ion Chamber)	93
3.3	Energy Flux and Pitch Angle (Electrostatic Analyzer)	94
3.4	Energy Spectra at 30° Pitch Angle	96
3.5	Energy Spectra at 64° and 150° Pitch Angle	97
3.6	Rate of Energy Deposition in Selected Energy Intervals (ESA)	98
3.7	Pitch Angle Distribution at 5, 10, 20, and 30 keV (ESA)	100
3.8	Pitch Angle Distribution at 2 and 3 keV (ESA)	101
3.9	Pitch Angle Distribution of Total Energy Flux (Ion Chamber)	102

FOREWORD

This is the final report for Contract F19628-68-C-0287. This contract is directed to the initial analysis of rocket and satellite measurements of the electron energy spectra in auroras. Part I of this report is devoted to the OV3-2 satellite measurements. The rocket measurements are discussed in Part II.

Appendixed to this report are reprints of four technical papers related to this work.

- A. "Satellite Measurements of Low Energy Electrons in the Auroral Regions" by E.R. Hegblom, W.P. Reidy, and J.A. Sandock.
- B. "Correlated Satellite and Ground Based Measurements from the OV3-2 Satellite and Churchill Research Range" by J.A. Sandock and E.R. Hegblom.
- C. "Coordinated Measurements from Two Multi-Experiment Rockets in an Aurora" by J.C. Ulwick, K.D. Baker, and E.R. Hegblom.
- D. "Charged Particle Transmission Through Spherical Plate Electrostatic Analyzers" by F.R. Paolini and G.C. Theodoridis.

The work was performed under the technical direction of Mr. John A. Sandock, Ionospheric Perturbations branch, Air Force Cambridge Research Laboratories and was sponsored by the Office of Aerospace Research with Air Force In-House Laboratory Independent Research Funds. The assistance of Dr. E. Richard Hegblom, Space Data Analysis Laboratory, Boston College, is gratefully acknowledged.

PART I

OV 3-2 ELECTRON SPECTRAL MEASUREMENTS

1.0 Introduction

1.1 Experimental Objectives

The OAR OV 3-2 Satellite was launched on 28 October 1966 into a polar orbit (82° inclination). The apogee/perigee was 1600/325 kilometers. Perigee at launch was 15° N and the position of perigee shifted northward approximately 3° per day. The spin rate was 4 rpm and the satellite initially had negligible precession. Part I of this report is devoted to the analysis of the electron spectra obtained with two electrostatic analyzers flown on this satellite.

The purpose of this experiment was to measure the low-energy electron spectra and angular distributions near the auroral zones and to analyze the fore and aft asymmetries in the angular distributions of the electrons to determine the trapped and precipitated fluxes. Two electrostatic analyzers whose fields of view are 180° apart were used to make this measurement. Each instrument was designed to measure the energy spectrum over the approximate energy range of 8 - 100 keV with an energy resolution of about 7%. The angular aperture was $8^\circ \times 20^\circ$ and the geometric factor was about $.05 \text{ cm}^2\text{-ster}$. Sweeping the voltage on the analyzer plates in a period of ten seconds measured the energy spectrum. The instrument sensitivity was sufficient to measure electron fluxes of the type associated with intense Class 1 or brighter auroras.

1.2 Present Status of Analysis

Data from the OV 3-2 Satellite were taped recorded on-board and subsequently readout by ground station command during the period from

launch (28 October 1966) to 22 February 1967, when the recording and playback system failed. During this period data were obtained for 60 orbits out of a possible 1636. The selection of recorded orbits was determined by Air Force operational requirements unrelated to this experimental program. Of these 60 orbits, measurable electron fluxes were observed on approximately half. Because of problems with the spacecraft clock and onboard magnetometer, it has been difficult to obtain a proper merge of the ephemeris and data. A satisfactory merge is required to obtain accurate pitch angle distributions, to calculate the energy precipitated into the auroral regions, and to map out the location of the auroral regions. To date a satisfactory merge has been obtained on ten orbits with measurable electron fluxes. The analysis of this data has been delayed by this problem and for this reason some of the results in this report are preliminary. The tape recorded data is presented in Section 3.1, Part I.

Subsequent to the failure of the tape recording and playback system, arrangements were made with the Churchill Research Range to record real time transmissions from the satellite and to make simultaneous ground based auroral measurements. This cooperative effort which has extended from the spring of 1967 to the present has greatly increased the scientific value of this program. Since this data is obtained in real time, there is no problem in obtaining a proper merge. However, after a period of 11 months in orbit, the ESA plate power supplies appear to have degraded. The Churchill real time data and a method for analyzing the measurements in the degraded mode are discussed in Section 3.2, Part I.

Preliminary results obtained with the tape recorded data were presented at the 49th annual meeting of the American Geophysical Union. The real time measurements were discussed at the 1968 AGU Winter Meeting. These papers are included as Appendix A and B to this report.

2.0 Instrumentation

2.1 Description

Under contract AF 19(628)-2814, three electron electrostatic analyzers (ESA) were delivered to the Air Force Cambridge Research Laboratories. Each analyzer consisted of two major subassemblies--the analyzer and logic unit and the power supply unit. Two of the analyzers were flown on the OV 3-2 satellite. The third unit was a spare. The three ESA units are identified by subassembly serial number in Table 2.1 below.

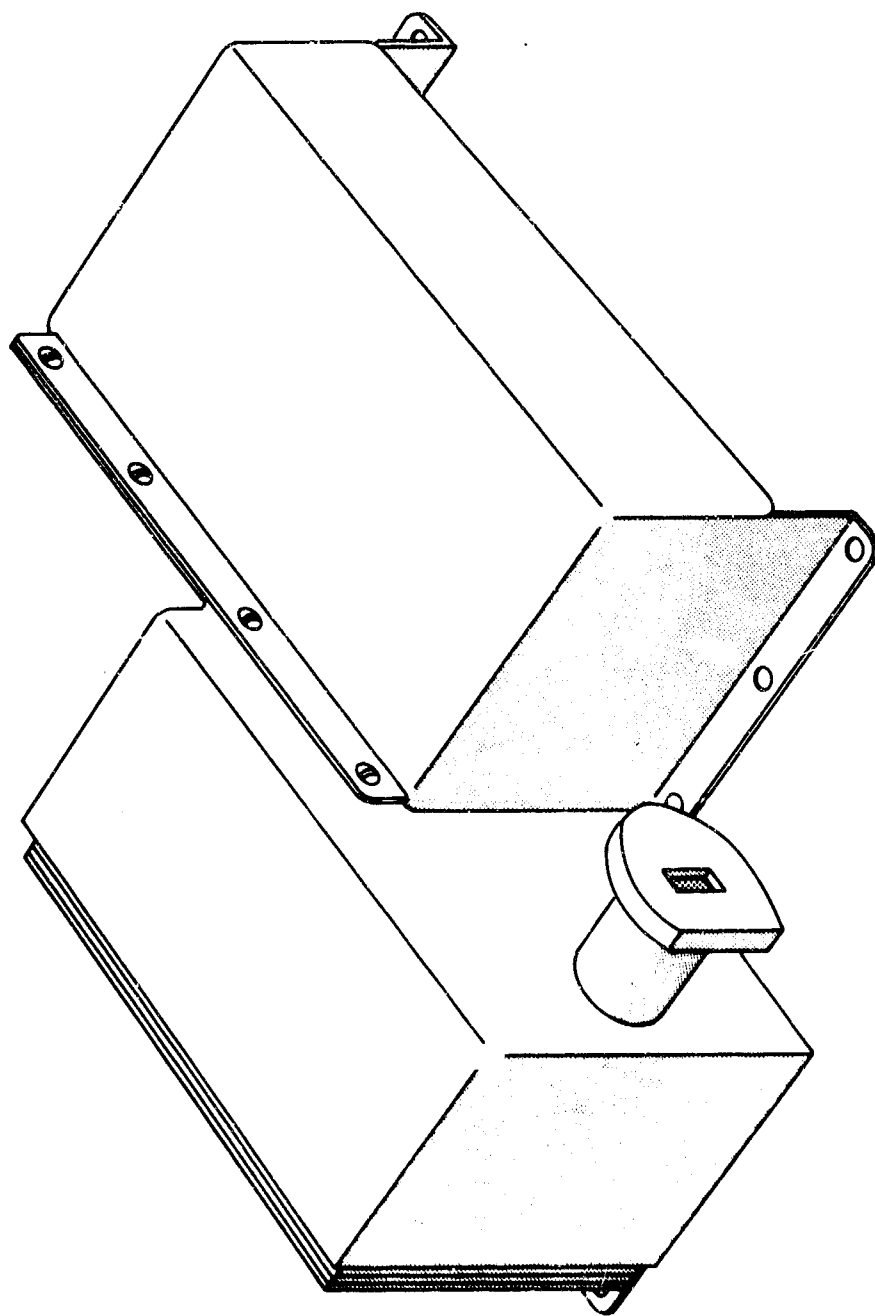
TABLE 2.1

SERIAL NUMBER FOR ESA COMPONENTS

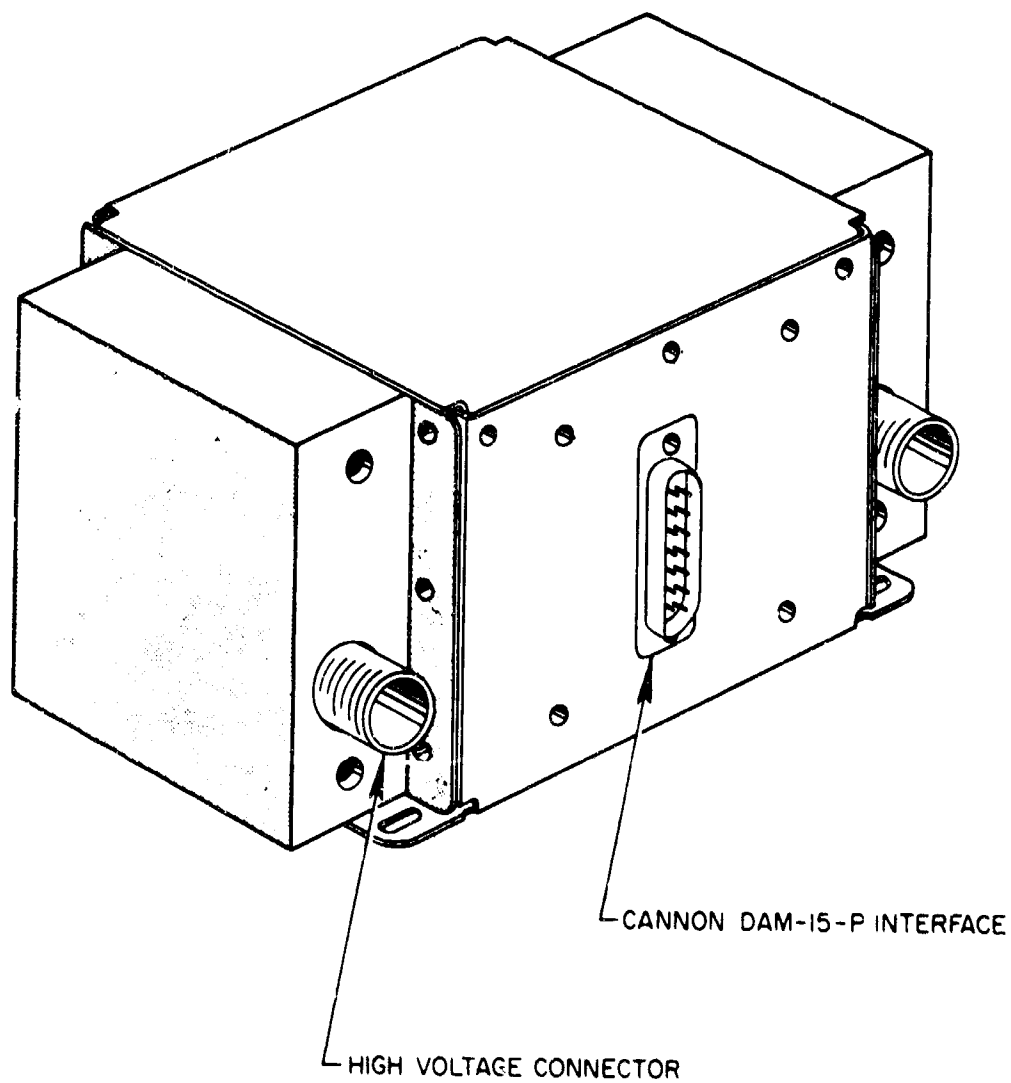
<u>ESA</u>	<u>Analyzer & Logic Unit</u>	<u>Power Supply Unit</u>
1	SO-3	SN-5
2	SO-2	SN-6
3 (Spare)	SO-1	SN-4

Figures 2.1 and 2.2 are representations of the analyzer and logic unit and the power supply unit, respectively. Mechanical layouts of these units are presented in Figures 2.3 and 2.4. Figure 2.5 is a photograph of one analyzer detector - high voltage supply combination. This is a typical mounting configuration for satellite use.

The electrostatic analyzer utilizes a concentric pair of spherical quadrants for spectral analysis; the spherical geometry is used to achieve three-dimensional focusing and reasonably large angular aperture. The



ANALYZER & LOGIC UNIT

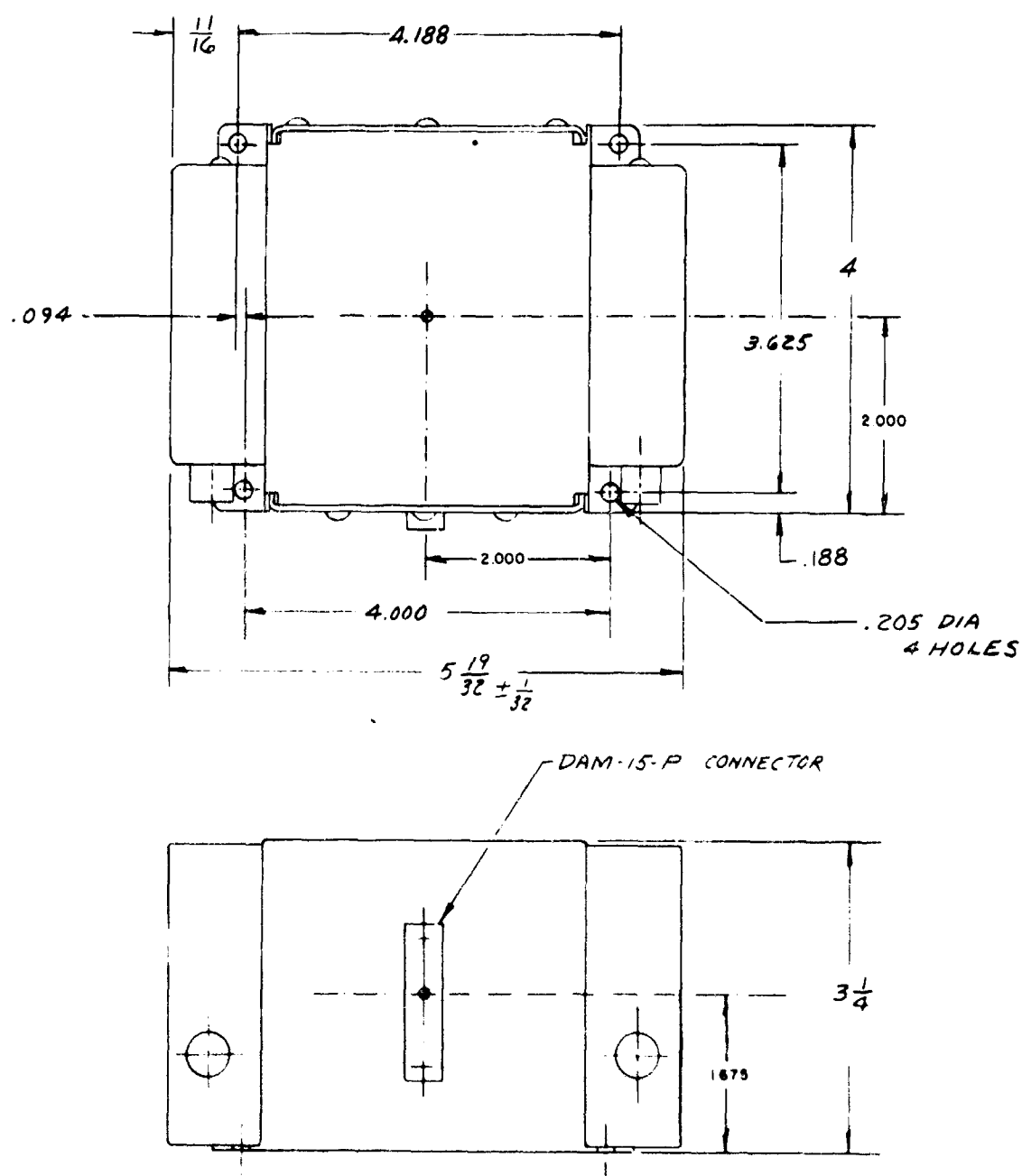


$\pm 15\text{KV}$ POWER SUPPLY UNIT

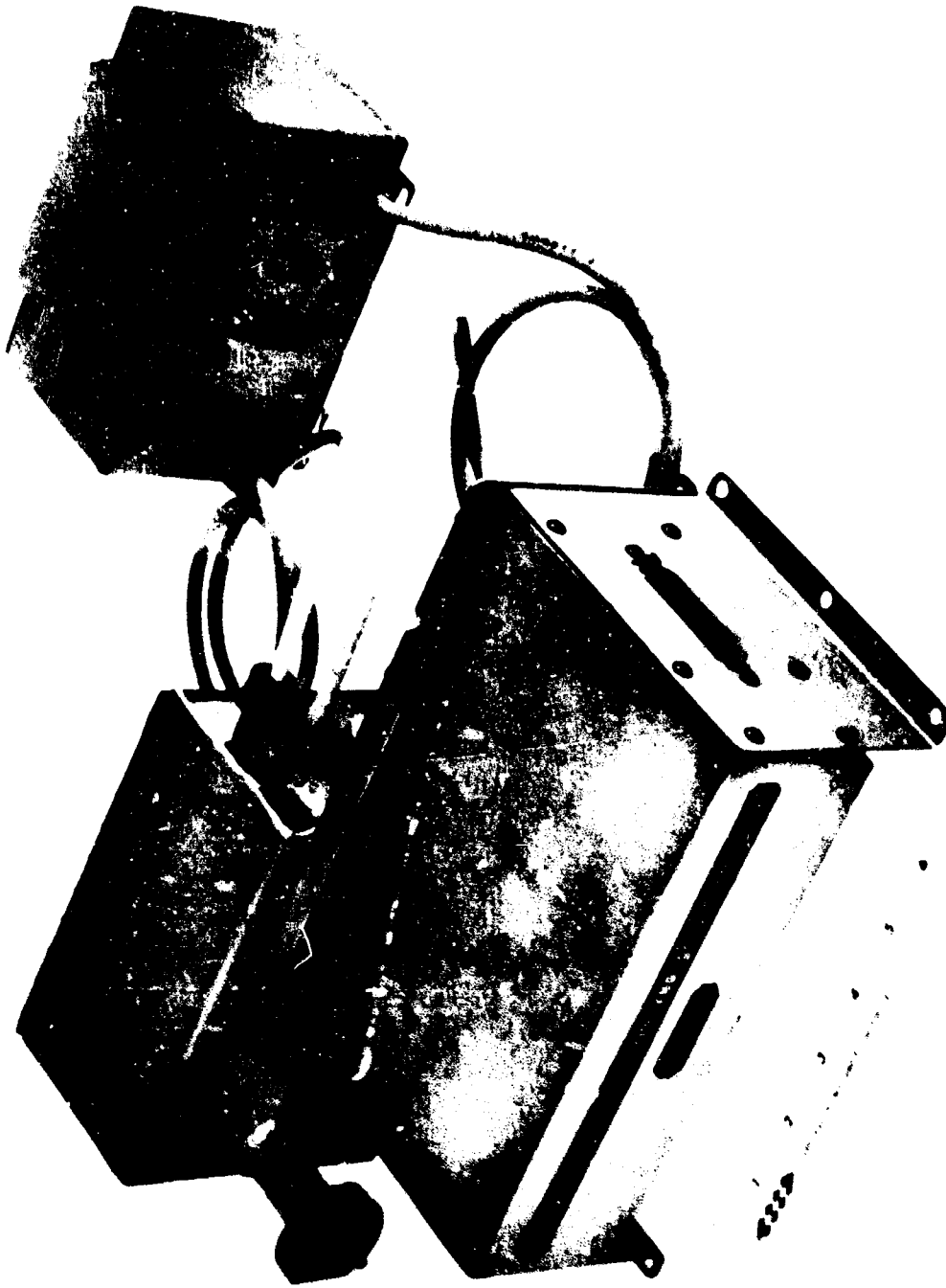
[illegible]

ANALYZER AND LOGIC UNIT MECHANICAL LAYOUT

±15KV POWER SUPPLY UNIT MECHANICAL LAYOUT



NO. 3255-13



CC-029

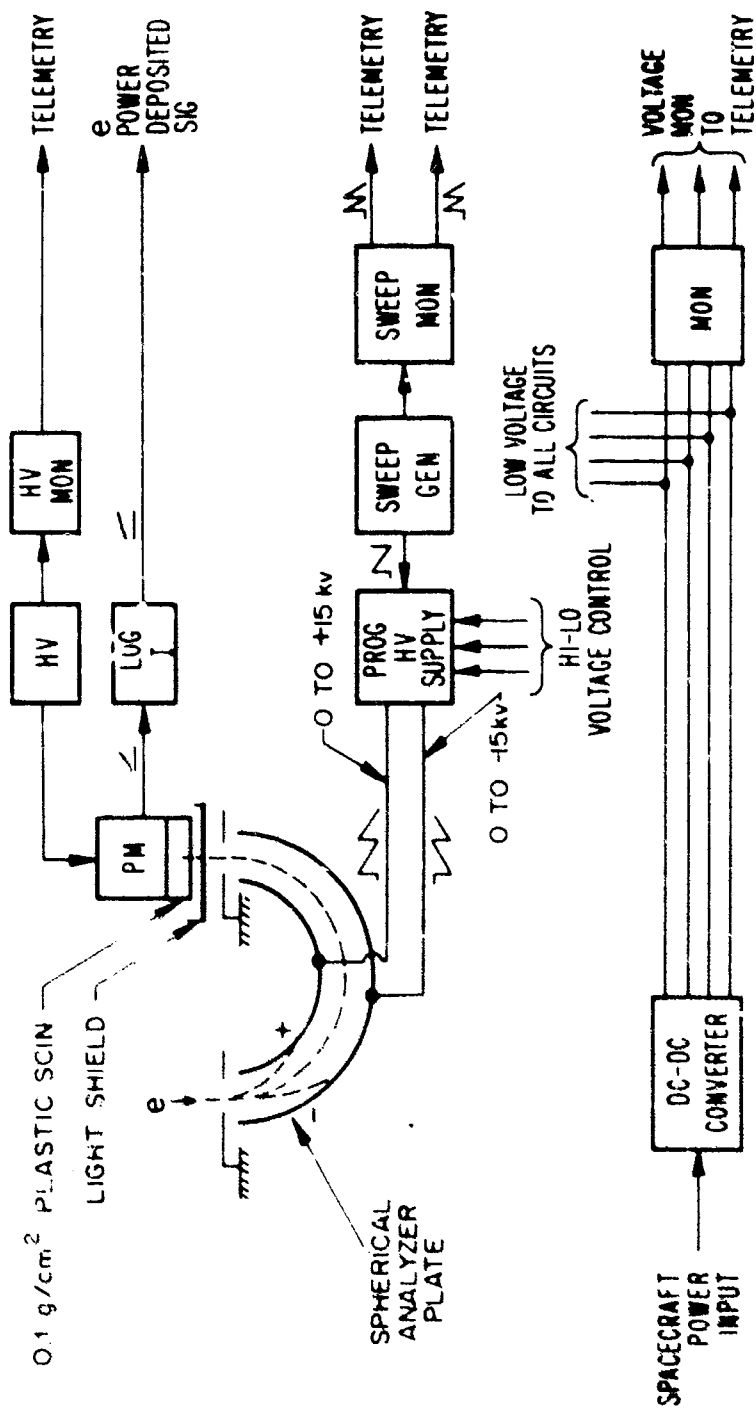
ELECTROSTATIC ANALYZER ASSEMBLY

relationship between the separation of the plates, ΔR ; the geometrical mean radius of spheres, \bar{R} ; the mean energy (electron volts) of the particle focused, E , and the magnitude of the voltage applied to each plate, V (i. e., one plate is at $+V$ and the other at $-V$ volts) is given by $E = 2V\bar{R}/\Delta R$. The energy resolution is given approximately by $\Delta R/2\bar{R}$ (FWHM), and for the present instruments, is about 7 percent. A detailed analysis of the properties of spherical electrostatic analyzers is included as Appendix D to this report. (This work was performed under a separate contract Air Force Contract F19628-67-C-0277).

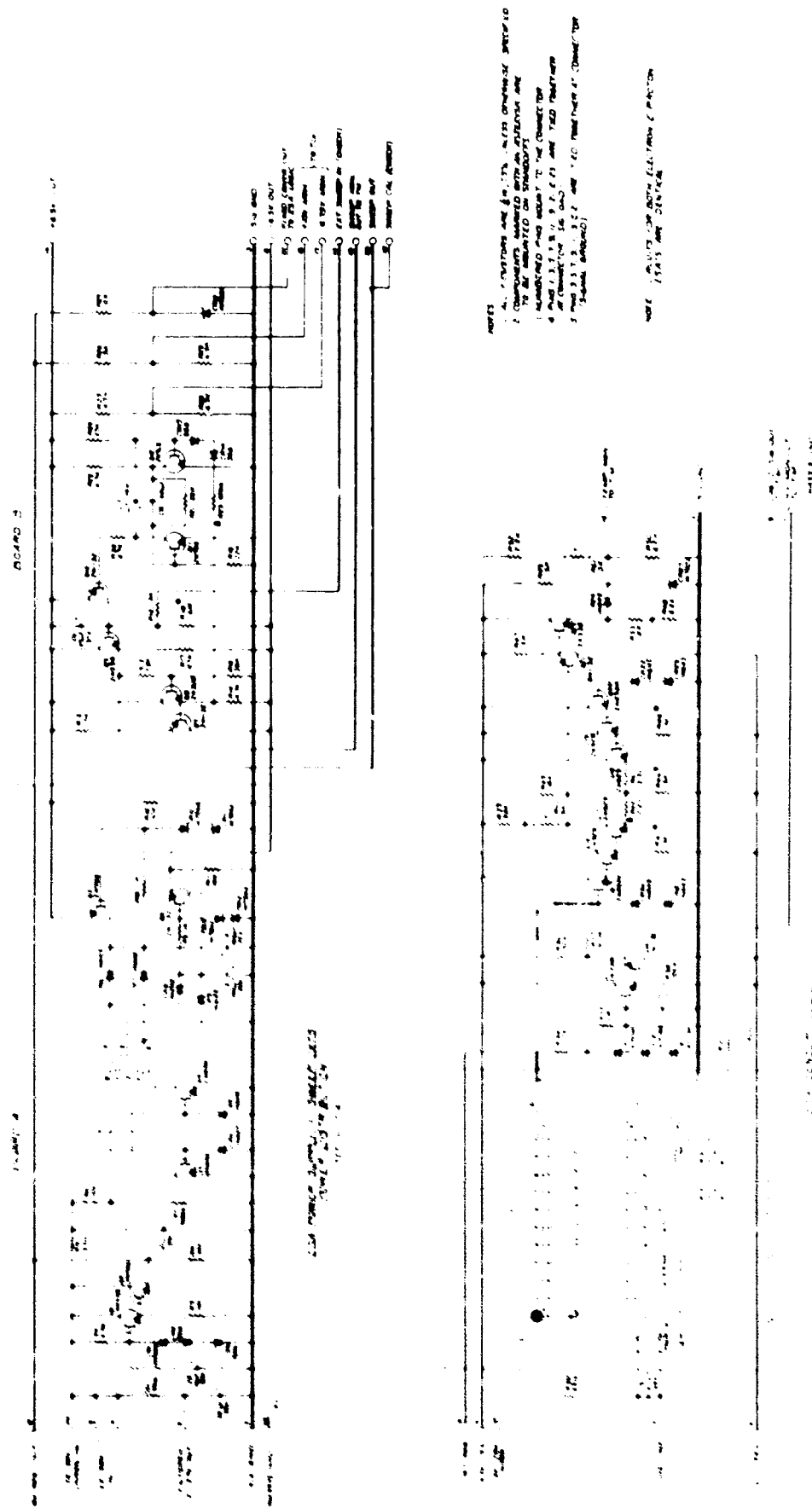
Figure 2.6 is a block diagram of one electrostatic analyzer and associated high voltage supply. A linear sweep voltage (saw-tooth) of about 10-second period is applied to a control circuit of a programmable high voltage supply with balanced positive and negative outputs which are tied to the separate plates of the analyzers. Monitoring the sweep provides knowledge of the high voltage outputs; the equation $E = 2V\bar{R}/\Delta R$ (which is verified by direct instrument calibration) then gives the energy to which the analyzers are set at any time.

The detection system employs a Pilot "B" plastic scintillator covered by 2000 Å of aluminum deposited as a light shield and viewed by a photomultiplier (RCA type 4441A); energy loss in the light shield is less than 8 keV. The current output of the photomultiplier is proportional to the rate-of-energy deposition in the scintillator. A logarithmic current to voltage converter is used to condition the signal for telemetry and to obtain a large dynamic range. The energy of the incident particles can be immediately derived by monitoring the sweep. A complete electronic schematic is shown in Figure 2.7.

The instrumentation was flown on the OV 3-2 satellite. The satellite is spin stabilized and the instrumentation was mounted such that the axis of the acceptance cone for each instrument was in the plane normal to the spin axis and the two instruments were looking 180° apart. Figure 2.8 shows

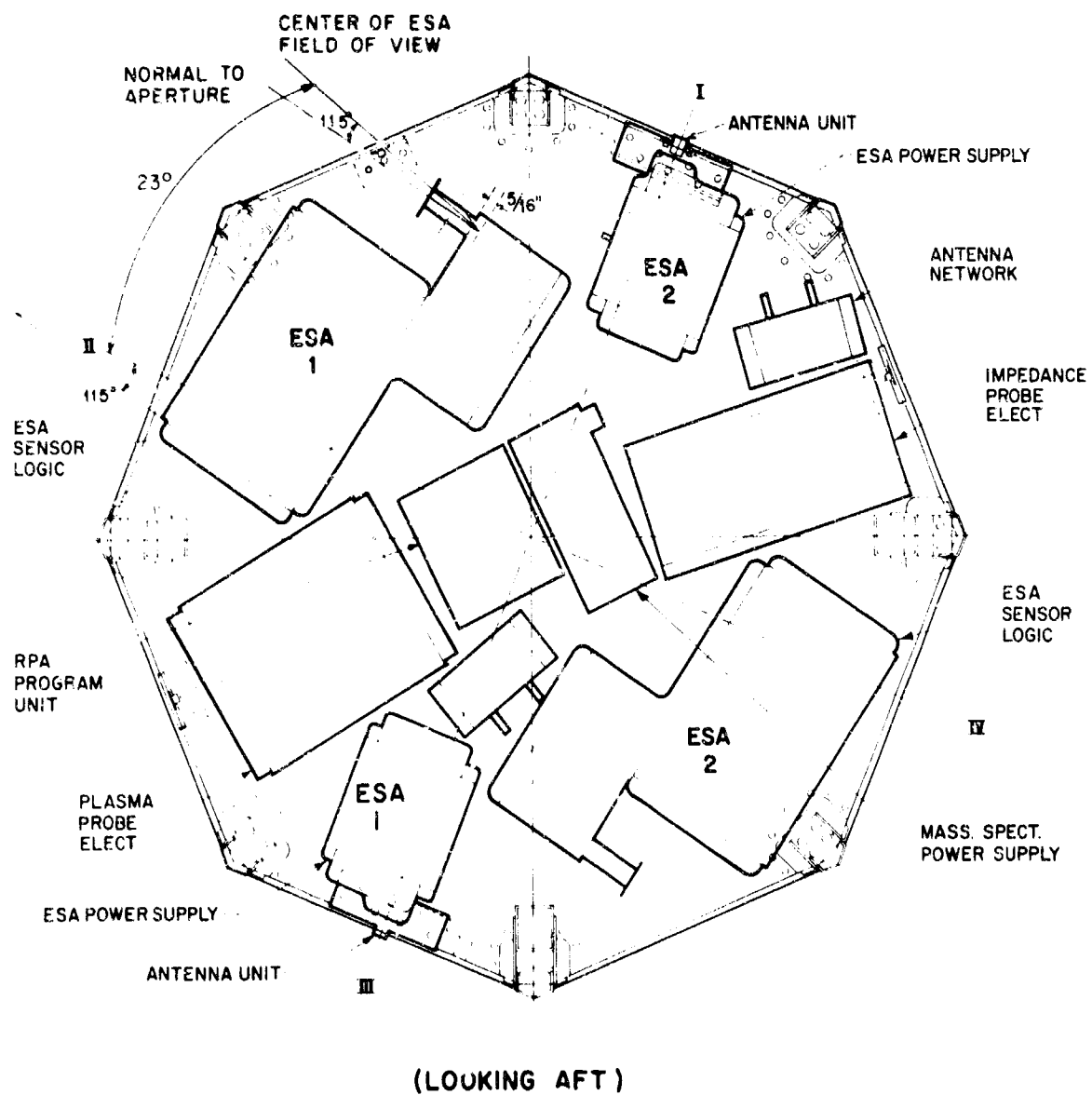


ELECTROSTATIC ANALYZER BLOCK DIAGRAM



ELECTROSTATIC ANALYZER SCHEMATIC

ORIENTATION OF ESA UNITS IN OV 3-2 SATELLITE



the mechanical layout of the ESA units with respect to the II/IV axis which is used as a orientation reference on the spacecraft.

The data from the electrostatic analyzer is sampled by a 1 x 120 commutator and telemetered to the ground in real time or stored on tape for subsequent transmission. Table 2.2 identifies the commutator segments applicable to this instrument.

The output signal from the analyzer logic unit, which is the primary data, is sampled 10 times a second; the other data is sampled once a second which is sufficient to establish the electron energy and to monitor proper operation.

In the analysis of the data, aspect was determined from magnetic and solar aspect data. Figure 2.9 and 2.10 show the orientation of the magnetometers and solar sensors with respect to the spacecraft.

2.2 Preflight Calibration

The output data signal from the analyzer logic is a 0-5V signal which is proportional to the logarithm of the output current from the photomultiplier. This in turn is proportional to the photomultiplier gain, the rate of energy deposition in the scintillator, the scintillator efficiency, the efficiency for light collection at the photocathode, and the photocathode photoelectric efficiency. If V is the signal as recorded on telemetry and $\epsilon_{(E)}$ is the rate at which energy is deposited in the scintillator then

$$V = k_1 + k_2 \ln[I_n + \epsilon_{(E)} \xi G]$$

where k_1 and k_2 are constants determined by the amplifier

I_n is the photomultiplier dark current

ξ is the current produced at the photocathode per unit energy deposited in the scintillator (ξ combines the scintillator

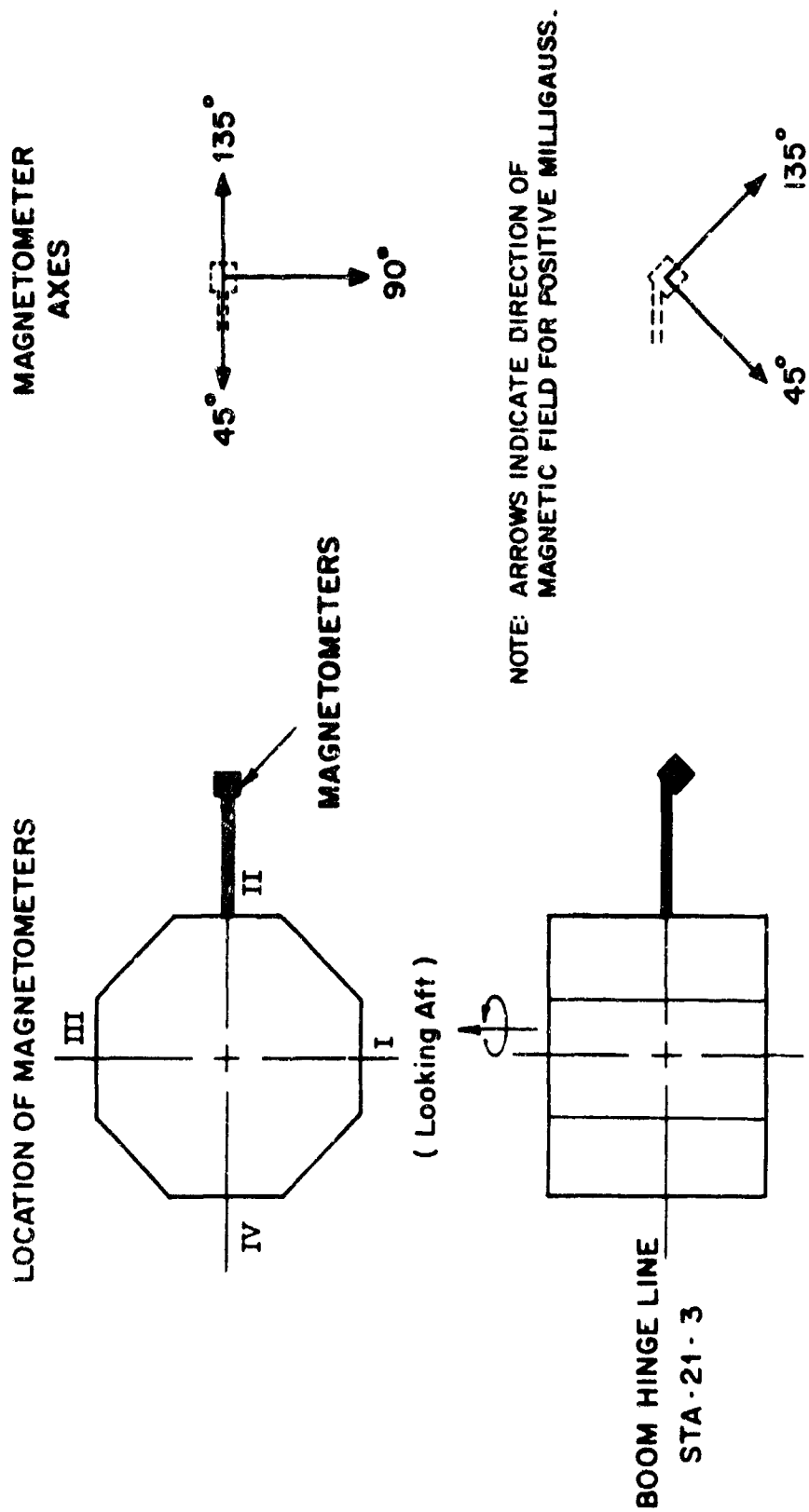
TABLE 2.2

IDENTIFICATION OF ESA COMMUTATOR SEGMENTS
ON OV 3-2 PAYLOAD (1 x 120 COMMUTATOR)

<u>Segment</u>	<u>Function</u>
6	ESA #1 Photomultiplier Current
7	ESA #2 Photomultiplier Current
8	ESA #1 Positive Analyzer Plate Voltage Monitor
9	ESA #1 Negative Analyzer Plate Voltage Monitor
16	ESA #1 Photomultiplier Current
17	ESA #2 Photomultiplier Current
32	ESA #1 Photomultiplier Current
33	ESA #2 Photomultiplier Current
34	ESA #1 -6.75 Volt Monitor
46	ESA #1 Photomultiplier Current
47	ESA #2 Photomultiplier Current
54	ESA #2 -6.75 Volt Monitor
55	ESA #1 Photomultiplier Current
56	ESA #2 Photomultiplier Current
68	ESA #1 Photomultiplier Current
69	ESA #2 Photomultiplier Current
70	ESA #1 Photomultiplier High Voltage Monitor
71	ESA #2 Photomultiplier High Voltage Monitor
78	ESA #1 Photomultiplier Current
79	ESA #2 Photomultiplier Current
80	ESA #1 +6.75 Volt Monitor

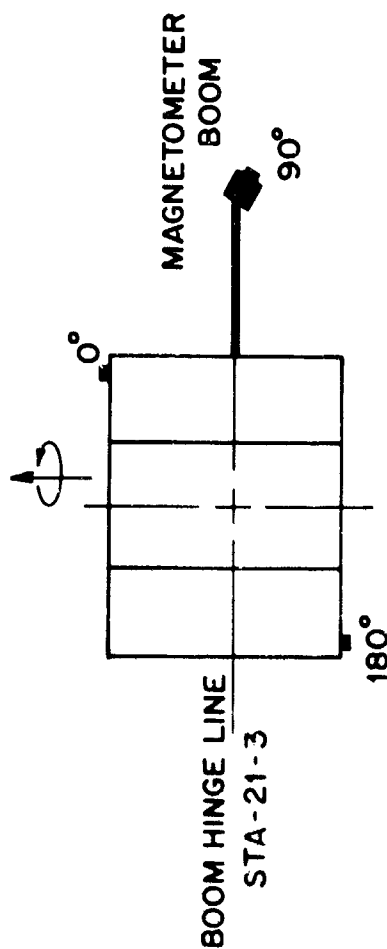
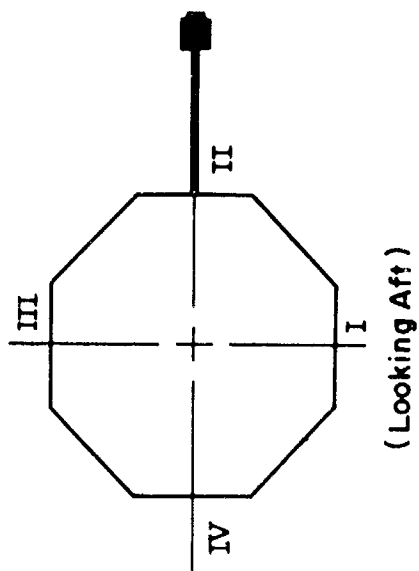
TABLE 2.2 (Continued)

<u>Segment</u>	<u>Function</u>
87	ESA #1 Photomultiplier Current
88	ESA #2 Photomultiplier Current
89	ESA #2 Positive Analyzer Plate Voltage Monitor
90	ESA #2 Negative Analyzer Plate Voltage Monitor
97	ESA #1 Photomultiplier Current
98	ESA #2 Photomultiplier Current
99	ESA #2 + 6.75 Volt Monitor
107	ESA #1 Photomultiplier Current
108	ESA #2 Photomultiplier Current



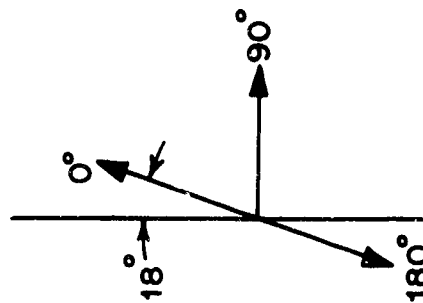
OV-3 MAGNETOMETER ORIENTATION

LOCATION OF SOLAR SENSORS



SOLAR SENSOR AXES

NOTE: ARROWS INDICATE AXES OF SOLAR SENSORS AND DIRECTIONS IN WHICH THEY POINT. AXES ARE PARALLEL TO THE PLANE FORMED BY THE II-IV AND SPIN AXES.



OV-3 SOLAR SENSOR ORIENTATION

efficiency, the efficiency for light collection at the photocathode, and the photocathode efficiency.)

G is the photomultiplier gain

The quantity $\mathcal{E}_{(E)}$ represents the energy carried by the portion of the incident electron flux $N(E)$ which is transmitted by the analyzer plates,

$$\mathcal{E}_{(E)} = \int_E \int_{\alpha_1} \int_{X_1} T(E, \alpha_1, X_1) E N(E) dE d\alpha_1 dX_1$$

where E , α_1 , X_1 represent the energy, angular direction and position in the aperture plane for the incident electron, $N(E)$ is the differential electron intensity $(\text{cm}^2\text{-sec-ster-eV})^{-1}$.

The discussion of the electrostatic analyzer calibration can be conveniently divided into three parts;

1. Plate transmission and geometric factor, which is expressed by the relationship between $\mathcal{E}_{(E)}$ and $N(E)$.
2. Calibration of the scintillator photomultiplier response expressed by ξG .
3. Calibration of the various electronic circuits (e.g., amplifiers, monitors, sweep voltages, etc.).

2.2.1 Plate Transmission and Geometric Factor

The transmission characteristics for analyzer plates geometrically similar to the ones used in this program have been measured by Theodoridis and Paolini. A paper on this work which was performed under Air Force Contract F19628-67-C-0277 is included as Appendix D to this report.

According to Paolini and Theodoridis, the transmission integral is independent of X_1 . Using this and the fact that $EN(E)$ can be considered constant over the narrow differential their results are equivalent to

$$\mathcal{E} = AEN(E)\Delta\beta \int T(E, \alpha = 0^\circ) dE \int T(E = E_{\max}, \alpha) d\alpha$$

where $T(E, \alpha = 0^\circ)$ and $T(E = E_{\max}, \alpha)$ are respectively the transmission functions measured with a pencil beam as a function of energy at normal incidence and as a function of angle at the energy of peak transmission. These response functions have been measured with analyzer plates identical to that flown on the OV 3-2 satellite and are shown in Figures 2.11 and 2.12. α is defined as the angle between the normal to the plate entrance aperture (\vec{n}) and the projection of the electron velocity vector into the plane containing that normal and the center of the spherical plates as shown in Figure 2.11. α_0 is a fixed reference angle in the calibration measurement. For β , the orthogonal angle, the response is limited by a collimating slit. For this instrument $\Delta\beta$ is 10° fullwidth half maximum. Using the data in Figures 2.11 and 2.12 one can numerically evaluate the expression for \mathcal{E}

Rewriting the above equation

$$\mathcal{E} = EN(E)A\Omega E$$

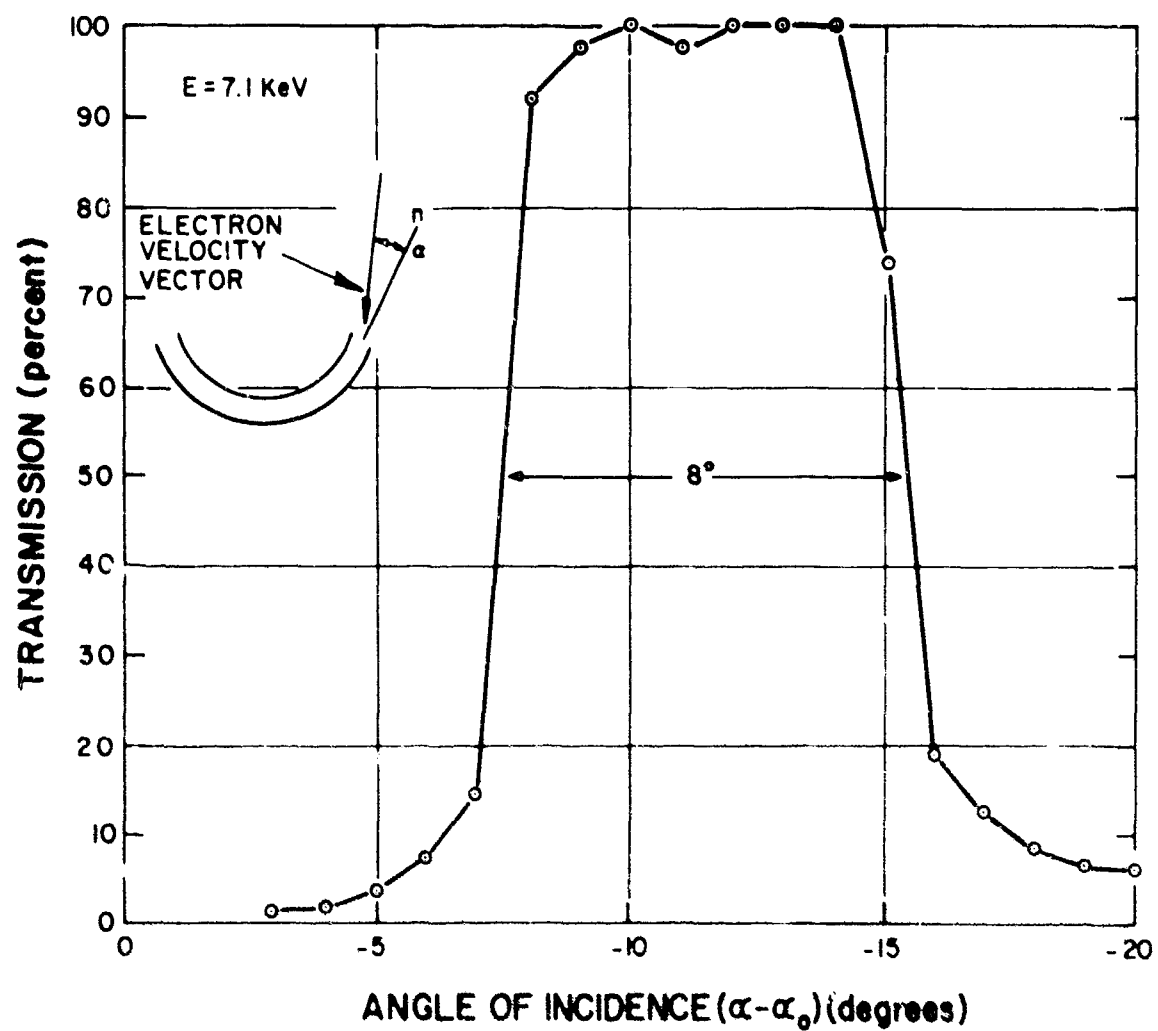
where $A = 1 \text{ cm}^2$

$$A\Omega = A\Delta\beta \int T(E = E_{\max}, \alpha) d\alpha = 4.9 \times 10^{-2} \text{ cm}^2 \text{ ster}$$

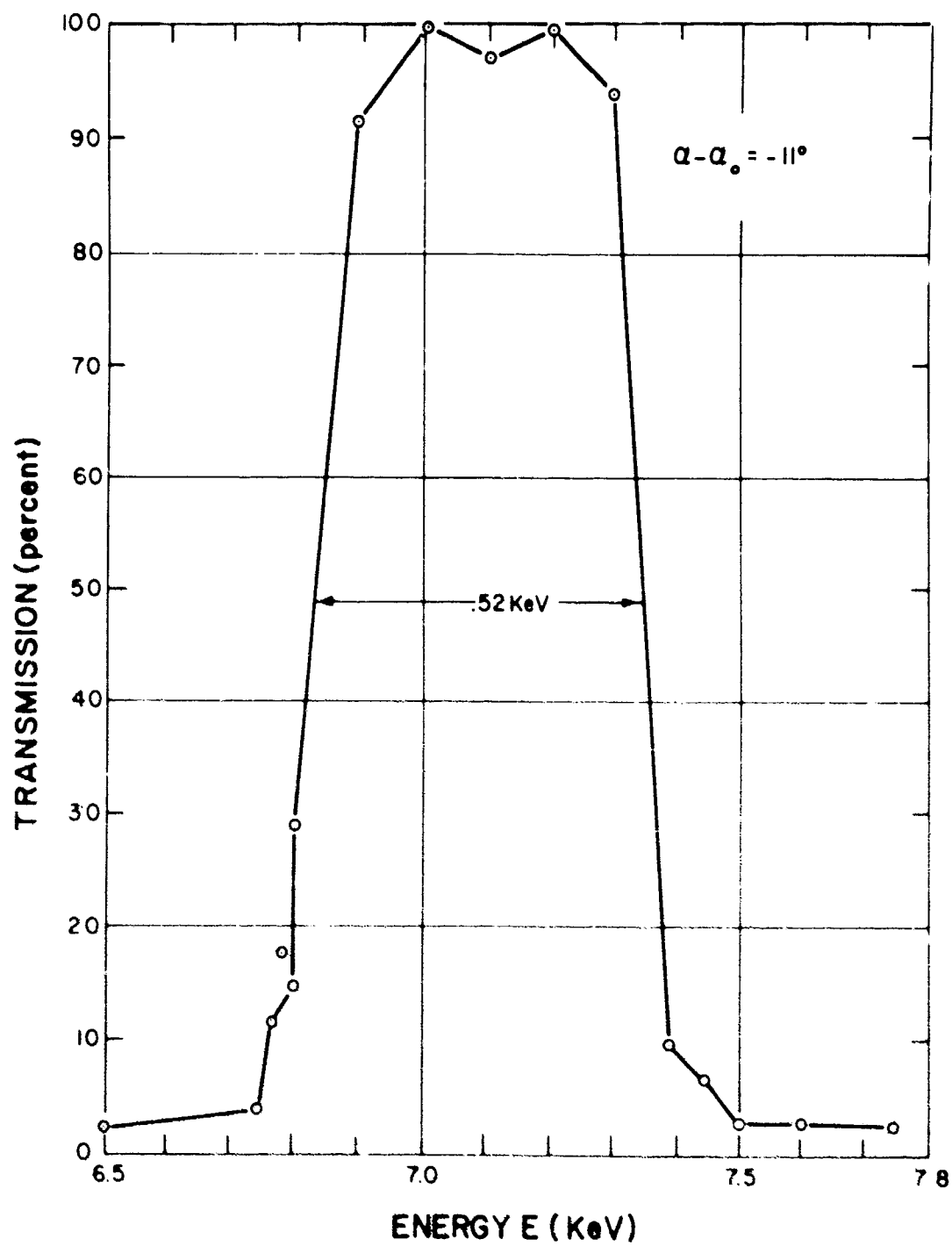
$$\Delta E = \int T(E, \alpha = 0^\circ) dE = .073 E$$

In this expression we have not taken into account the energy loss in the aluminum deposition covering the scintillator. The corrected formula is

ELECTROSTATIC ANALYZER ANGULAR TRANSMISSION RESPONSE



ELECTROSTATIC ANALYZER ENERGY TRANSMISSION RESPONSE



$$\mathcal{E} = (E - E_L) N(E) A E$$

where E_L is the average energy loss per electron calculated from the measured aluminum thickness on the basis of the work of Kanter and Sternglass⁽¹⁾.

2.2.2 Calibration of Scintillator and Photomultiplier

The scintillator photomultiplier portion of the detector was calibrated using assayed Am^{241} sources. The measured response was corrected for the difference in scintillator response to α particles and electrons as discussed by Paolini et al⁽²⁾. Each unit was calibrated at its normal operating voltage. The second column is the ratio of output current of the photomultiplier to rate of energy deposition in the scintillator at normal operating voltage

Analyzer and Logic Unit	Amperes/watt
SO-1 (spare)	56
SO-2 (ESA-2)	14
SO-3 (ESA-1)	56

2.2.3 Electronic Calibration Curves

Calibration measurements of all telemetered and housekeeping circuits were made prior to delivery of the instrumentation.

Figures 2.13 through 2.18 are the calibration curves for the plus and minus 6.75 volt (input power) monitor for the three Analyzer and Logic Units.

Figures 2.19 through 2.21 show the calibration curves for the photomultiplier high voltage monitor of each Analyzer and Logic Unit. The temperature variation in the photomultiplier high voltage monitor output of SO-2 is shown in Figure 2.19. Figure 2.22 through 2.24 gives the calibration curves for the current to voltage amplifiers used to measure the photomultiplier current for each of the Analyzer and Logic units.

Figures 2.25 through 2.28 show the monitor voltage as a function of plate equivalent energy for Power Supply Units SN5 and SN6 which are the two units flown on the satellite. The sum of the positive and negative equivalent energies are equal to the electron energy at the center of the energy band pass to which the analyzer is set.

Figures 2.29 through 2.32 are reproductions of oscilloscope traces showing the relative behavior of each plate high voltage and its monitor as a function of time. The oscilloscope measures the plate high voltage through a resistor divider chain. The relationship between the plate high voltage and the voltage measured by the oscilloscope through the resistor divider is shown in Figure 2.33.

In the calculation for the incident flux using the calibration data in Section 2.2 the effective area of SO-2 had to be reduced by a factor of 1/3 to compensate material overlapping on the scintillator face. With this correction included the relation between photomultiplier anode current and incident flux (N electrons $\text{cm}^{-2} \text{ster}^{-1} \text{sec}^{-1} \text{ev}^{-1}$) for the two units flown on OV3-2 is

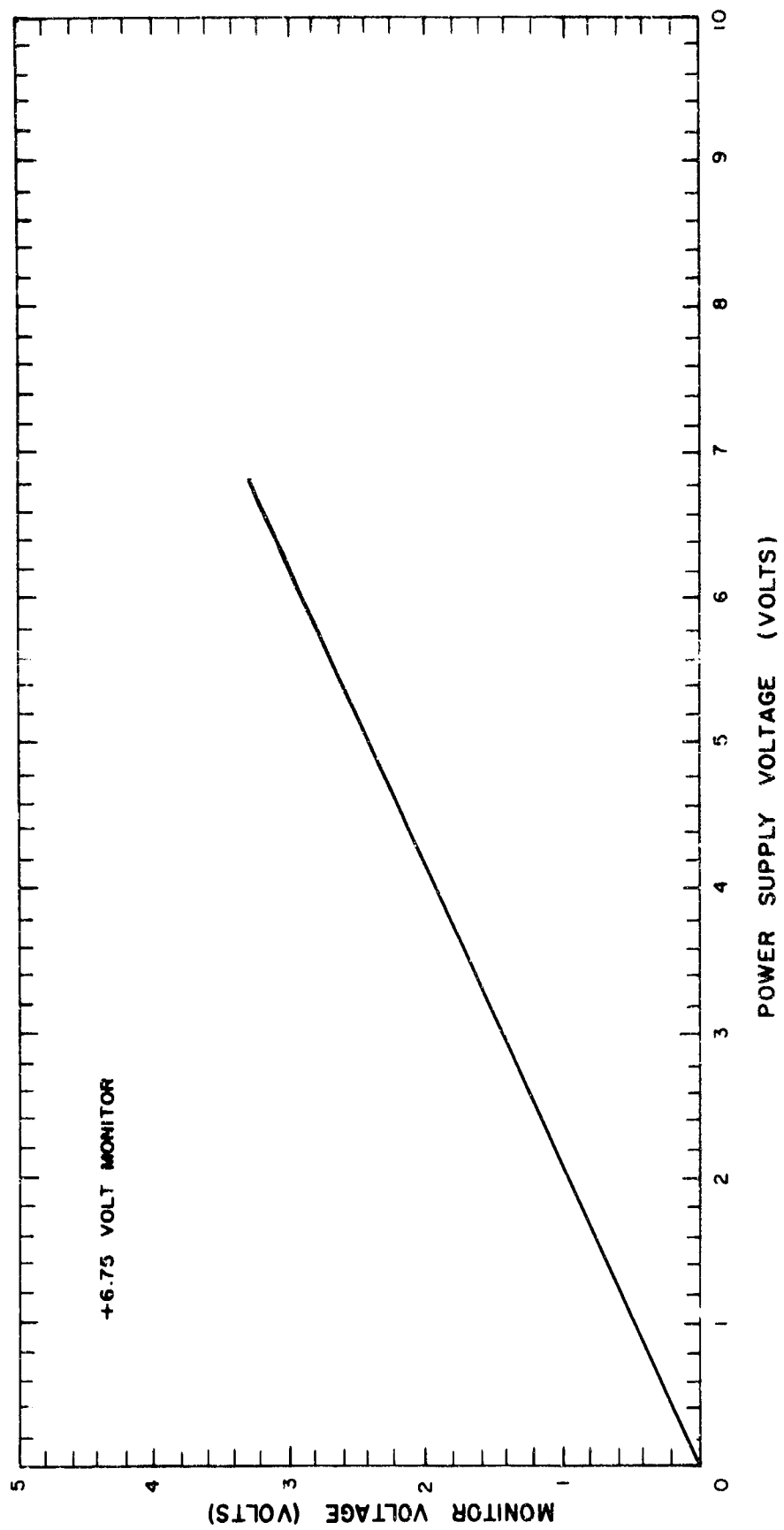
SO-3 (ESA #1)

$$N_1 = \frac{3.1 \times 10^{19} (I - I_n)}{E (E - E_L)} = \frac{3.1 \times 10^{19} (I - 10^{-8})}{E (E - 5 \times 10^3)}$$

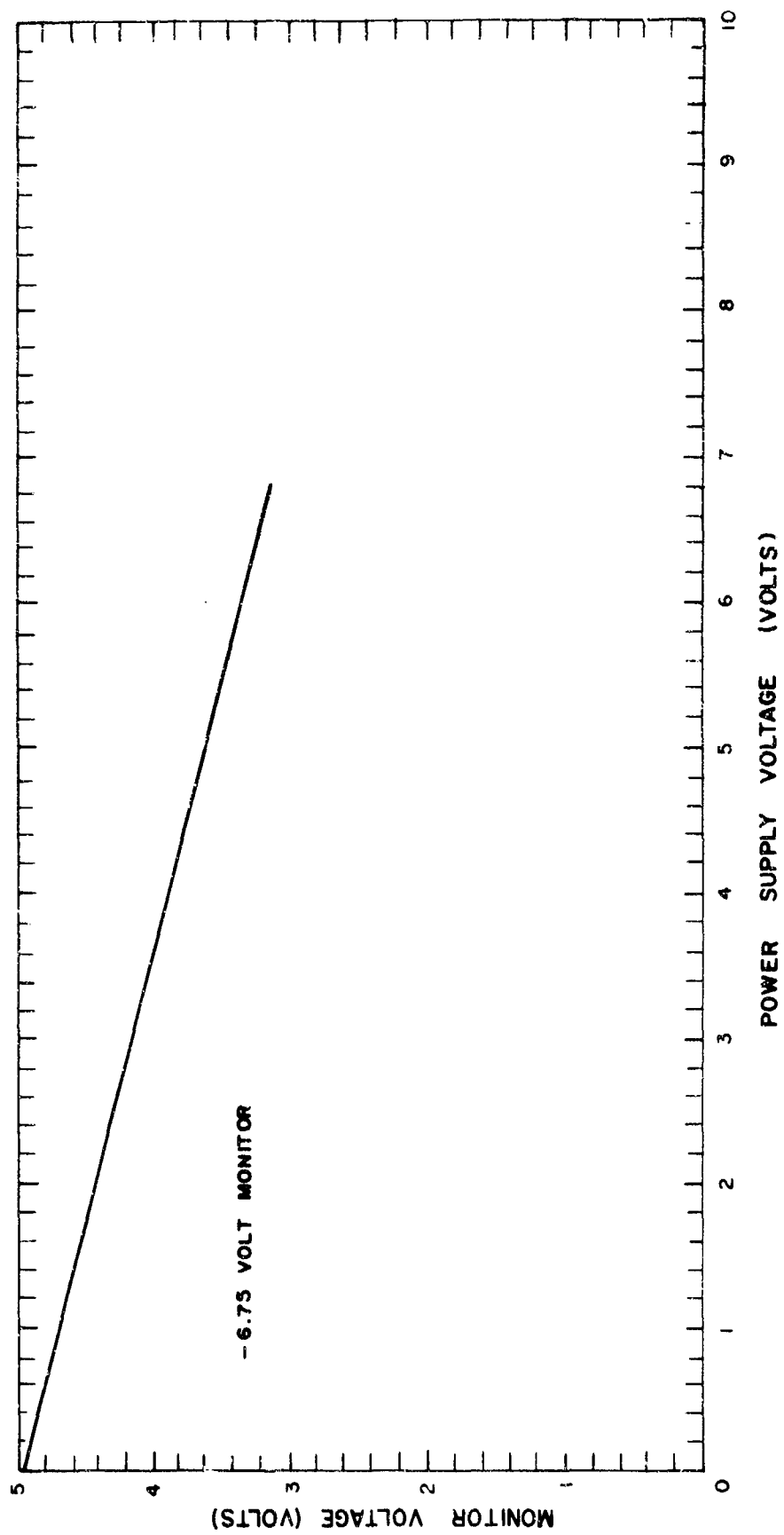
SO-2 (ESA #2)

$$N_2 = \frac{18.4 \times 10^{19} (I - I_n)}{E (E - E_L)} = \frac{18.4 \times 10^{19} (I - 10^{-9})}{E (E - 5 \times 10^3)}$$

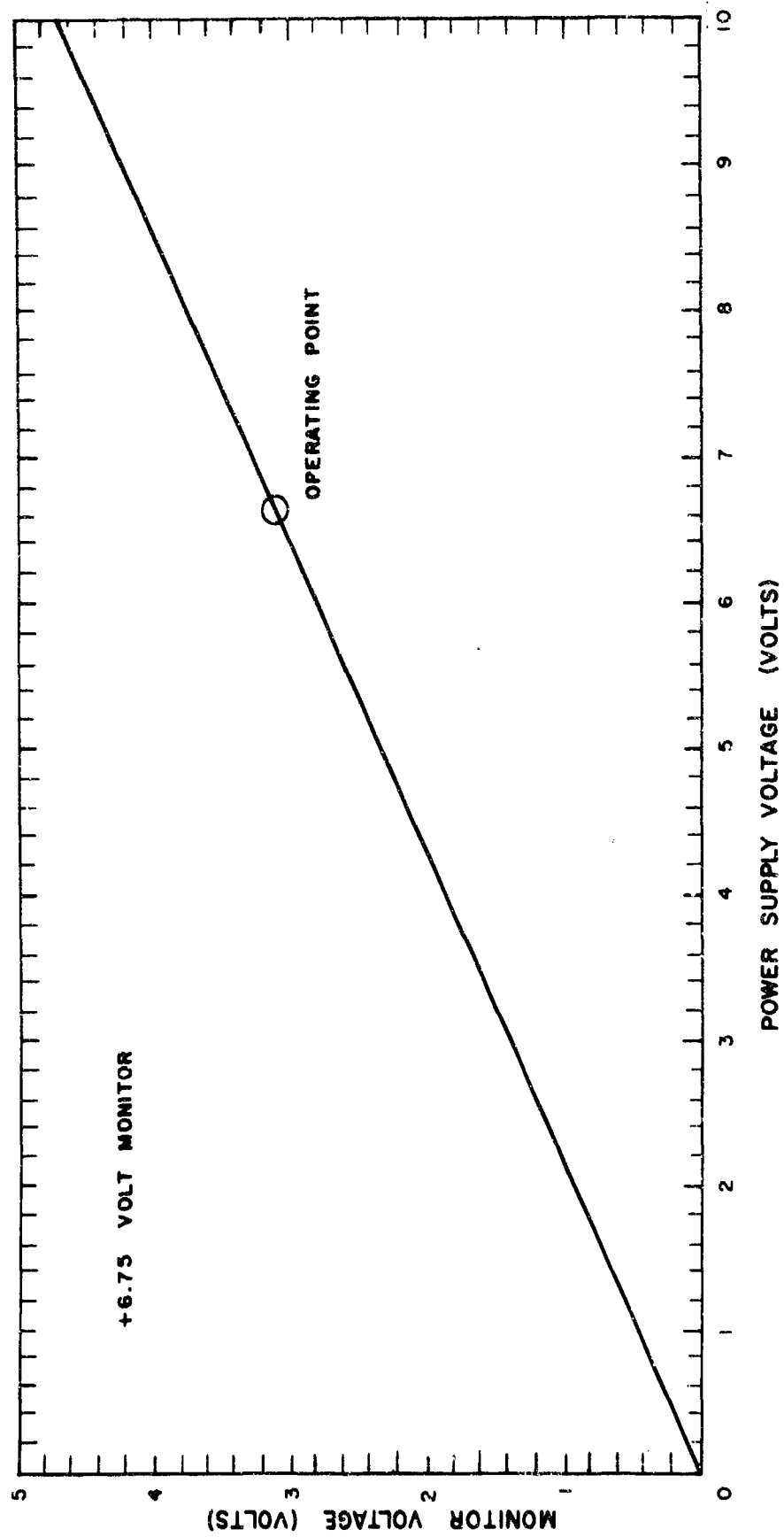
I is the photomultiplier output current (amperes) and I_n is photomultiplier dark current measured for each orbit (amperes) (typical values are shown in the above equations). E is the electron energy in eV and E_L is the average energy loss (eV) in the scintillator (1).



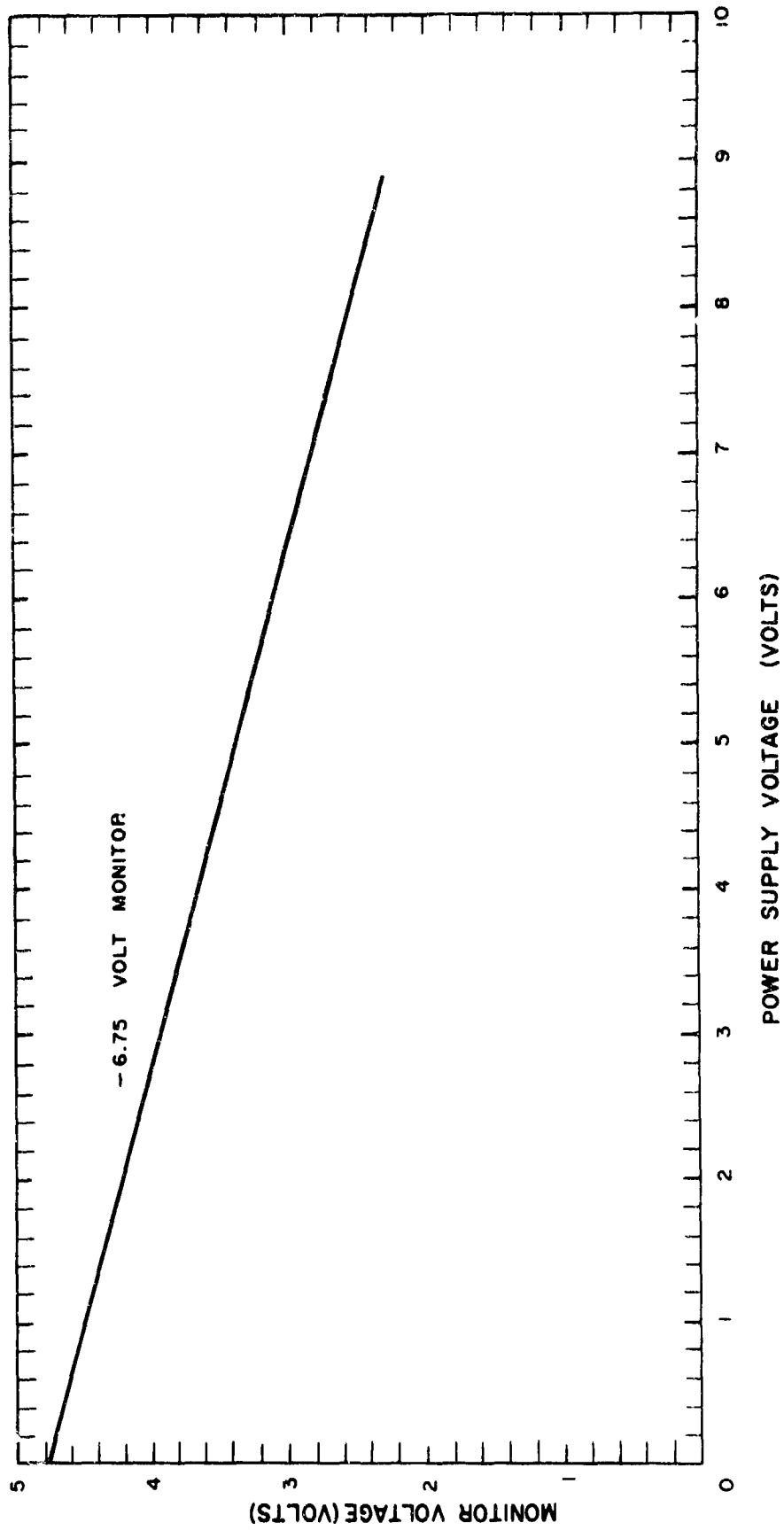
SO-1 CALIBRATION (SPARE UNIT)



SO-1 CALIBRATION (SPARE UNIT)

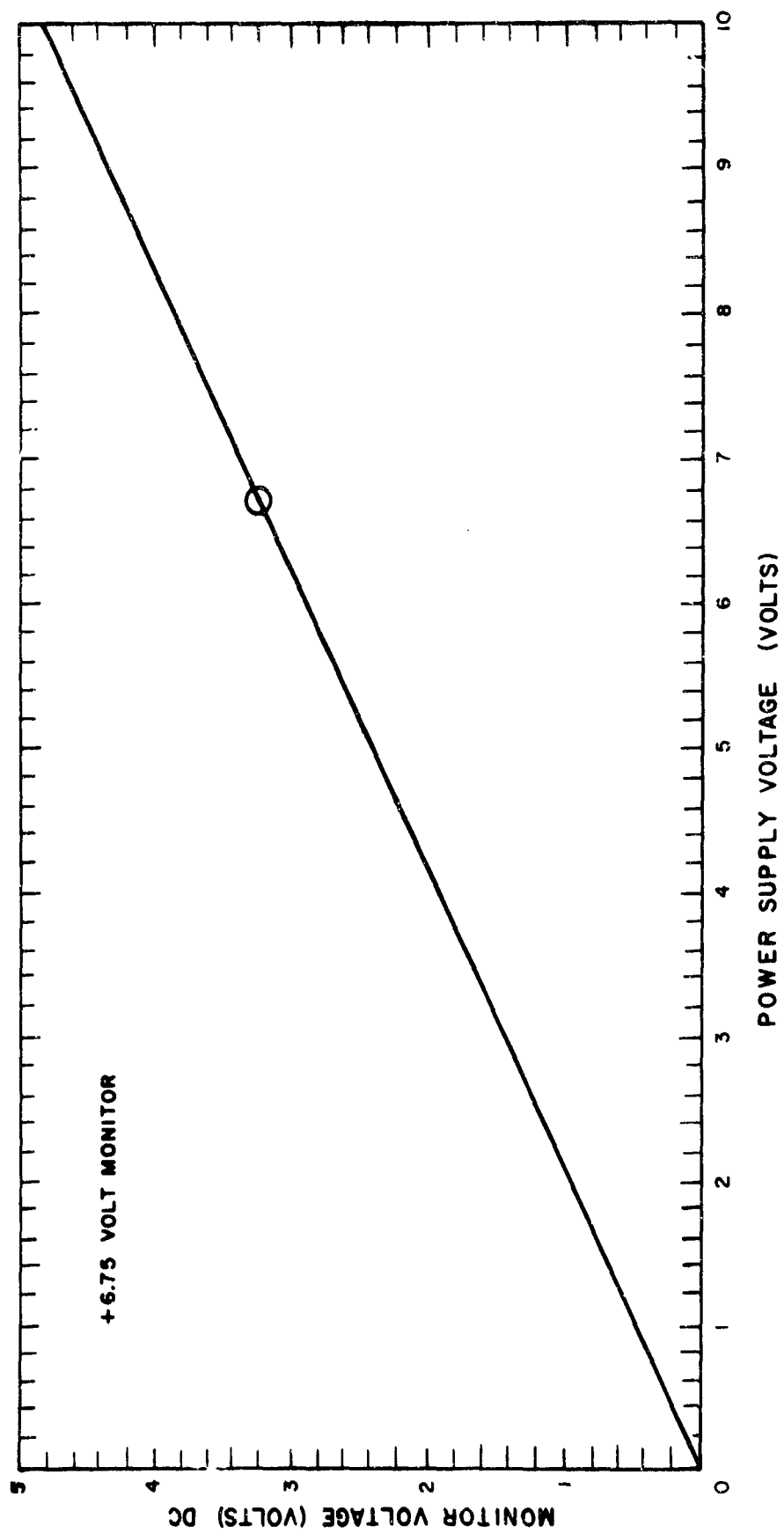


SO-2 CALIBRATION (ESA-2)

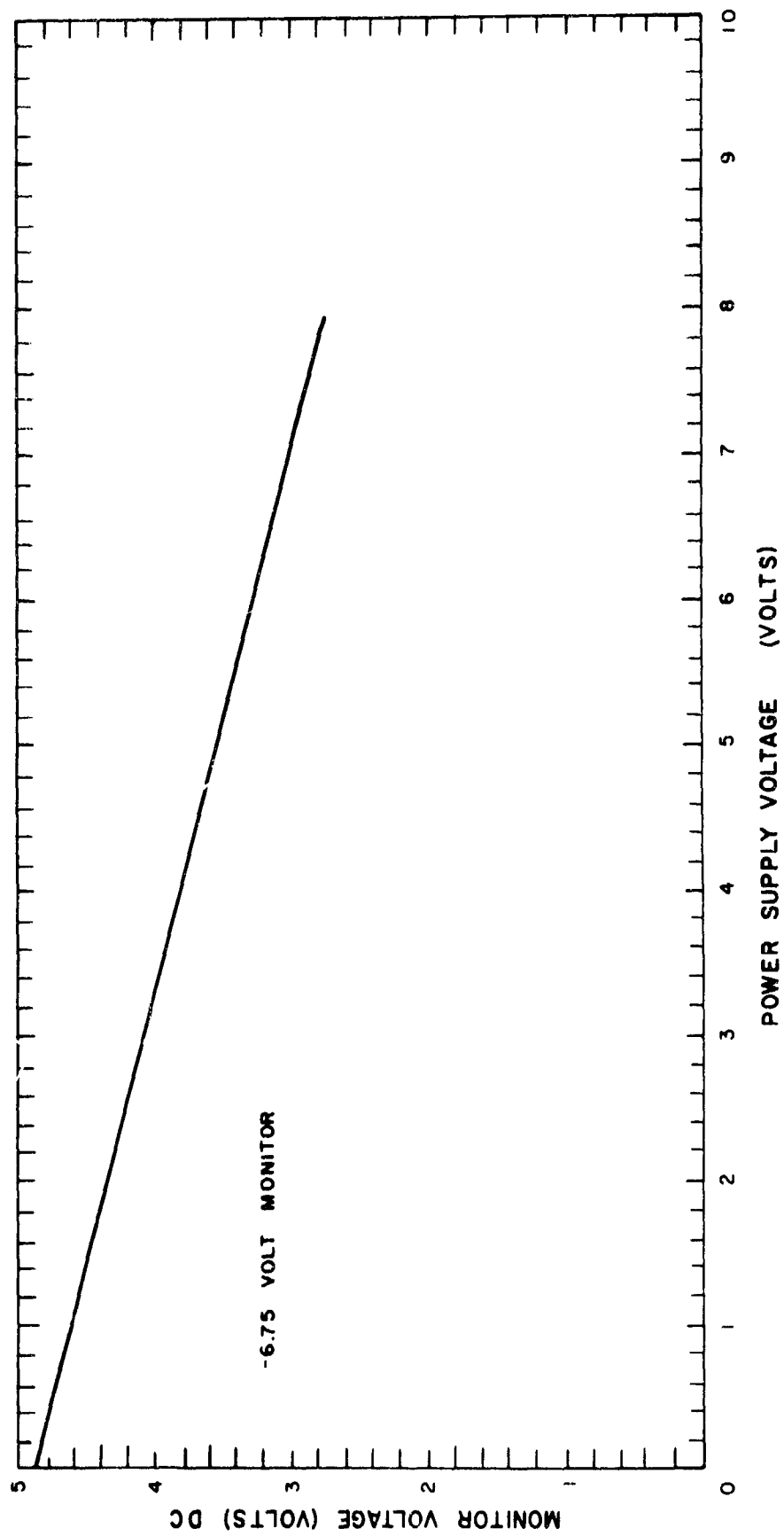


SO-2 CALIBRATION (ESA-2)

Figure 2-16



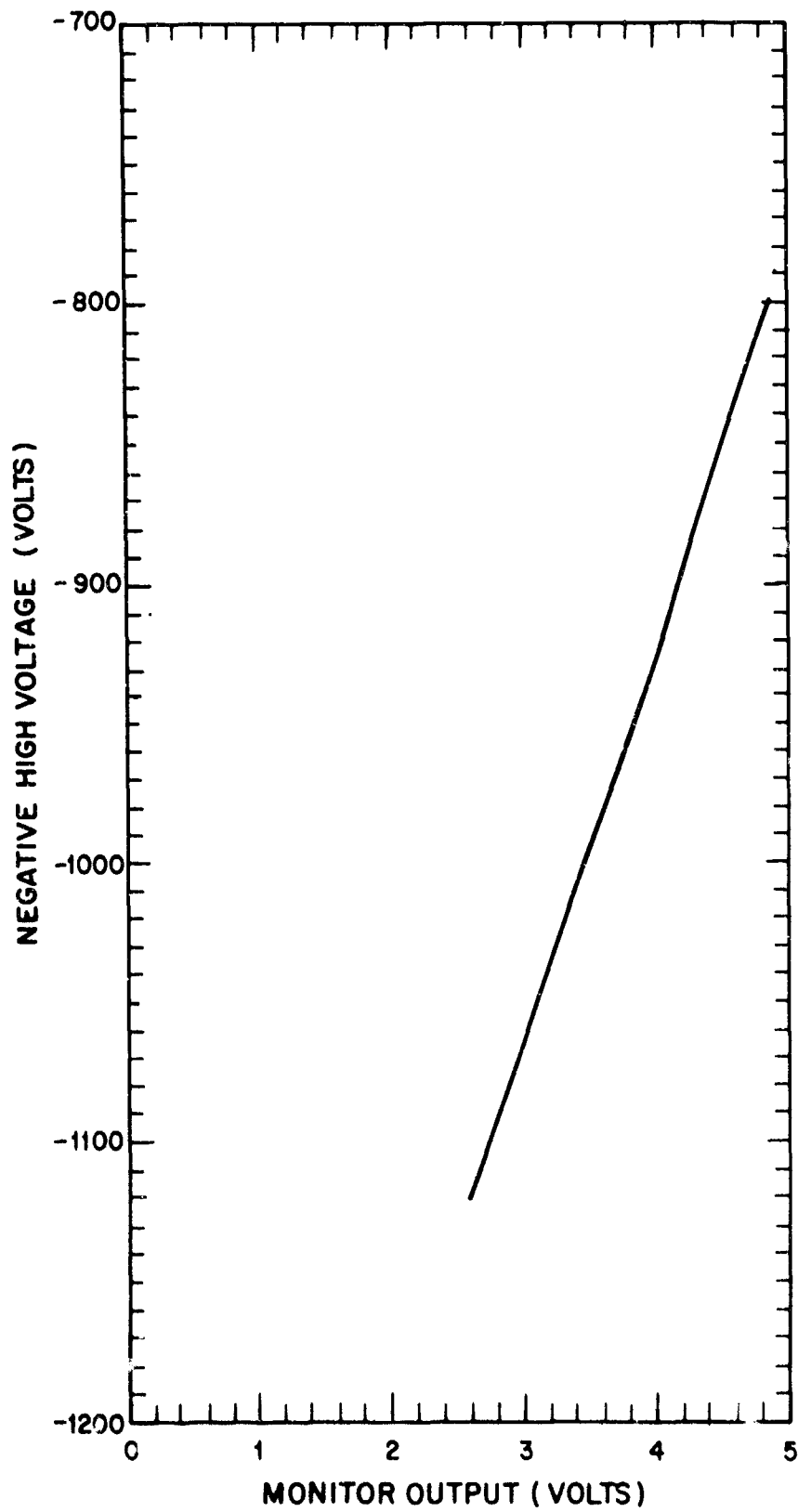
SO-3 CALIBRATION (ESA-1)



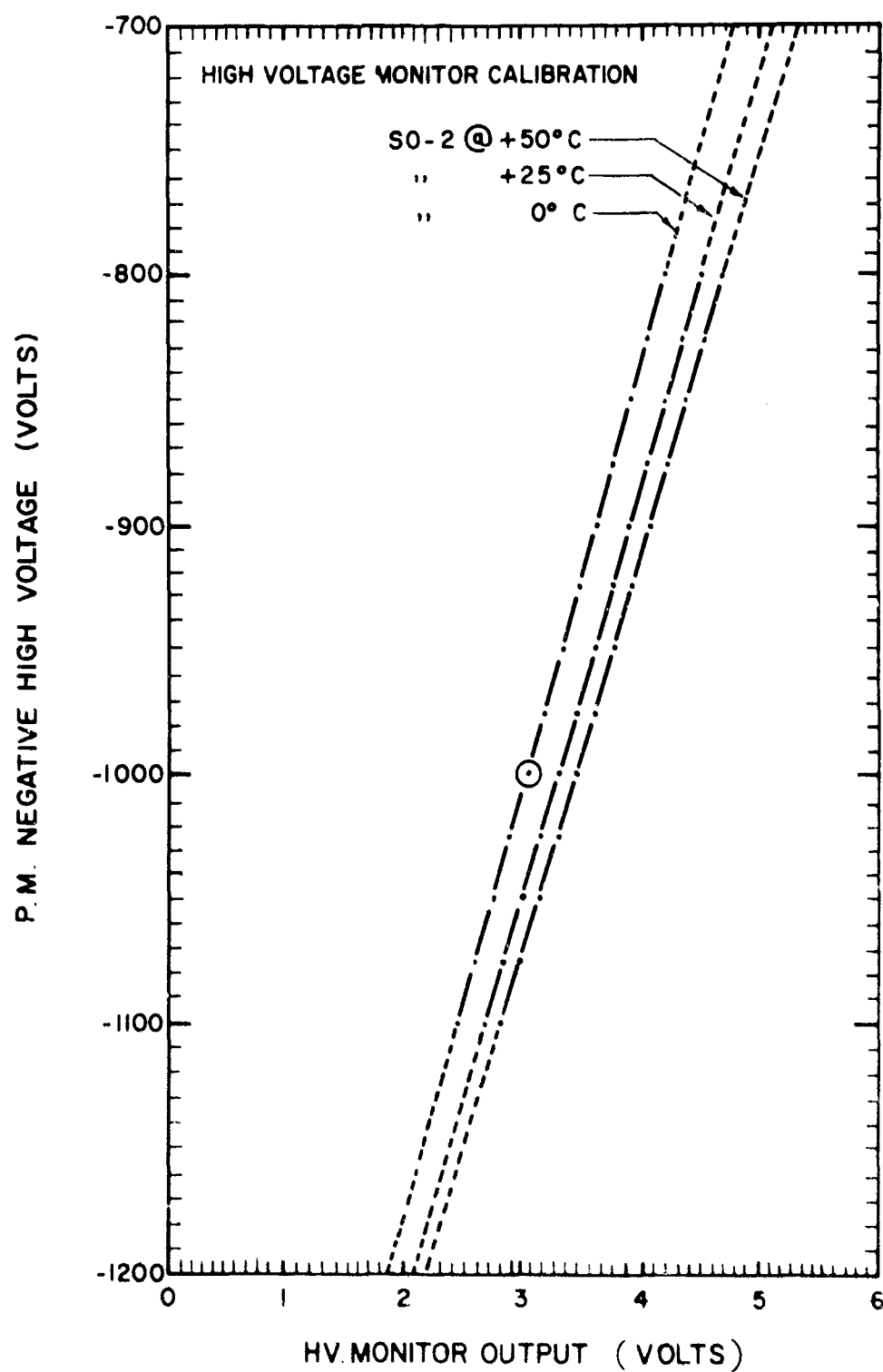
SO-3 CALIBRATION (ESA-1)

Figure 2-18

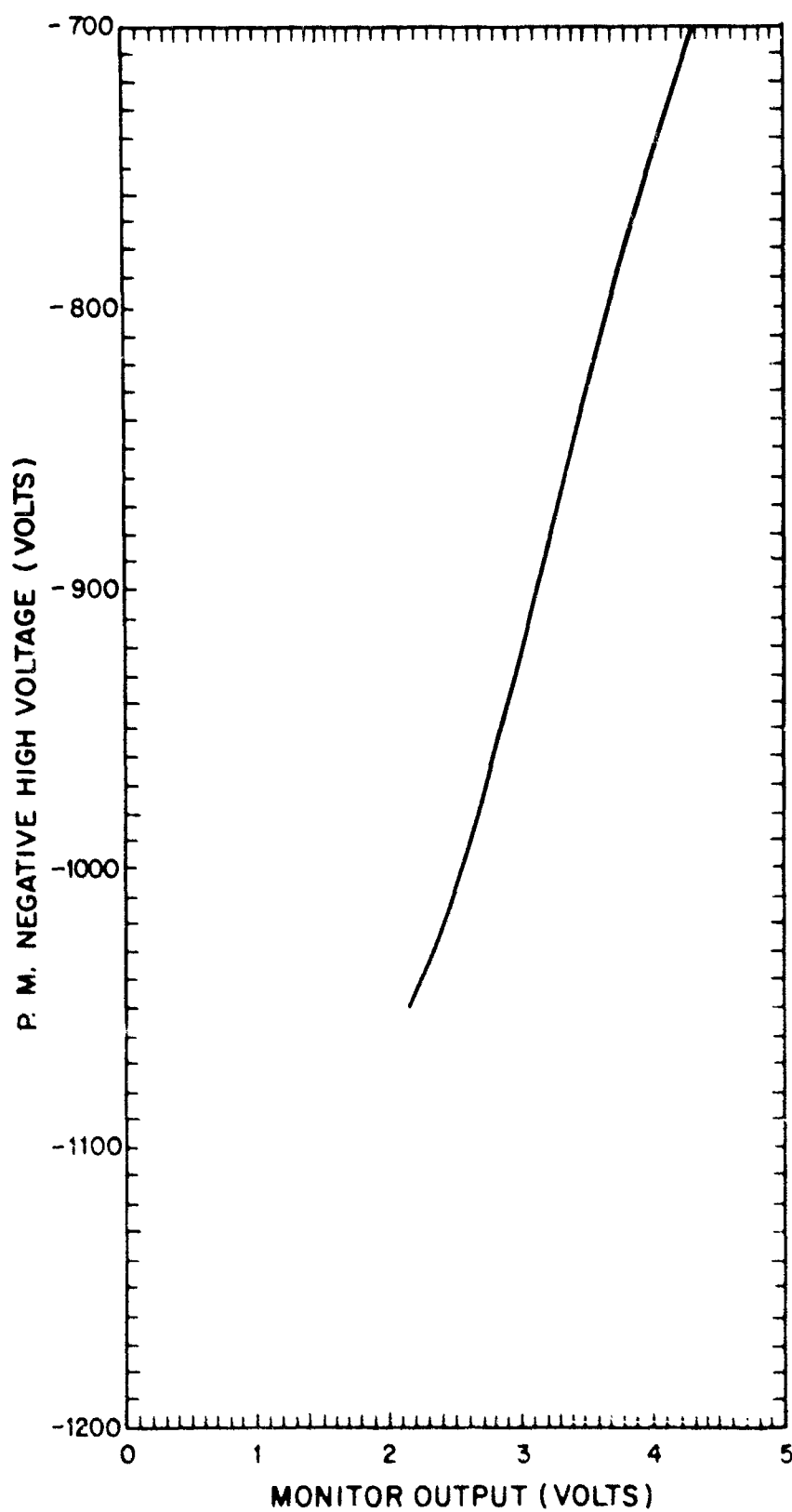
PHOTOMULTIPLIER HIGH VOLTAGE CALIBRATION SO-1 (Spare Unit)



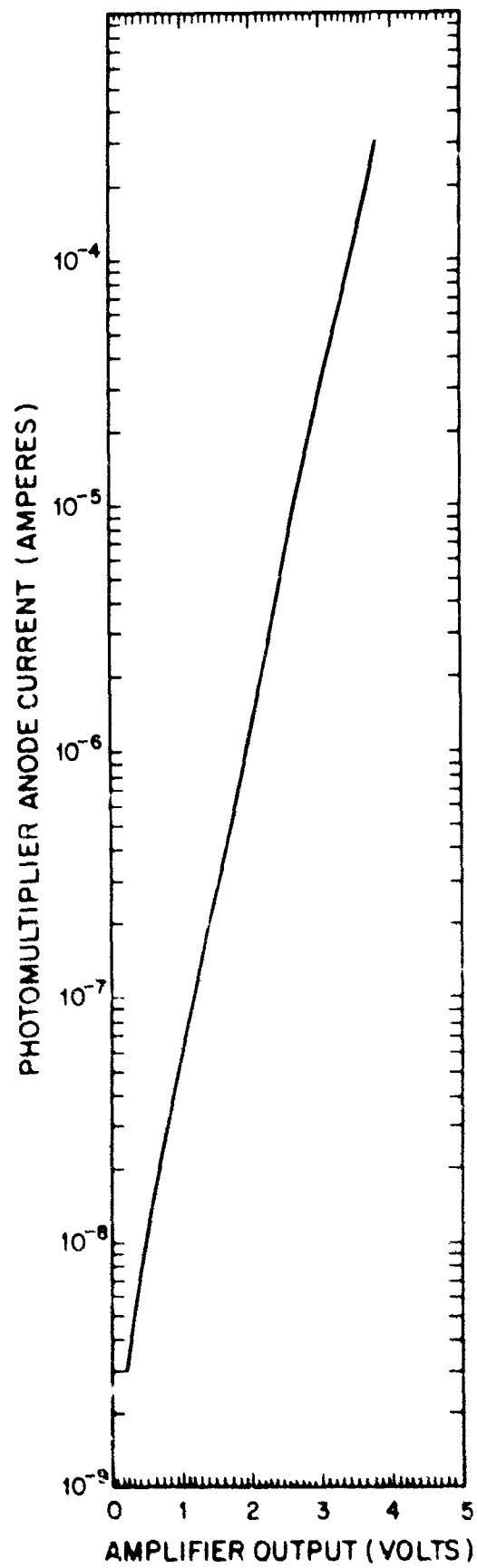
PHOTOMULTIPLIER HIGH VOLTAGE CALIBRATION SO-2 (ESA-2)



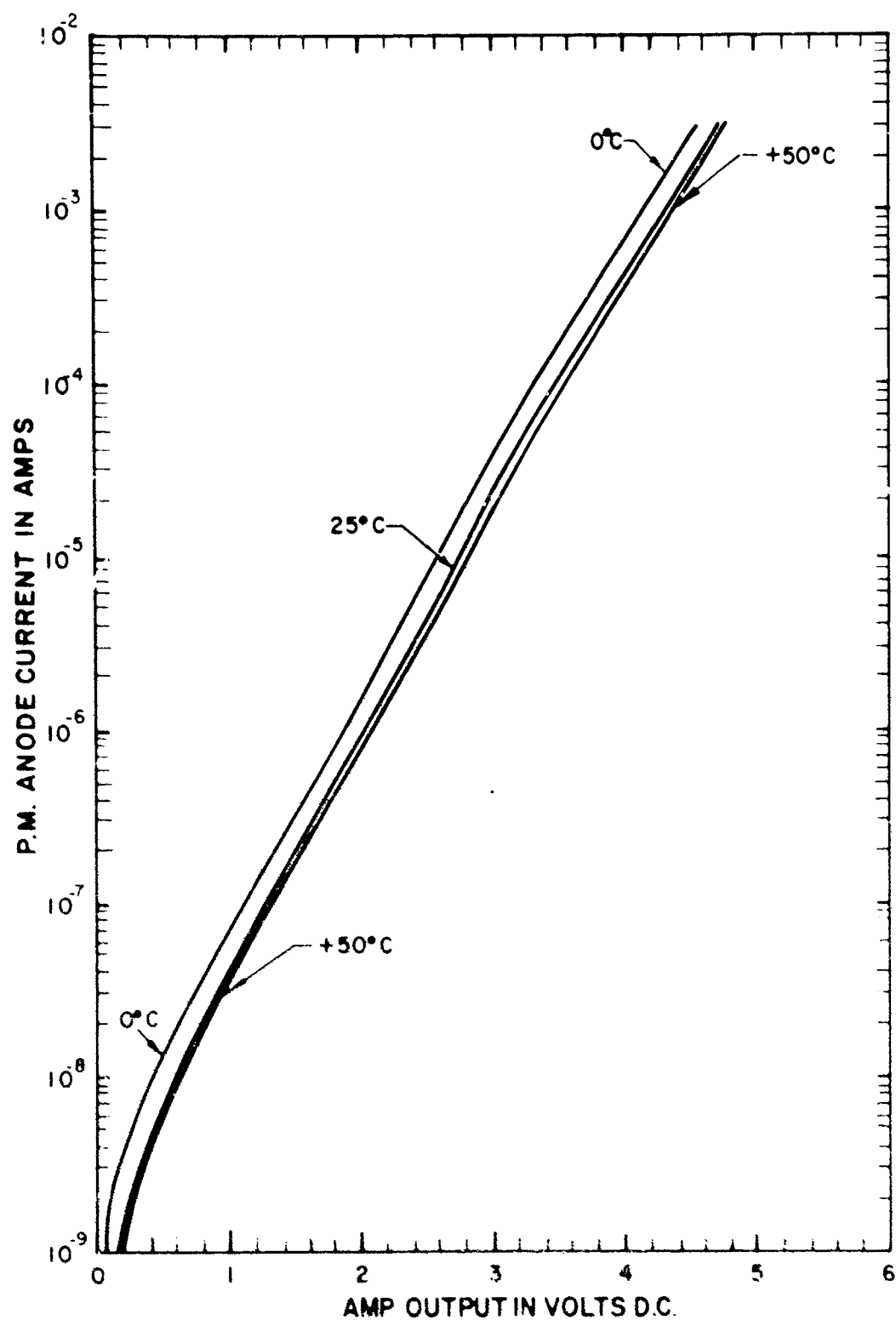
PHOTOMULTIPLIER HIGH VOLTAGE CALIBRATION SO-3 (ESA-1)



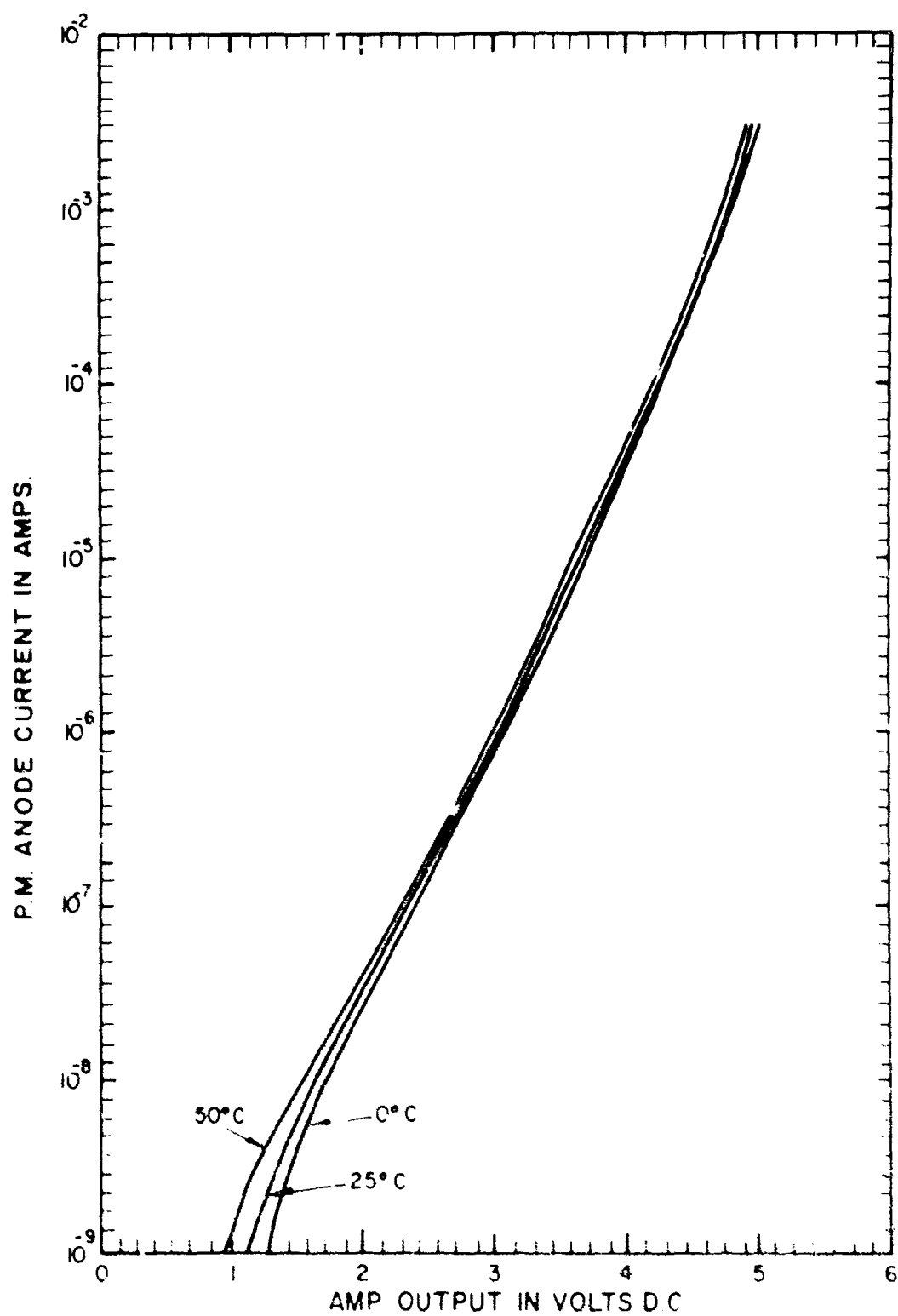
LOG CURRENT AMPLIFIER CALIBRATION SO-1



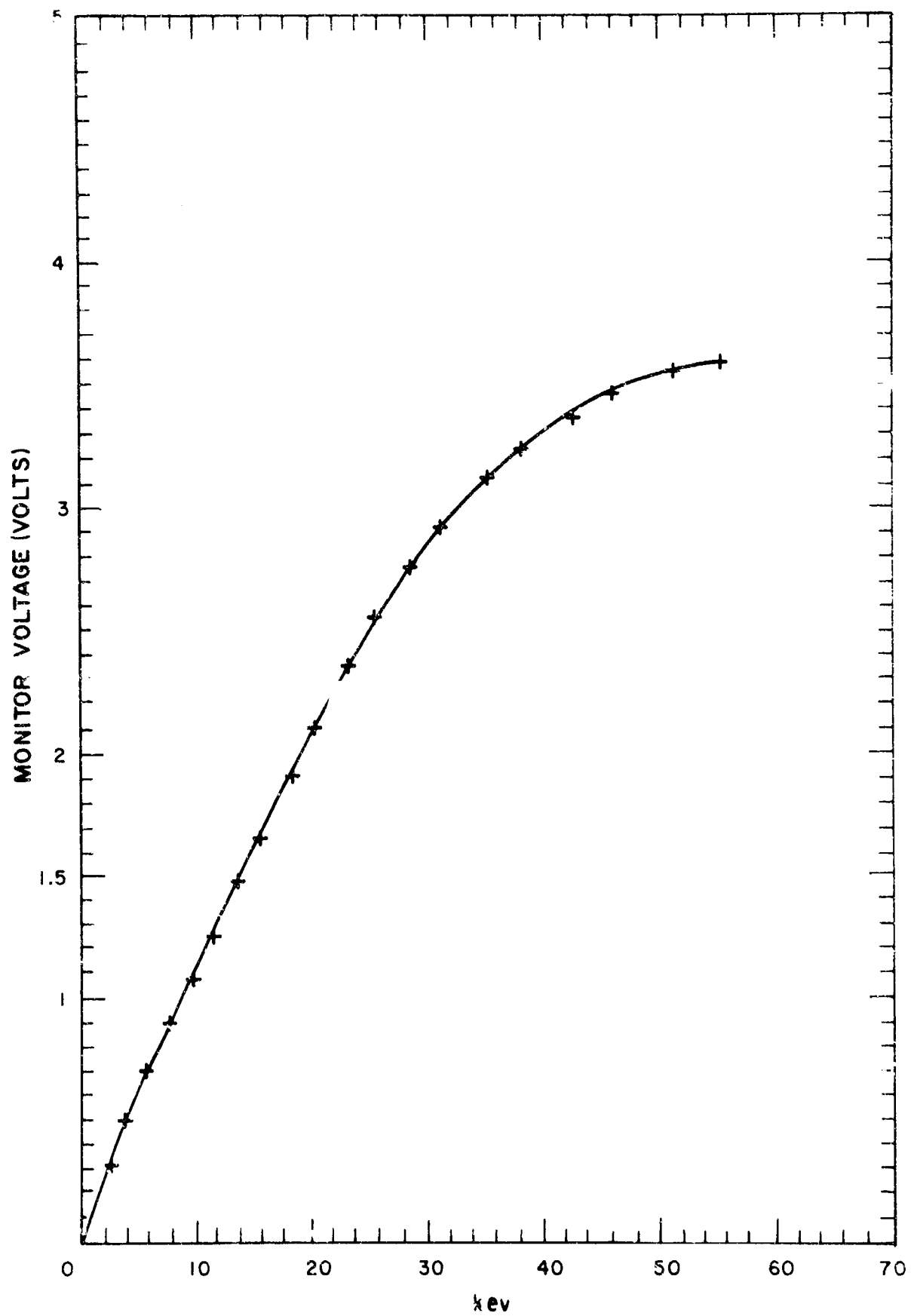
LOG CURRENT AMPLIFIER CALIBRATION SO-2 (ESA-2)



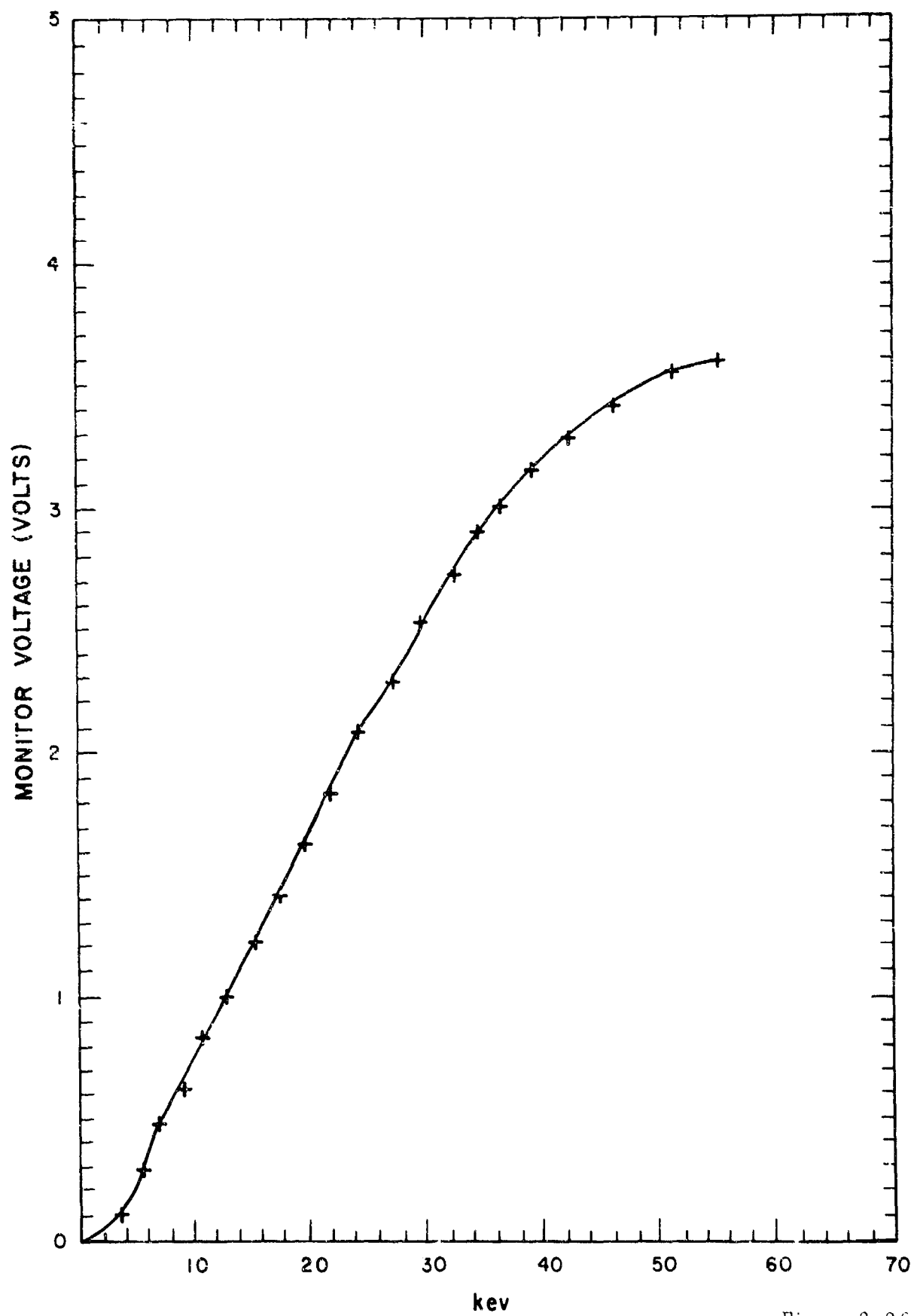
LOG CURRENT AMPLIFIER CALIBRATION (ESA-1) SO-3



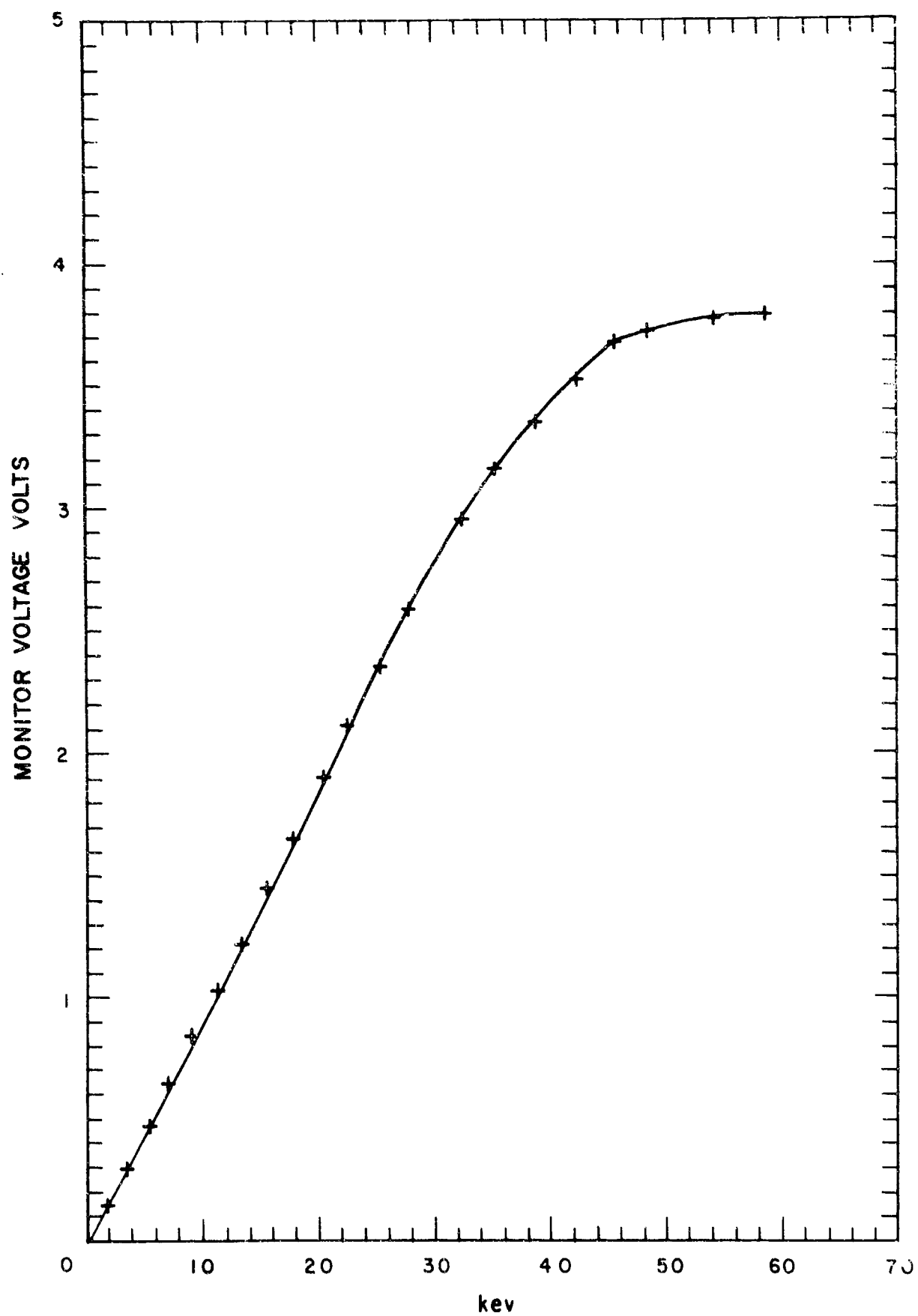
POSITIVE PLATE EQUIVALENT ENERGY SN-5



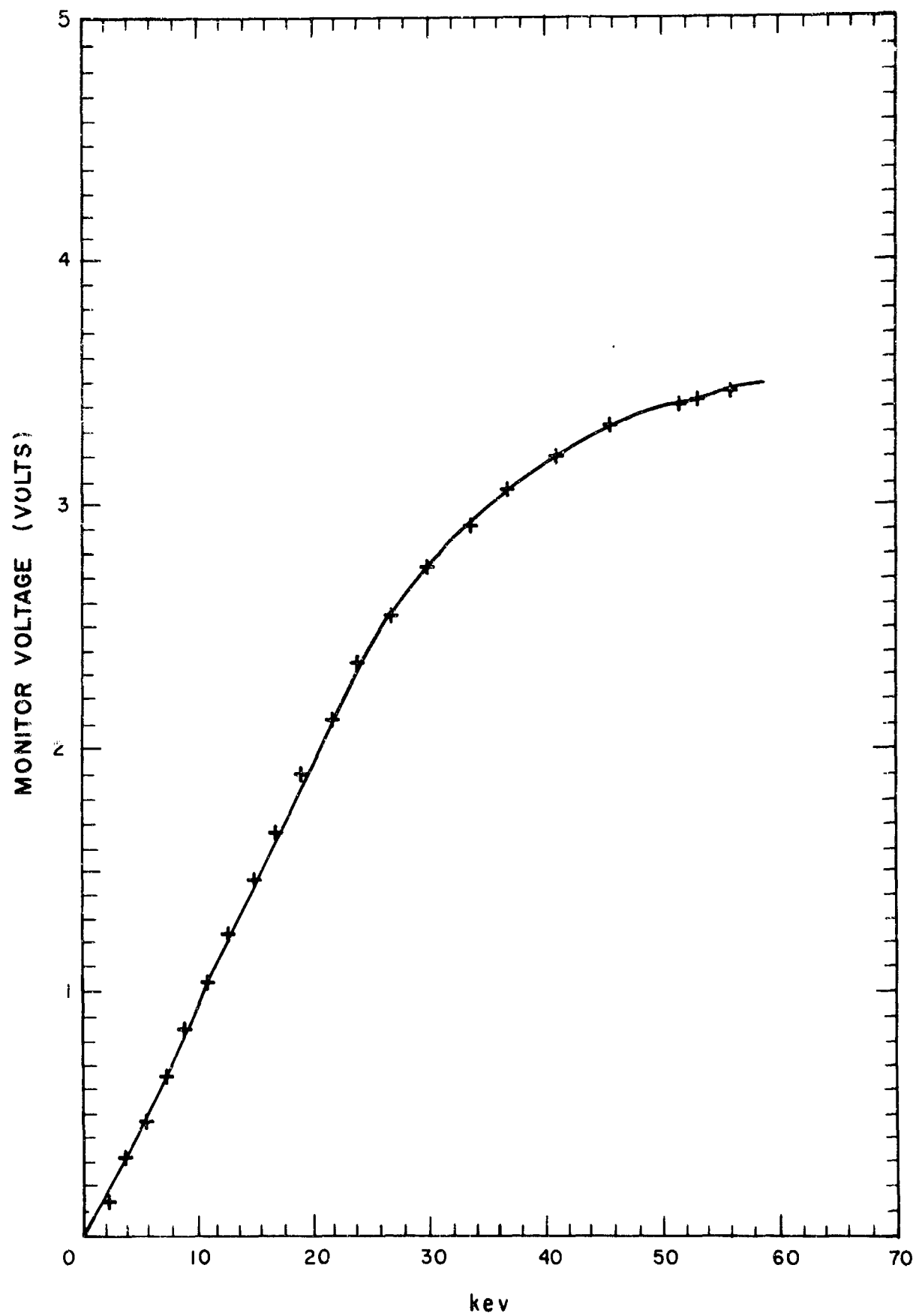
NEGATIVE PLATE EQUIVALENT ENERGY SN-5

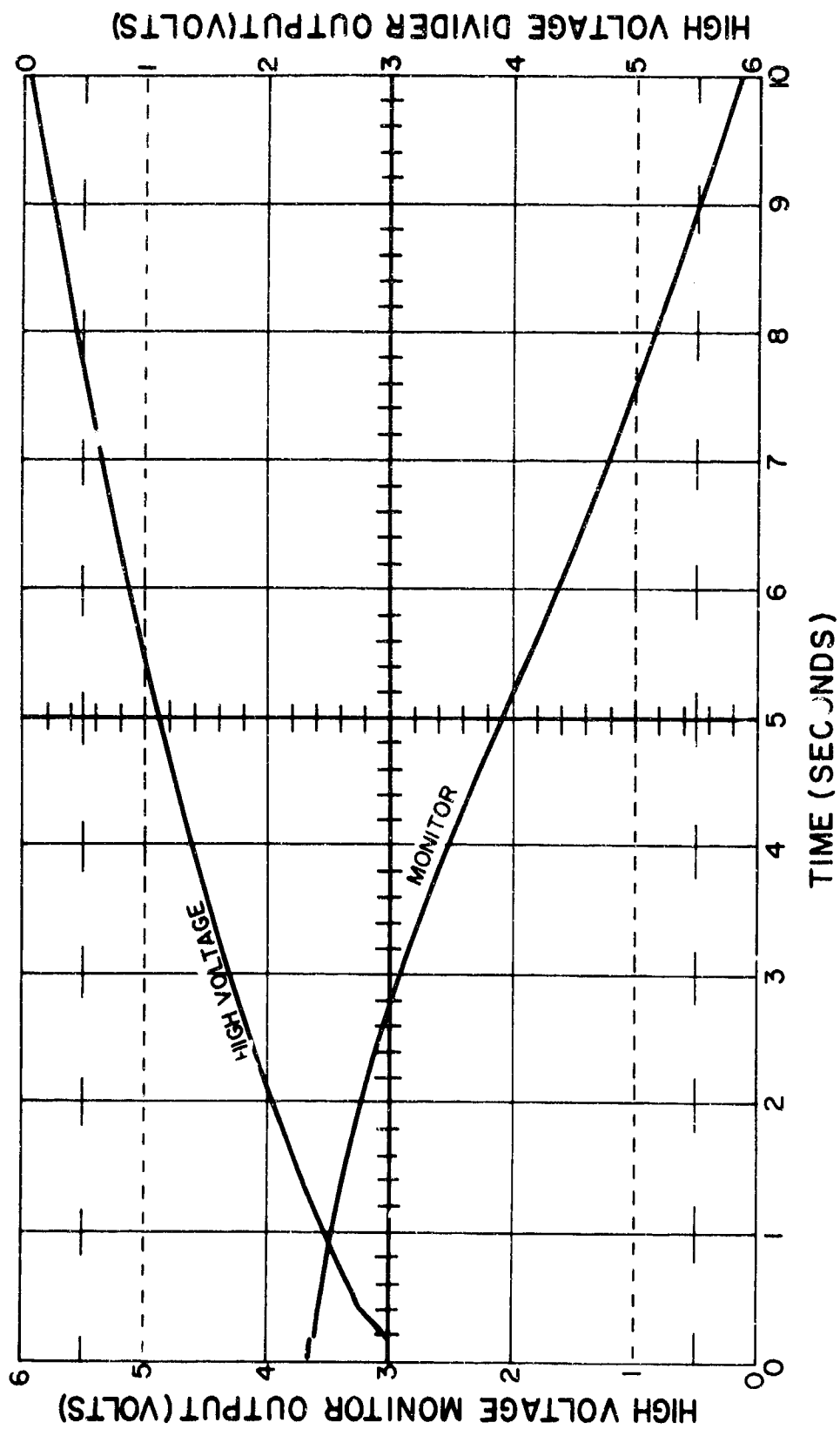


POSITIVE PLATE EQUIVALENT ENERGY SN-6

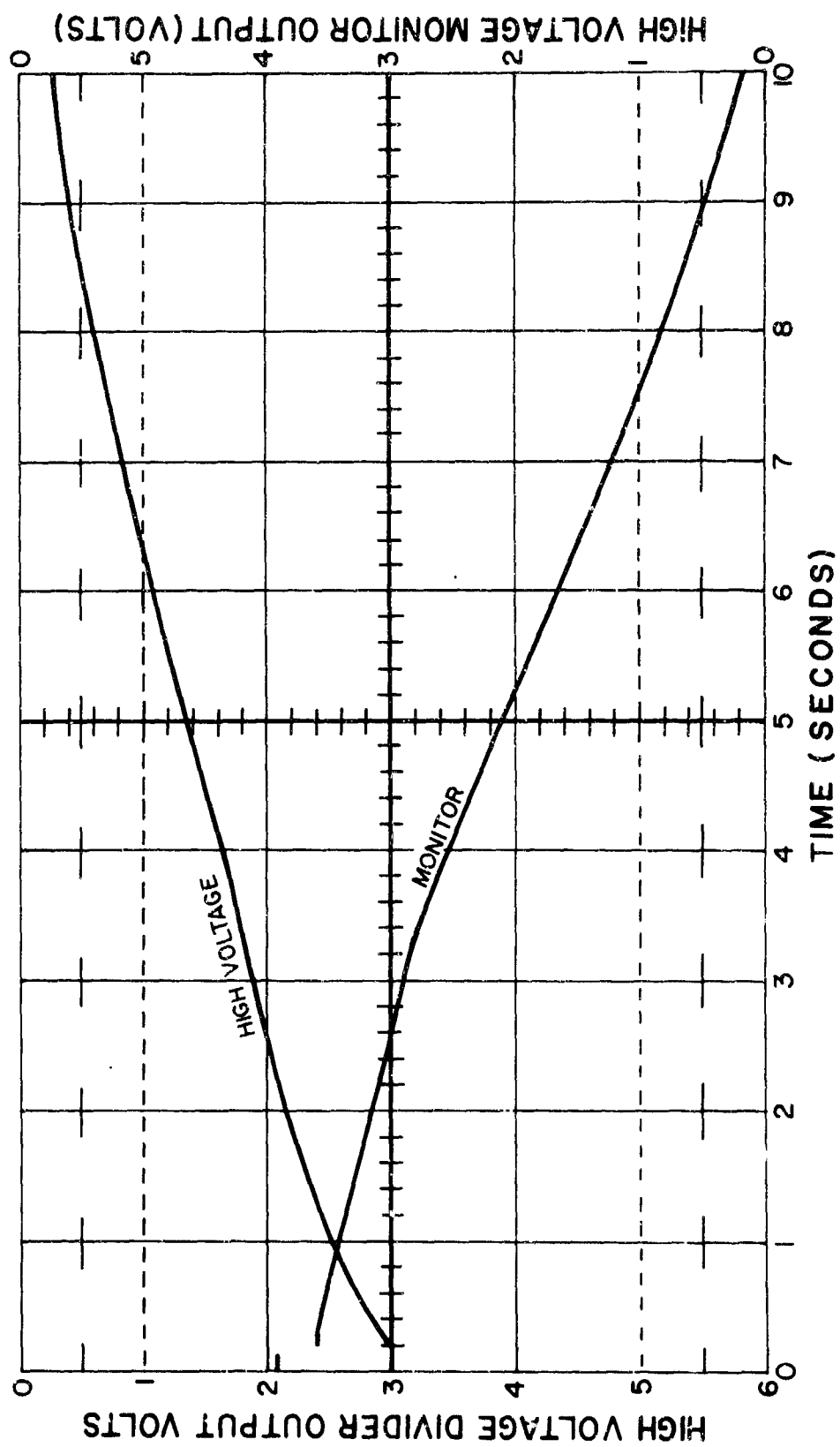


NEGATIVE PLATE EQUIVALENT ENERGY SN-6

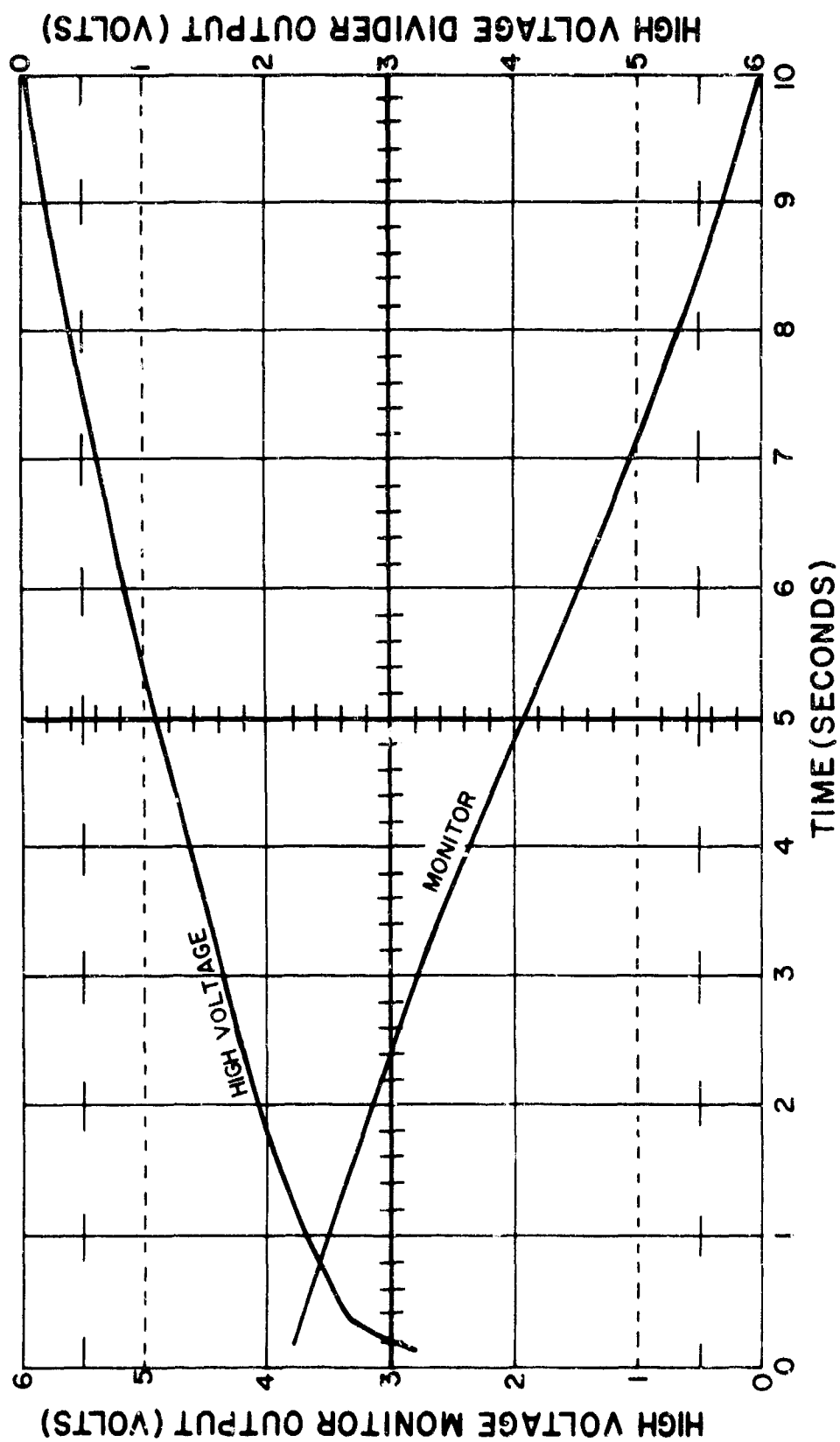




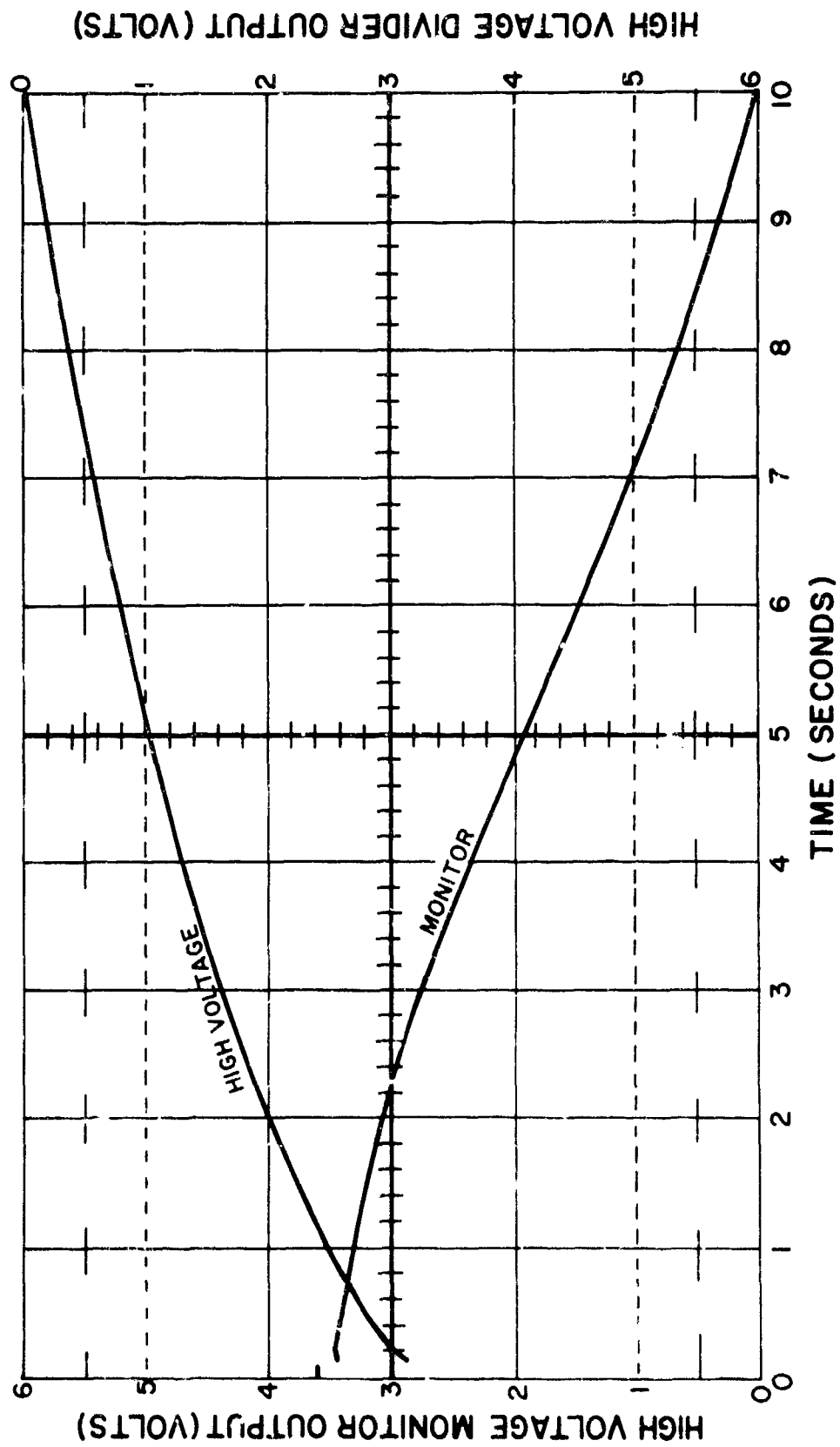
POSITIVE PLATE VOLTAGE AND MONITOR OSCILLOSCOPE
TRACE SN-5



**NEGATIVE PLATE VOLTAGE AND MONITOR OSCILLOSCOPE
TRACE SN-5**

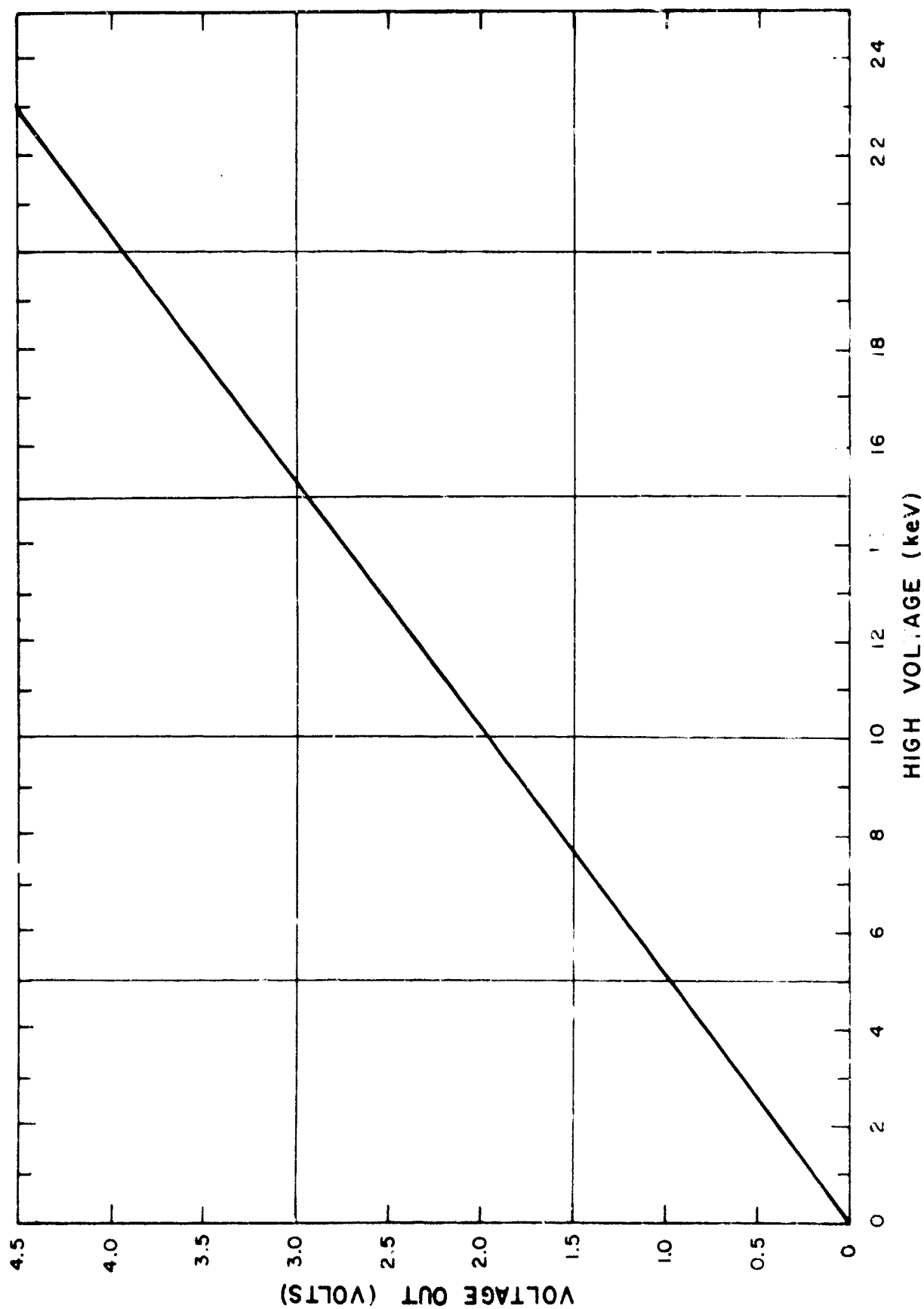


**POSITIVE PLATE VOLTAGE AND MONITOR OSCILLOSCOPE
TRACE SN-6**



**NEGATIVE PLATE VOLTAGE AND MONITOR OSCILLOSCOPE
TRACE SN-6**

VOLTAGE DIVIDER CALIBRATION



OSCILLOSCOPE TRACE CALIBRATION

2.3 Preflight and Inflight Performance and Sensitivity

Preflight instrument checkout was at Vandenberg Air Force Base. All tests were performed in the low plate voltage mode since corona discharge would occur if the unit were operated at maximum plate voltage at atmospheric pressure, and vacuum test facilities were not available. The following trip report summarizes the prelaunch checkout activity. It should be noted that both for prelaunch and inflight checkout and operation, ESA-2 must be turned on first and off last (Command 10 must be given before Command 11). This is required because the low plate sweep is generated in ESA-2. While both ESA's were interchangeable the low voltage sweep from one of the units (ESA-2) was used to drive both high voltage sweeps to keep the sweeps in synchronization.

Trip Report - Prelaunch and Post Launch Checkout of OV3-2 Electron Electrostatic Analyzer

This is a report on the field and launch support provided for the two electrostatic analyzers on the OV3-2 spacecraft October 12 through November 3, 1966.

Prior to final checkout, the preflight hanger tests at Vandenberg Air Force Base were initiated for the OV3-2 on October 12, 1966. The high voltage (15 kV) power supplies were operated in the low voltage mode with the dummy loads attached. During this test the ESA electronics and high voltage power supplies operated satisfactorily at high (29 volts), and nominal (26 volts) power supply voltages. Interference was observed between the mass spectrometer and the ESA when the supply voltage was below 23 volts. (At the beginning of every other high voltage power supply sweep the mass spectrometer sweep was triggered.) The power was being supplied through a very long cable and this problem did not occur when the spacecraft power was supplied through a short cable.

During the low voltage (23 volts) test the high voltage power supply No. 2 (SN-4) positive high voltage monitor changed its sweep characteristics. Instead of sweeping from 1.4 volts to zero it swept from 2.5 to 1.5 volts. This unit was tested using the spare ESA electronics and a special test box and the sweep rate increased from 0.1 cps to 1.0 cps. The unit was re-connected to the spacecraft and a 0.14 cps sweep rate was observed with only one power supply connected to the sweep circuit. When both power supplies were connected the sweep rate returned to 0.1 cps. The power supply was removed from the spacecraft and tested using a cable to replace the test box. The same results as those obtained on the spacecraft were observed in this test. The change in the monitor voltage levels occurred because the light bulb in the positive high voltage section had burned out. The spare power supply was checked out on the bench and then mounted on the spacecraft on Friday morning. The systems test was started about 12 PM Friday and proceeded smoothly until a part of the procedure where a three hour delay is sent and then a reset command is given. A spurious signal caused various relays in the tape recorder to be set to improper positions. This problem did not occur during integration tests when the delays were allowed to run out. It was determined that power was being fed back into the tape recorder (which was designed to operate on pulses) from the experiments. In particular the capacitors in the input circuit of the ESA power supplies ($\sim 100 \mu f$ each) and the ESA electronics ($\sim 50 \mu f$ each) discharged through the relays in the tape recorder when the reset command is sent.

This problem was solved by placing diodes (1N645) in the input power circuit (at the rear of a connector) to the ESA units. The diodes were connected and potted. During further tests, the P.M. high voltage monitor changed from 2.4 volts to 1.9 volts. The ESA electronics section (not the plates) were removed, the unit was checked, and the monitors read normally. The dark

current, however, increased to 9×10^{-9} amps. The spare was checked (the previous dark current of 1.8×10^{-9} amps was observed) and installed. It was discovered that S. G. had installed the diodes in the ESA input circuit backwards and they had to be replaced and repotted. The ESA was then checked on the spacecraft on October 17.

On October 18, it was learned that the potting material used to pot the Space General Connector would outgas. This potting material was removed and the connector repotted. The final system test was completed on October 18.

The blockhouse panel to switch the electrostatic analyzer into the high voltage mode prior to launch was installed and checked on October 19. On Thursday, October 20, the spacecraft was mated to the fourth stage and on Friday, October 21, the spin balance with the fourth stage was completed (about 1000 gms were added).

On Monday, October 24, the spacecraft was moved from the spin facility to the pad and the system check was performed. The test was normal. The ESA and mass spectrometer were turned off during the record cycle and the recorder was on for 75 minutes (1/2 of the tape).

On Tuesday, October 25, ordnance was installed and on Wednesday, October 26, the mock count was performed. Thursday, October 27, at 11:00 P. M. the countdown was begun and continued until T-30 minutes (4:00 A. M. local time October 28) at which point a hold was called for a passenger train in the corridor. The count was picked up at 4:25 A. M. and proceeded until launch at 4:56 A. M. (October 28 11:56 Z). Orbit was confirmed and the booms were deployed. However, various commands were observed to be performing additional functions (e. g., Command 10 (ESA-2 off) turned two experiment groups off, ESA-1 and the IMS, and another command turned the beacon off when it should not have). The six h delay had been inserted (although this command should not have been given) and could not be removed. The ESA's were not to be turned on for four days

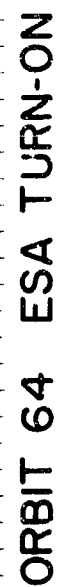
On Saturday, October 29, it was decided not to send anymore commands to the spacecraft over the weekend except for "address." Prior to this, numerous commands had apparently been sent by various stations around the world. On Tuesday, November 1, the ESA was turned on (during orbit 61/62) and functioned properly with the exception of the power supply sweep voltage discussed below.

The electrostatic analyzers were not turned on for four days after launch to allow sufficient time for the spacecraft and the units to outgas and to insure that arcing would not occur. At turn-on the monitors read the same as prior to launch with the exception of the high voltage sweeps. After the first tape recorder pass the high voltage power supply monitors indicated that the high voltage was not rising consistently to its programmed value. As a result, the nominal maximum energy measured with the ESA's is approximately 60 keV for ESA-1 and 70 keV for ESA-2. This malfunction did not affect data obtained at lower energies. (End of Trip Report)

Figure 2-34 shows a strip chart record covering the period of initial turn on. The instrument was turned on in daylight and the modulation of the PM signal channels is due to light leakage in the photomultiplier unit. The most probable source of the light leakage are small imperfections in the thin (2000Å aluminum) light shield deposited on the scintillator.

Since the sun is only observed for a portion of the spin period, it is possible to reduce some of the data that may be obtained during this time. When the sun is observed, one maximum per spin period occurs (except for secondary maxima due to scattering of the sunlight), and the amplitude of the signals are relatively large. Since the amount of light leaking into the ESA's and striking the photocathode is quite different for each ESA, the current output differs by about two orders of magnitude.

When the satellite is apparently passing through a portion of the inner radiation belt at apogee (detailed ephemeris data is needed to determine this), the data output of both ESA's rise to very high levels and no spin or



sweep modulation is observed. The output at that time was apparently due to high energy particles in the radiation belt striking the scintillator and producing a light output.

The sensitivity of the ESA's to sunlight and to the radiation belts can be used to monitor the performance of the instrumentation throughout the life of the satellite. The response of the instrumentation in the inner radiation belt is independent of direction and therefore is probably due to energetic protons penetrating directly into the scintillator. To a first approximation because of the symmetry of the satellite, each scintillator will be exposed to the same amounts of radiation and the ratio of the PM output currents should be the same as that given in 2.2.2 for the preflight alpha source calibration. The alpha source measurement resulted in a ratio of SO-3 (ESA-1) current output to SO-2 (ESA-2) current output of 4. The ratio measured in the radiation belts was initially two and declined to 1.3 in later orbits. This difference can be accounted for by slight changes in operating voltage and temperature and also to differences in background flux at the two instruments since shielding for the two instruments is only approximately the same. This behavior indicates that no appreciable degradation of the detector units occurred during the flight since it would be extremely fortuitous for major changes to occur in both detectors without a large change in the sensitivity ratio.

Because of the difficulty in calculating shielding effects and variations in the radiation belt flux at the position of the satellite it is simpler to use the solar sensitivity to determine the temporal behavior of each instrument. (The spacecraft measurements show that this response is constant when the instrument is sun centered within 10° .) Preliminary evaluation of the solar response indicates no significant detector degradation, in agreement with the conclusions reached in considering radiation belt sensitivity.

The behavior of the instrumentation prior to launch and in orbit is shown in Table 2.3. The nominal voltage readings are the measured values after final assembly and checkout of the instrument and prior to integration in the spacecraft. Values are given for representative orbits throughout the mission. The minimum detectable signal was defined as a 0.1 volt increase above noise. Using this definition and the noise levels measured in flight, the sensitivity for ESA is approximately the same and is shown for typical noise levels in Figure 2.35. This minimum sensitivity corresponds to an energy flux of approximately $2 \times 10^4 \text{ keV cm}^{-2} \text{ sec}^{-1} \text{ ster}^{-1}$ between 10 and 20 keV which corresponds to a strong Type 1 Aurora.

On several orbits spurious electron spikes were observed. These were seen only on ESA-2 at the higher electron energies to which ESA-1 was not sensitive. After closer examination, it was noted that these signals did not have a proper pitch angle distribution. The signal was observed on every other spin period when the ESA plate voltage was high and at the position where the instrument field of view was most closely aligned to the satellite velocity vector. No such spurious signals have been observed when the angle between the center of the instrument field of view and the velocity vector exceeds 45° . While the effect is not understood, the data do not represent valid electron spectral measurement and has been excluded from our analysis.

2.4 Orbital Parameters

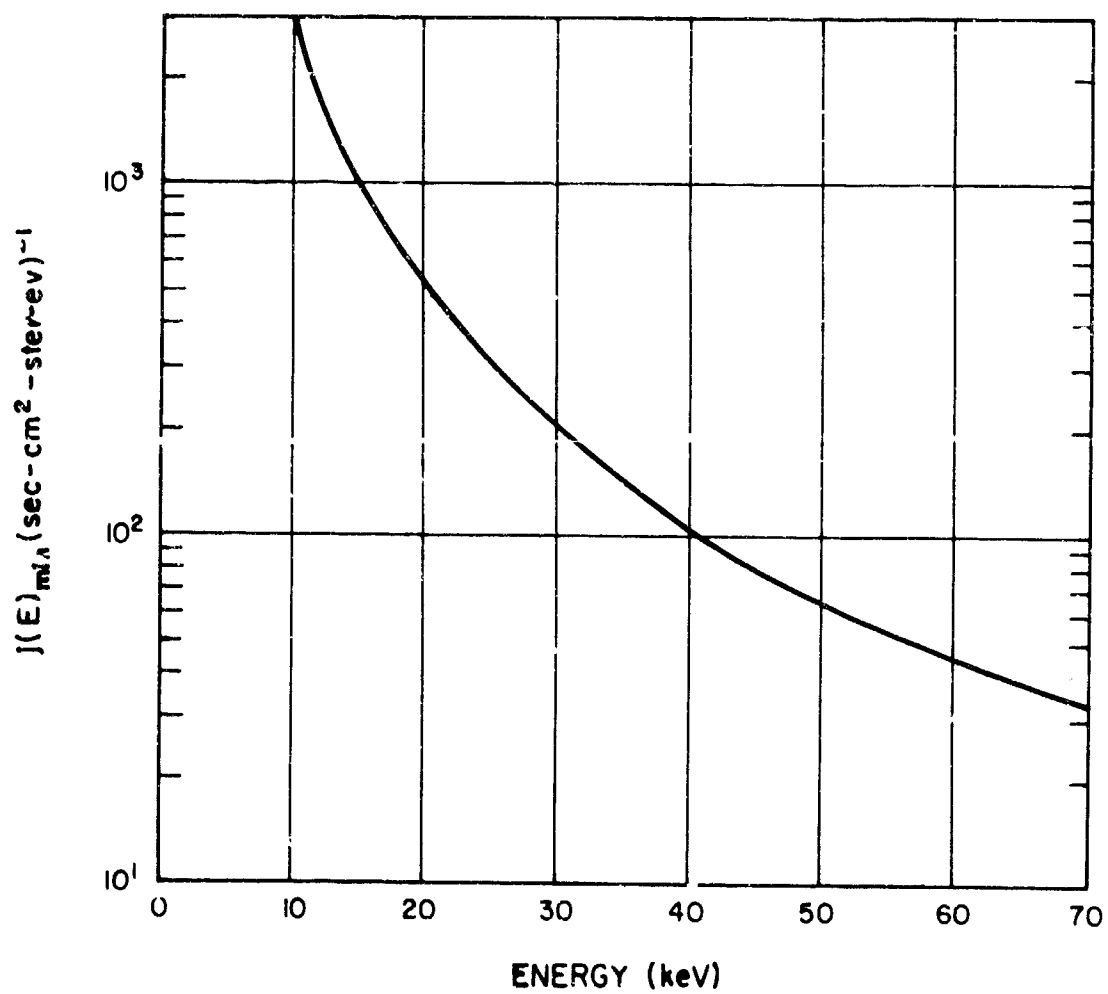
The OAR O'3-2 satellite was launched on October 28, 1966 into a polar orbit (82° inclination), the apogee perigee was 1600/325 kilometers. Perigee at launch was 15° N and the position of apogee perigee shifted northward approximately 3° /day. Local time at equatorial crossings increased at the rate of approximately 8 minutes per day. The spin rate was 4 rpm and the satellite initially had negligible precession. Figure 2.36 shows the orientation of the two electrostatic analyzers with respect to

Values in parentheses - full scale - full scale = 5 Volts

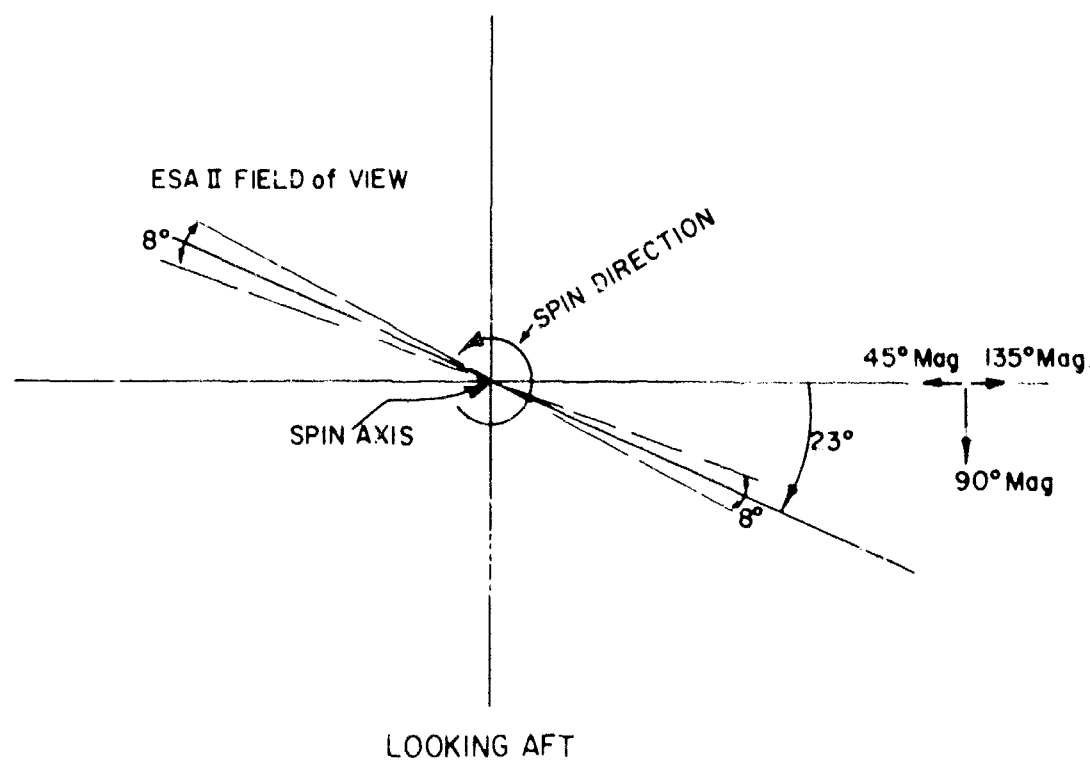
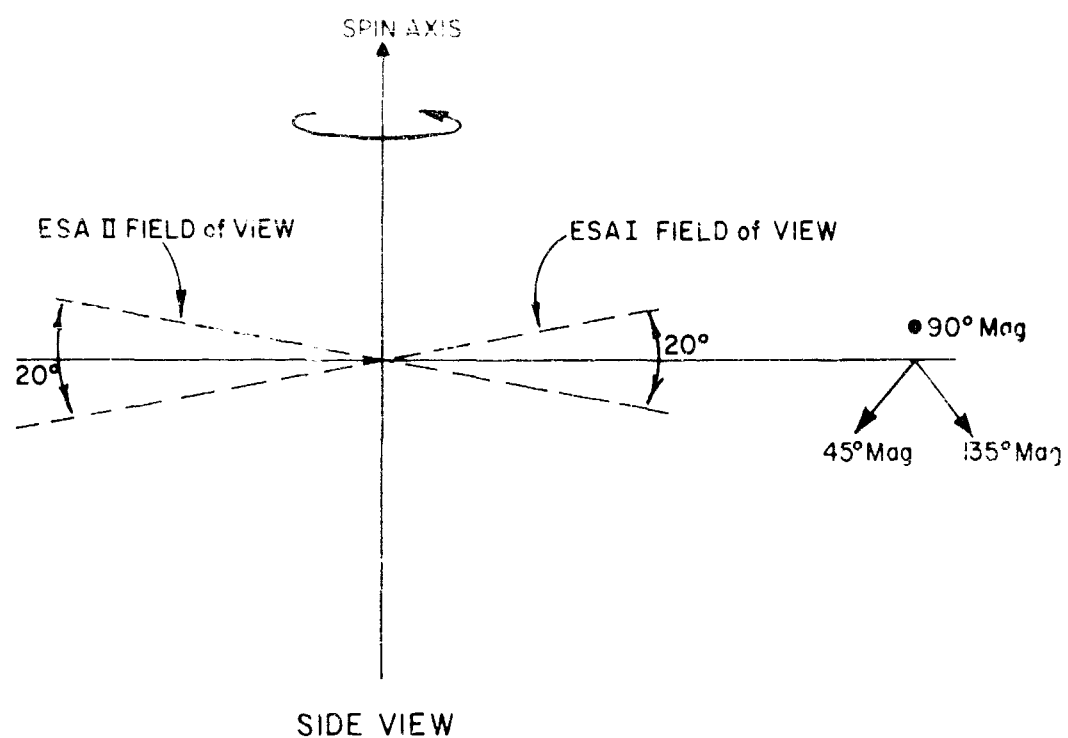
Values in parentheses - full scale - full scale = 5 Volts

[illegible]

MINIMUM DETECTABLE FLUX



SKETCH OF ESA ORIENTATION



the satellite axes. Figures 2.37 and 2.38 define the orientation of the satellite.

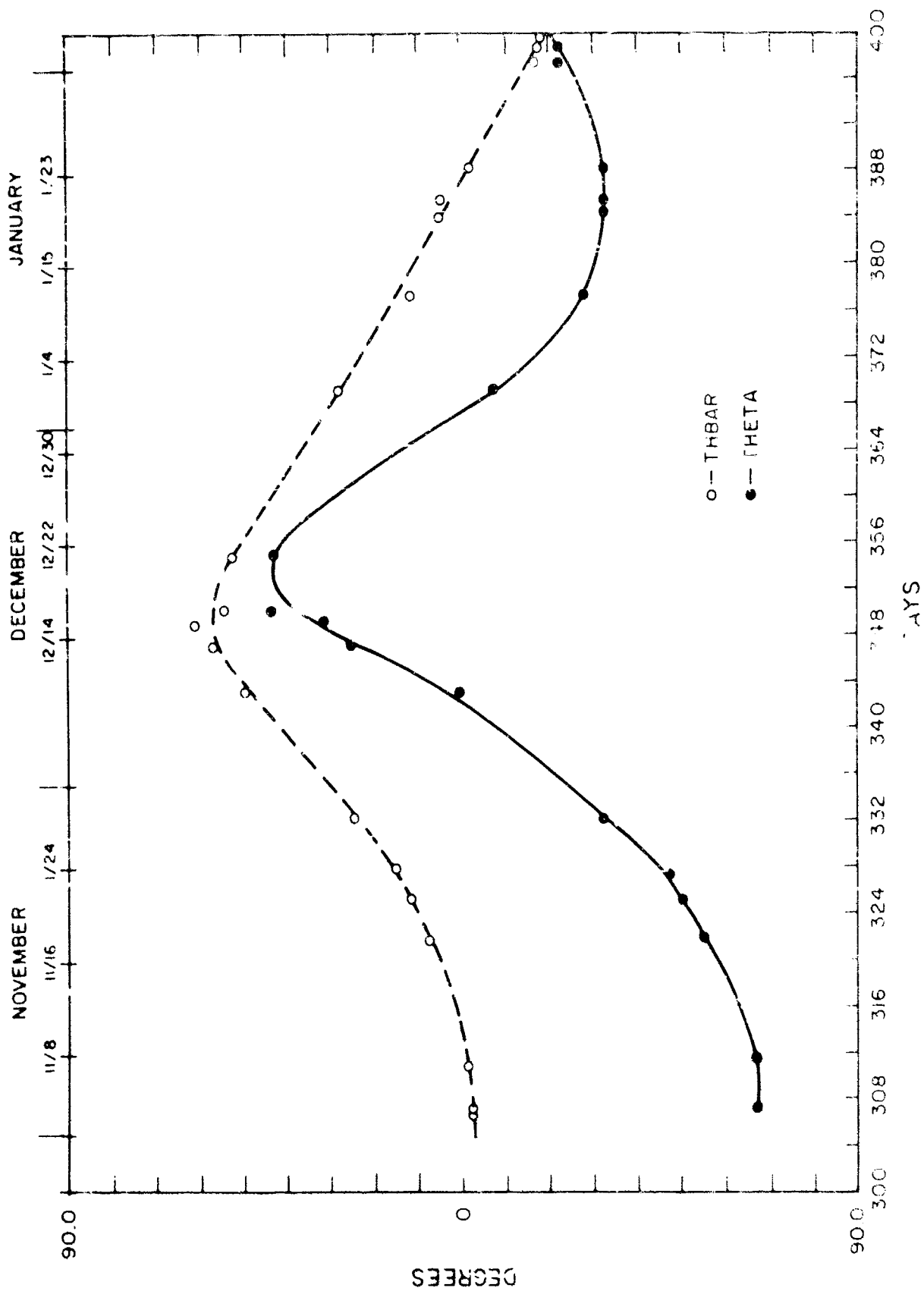
DEFINITIONS

Theta is the complement of the angle between the satellite axis and the normal to the equatorial plane.

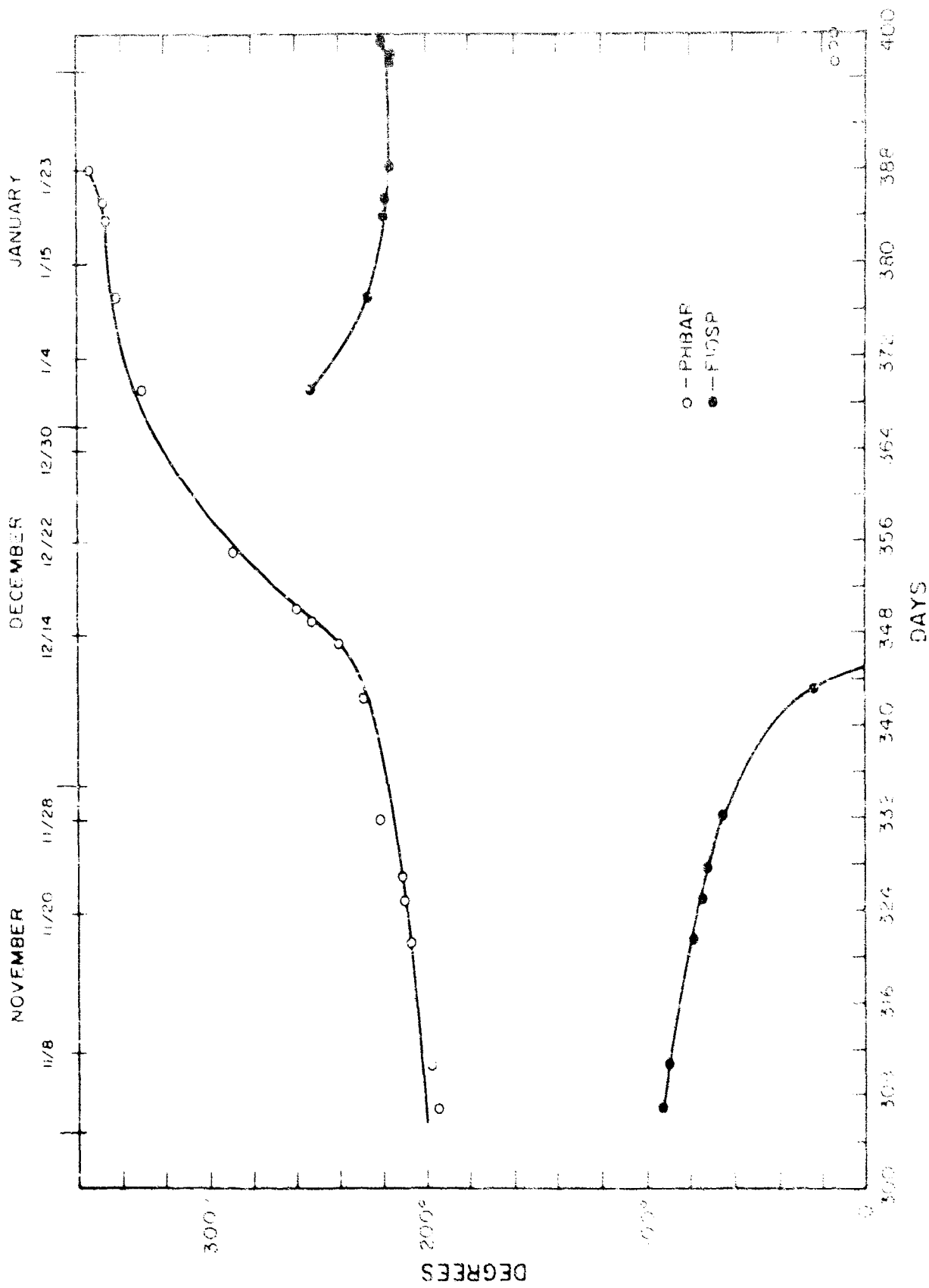
Thbar is the complement of the angle between the satellite axis and the normal to the orbital plane.

Phbar is the angle between the projection of the axis in the equatorial plane and the line of intersection of the orbital plane with the equatorial plane.

FIOSP is the longitude of first intersection between orbital and spin plane noting ascending or descending position on orbit.



ORBITAL PARAMETERS THBAR AND THETA AS FUNCTION OF TIME



ORBITAL PARAMETERS FIOSP AND PHBAR AS A FUNCTION OF TIME

BLANK

3.0 Data Reduction and Analysis

In the period from launch (28 October 1966) to 22 February 1967, when the recording and playback system failed, data was tape recorded on board and subsequently readout by ground command. A single readout corresponds to approximately 1-1/2 orbits of data. Subsequent to this failure, arrangements were made with the Churchill Research Range to record realtime data transmission when the satellite was within range and to make simultaneous ground based auroral measurements. These two groups of data will be discussed separately in the following sections.

3.1 Tape Recorded Data

The OV3-2 satellite is designed to obtain 1-1/2 orbits of tape recorded data on ground command. The command system was designed so that initiation of data recording could be delayed by three or six hours or could commence immediately after the command. Data would be recorded for the available recording time (approximately 2-1/2 hours). The recorded data was then stored until it was played back and transmitted on ground command. The playback speed was approximately sixteen times the recording speed.

The analysis of the OV3-2 data has been complicated by defective spacecraft clock and magnetometer systems. The spacecraft clock was subject to sudden spurious advances in time and the magnetometer flux was a factor of two below the calculated value. Because of these discrepancies it was generally not possible to use a routine computer program to determine satellite location at the time of data recording. However, an acceptable solution to the problem of determining the location and orientation of the satellite at the time of data recording was obtained using other available pieces of information: the satellite ephemeris, solar position

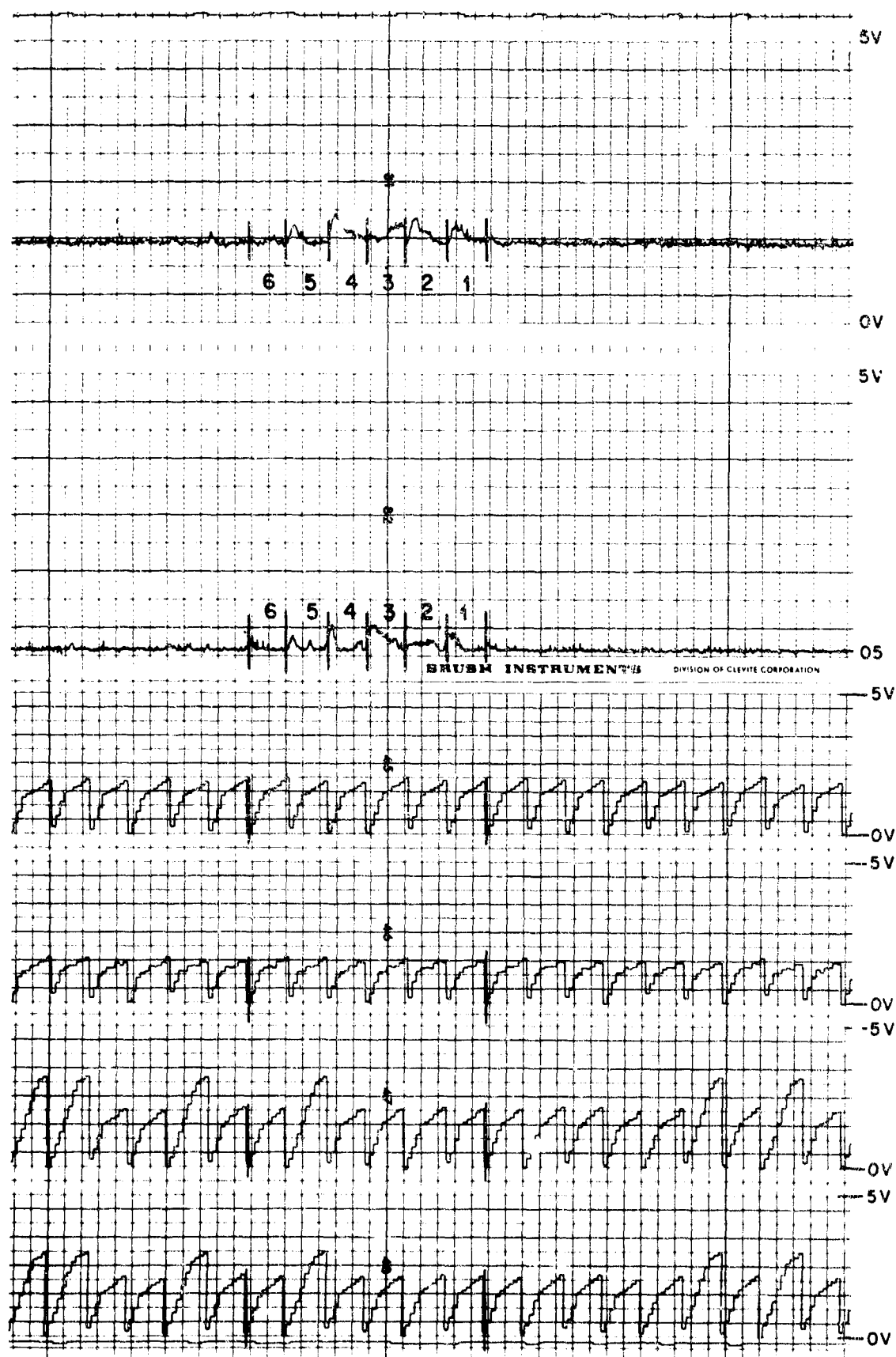
as measured by the sun sensor and realtime recording of the spacecraft clock when the tape record command is processed.

The tape recording and playback system functioned from 28 October 1966 (launch) to 22 February 1967. During this period tape recorded data was obtained for 60 orbits out of a possible 1636. The number of orbits from which data was obtained was limited by Air Force operational requirements unrelated to this experiment and difficulties with the command system. A satisfactory merge between the ephemeris and the recorded data is now available for twenty-nine orbits. Table 3.1 lists the present status of all tape recorded data obtained for the OV3-2 satellite. Work is continuing to obtain improved ephemeris merges.

The data and monitor outputs were sampled by a commutator, tape recorded on board and subsequently telemetered on command to the ground. The amplifier output for each ESA was sampled 10 times a second or 100 times per sweep while each plate high voltage monitor (and all other monitors) was sampled once a second. In analyzing the data it was first necessary to determine the start of a sweep. Since all high voltage supplies were driven by a common low voltage sweep, the sweep start was distinguished by observing a 1V or more change in any two successive plate high voltage monitor readings. Data obtained between the two successive monitor readings were discarded since it was not possible to determine the plate voltage in this period of time. Since the sweep voltage was designed to be a linear function of time, linear interpolation between monitor readings was used to determine plate voltage as a function of time. The calibration data (Section 2.2.3) were used to convert plate voltage to electron energy and to determine the photomultiplier output current from the measured signal voltage. The incident flux was then determined using the formulas and the calibration data in Section 2.2. A typical example is

O.V. 3-2 TAPE RECORDED DATA												
ORBIT PLAYBACK	ACTUAL ORBIT	DATE RECORDED AND 3 HOUR R	S-W EQUATOR CROSSING LOCAL TIME	S-W EQUATOR CROSSING LOCAL TIME	S-W EQUATOR CROSSING LOCAL TIME	LATITUDE OF PERIGEE	ANGLE BETWEEN SAT AXIS AND THE EQUATORIAL PLANE ELEVATION	ANGLE BETWEEN PROJECTION OF AXIS IN THE EQUATORIAL PLANE AND IN THE INTERSECTION OF ORBITAL PLANE WITH THE EQUATORIAL PLANE AZIMUTH	PLASMA PHONE (1) = ON (0) = OFF	REPRESENTS MERCELENT 2 FAIR 3 UNSATIS- FACTORY	MEASURABLE ELECTRON FLUX 2 WEAK POSSIBLY SPURIOUS SIGNAL 3 NO MEASURABLE ELECTRON FLUX	
							θ	γ				
74	61/62	11/1-2/66, 3+	0047	1547	224°	120°50'E			0	2	1	
90	74/75	11/2/66, 3-	2323	1523	244°	125°17'E			0	2	1	
101/102	90	11/3/66, 3-	0127		211°	120°17'E	-67	194	0	2	1	
102/103	101/102	11/4/66, 2-							0	2	1	
143	102/103	11/4-5/66, 2-	0903	1523	230°	133°01'E			0	3	2	
153	142	11/7/66, 3-	2130	1503	262°	140°18'E	-67	187	0	1	3	
163	172	11/9/66, 0+								3	3	
166	184	11/10/66, 2								3	2	
206/208	188	11/10/66, 2								3	1	
249/250	206/208	11/12/66, 1+	1429	1429	0°	154°00'E				1	1	
291	281	11/12/66, 3+	2119	1419	248°	167°07'E	-55	206		3	3	
294/295	292									1		
334	295	11/18/66, 3+				170°50'E			1	3	2	
348	337	11/21/66, 0+	0007	1320	273°	177°00'E	-50	210	1	2	3	
350	348/347	11/22/66, 0+	1413	1313	345	160°103'E	-32	215	1	3	3	
447	432	11/28/66, 5	0335	1235	258	177°30'E			1	1	1	
534	528	12/5/66, 1+	0035	1215	280	160°27'E			1	3	1	
542	534	12/6/66, 2+	0454	1141	103	157°11'E			1	3	3	
548	542	12/8/66, 1+	0836	1136	253	150°28'E			1	2	1	
558	548	12/7/66, 1+	0550	1101	97	155°103'E			1	3	2	
571	558	12/8/66, 1+	0854	1054	247°	160°28'E			1	3	2	
580/581	573	12/8/66, 3-							0	3	2	
589	581	12/10/66, 0+					0	229	0	2	1	
628	588	12/13/66, 1-	0441		103°	145°108'E			1	2	2	
638	630	12/13/66, 4-	0821	1042	110°	138°114'E	25	240	0	2	2	
644	636	12/13/66, 5+	0815	1037	235°	137°238'E			1	3	2	
658	658	12/14/66, 2	0029	1029	150°	134°133'E			0	3	1	
668	658	12/15/66, 3+	0857	1027	98°	133°100'E	31	253	1	1	1	
671	669	12/15/66, 2	2303		170°	134°153'E			1	3	2	
683	671	12/16/66, 2+	1231		117°	130°120'E			1	3	2	
752	683	12/16/66, 2	0818	1012	111°	137°17'E	42	25	1	1	2	
837	752	12/21/66, 2+	2304	0837	158°	115°180'E	42.5	288	1	1	1	
833	850	12/28-29/66, 3-							1	3	2	
845	833	1/3/67, 1+	0046	0745	110°	17°110'E			0	1	3	
950	845	1/4/67, 1	0355	0753	137°	23°14'E	-7.5	330	0	1	3	
969	858	1/5/67, 0+								3	3	
1024	1015	1/9/67, 2	2344	0714	120°	36°117'E			0	3	3	
1038	1024	1/10/67, 0+							1	2	3	
1068	1055	1/12/67, 1-	1947	0854	145°	44°150'E	-275	342	1	1	3	
1113	1069	1/13/67, 4+	2051	0851	150°	45°143'E			1	3	1	
1125	1113	1/17/67, 1+	0108	0808	78°	59°70'E			1	3	3	
1140	1125	1/17/67, 1	2157	0557	125°	50°18'E			1	1	3	
1151	1140	1/18/67, 1+	2358	0556	93°	60°82'E			1	1	3	
1165	1151	1/19/67, 2+	0800	0603	168°	61°13'E	-32.5	349	1	1	3	
1208	1165	1/20/67, 3+	0817	0556	180°	60°11'E	-22.5	349	1	1	2	
1222	1208	1/23/67, 1+	2449	0533	118°	74°11'E	-17.5	356	1	1	3	
1234	1222	1/24/67, 0+							1	1	3	
1248	1234	1/25/67, 1-							1	3	3	
1262	1248	1/26/67, 0	0908	0509	150°	79°10'E			1	1	3	
1332	1262	1/27/67, 1-	0825	0525	144°	82°60'E			1	3	3	
1346	1332	2/1/67, 0	2044	0428	115°	74°34'E	-22.5	14.5	1	1	3	
1358	1346	2/2/67, 1+	0027	0418	58°	71°280'E	-22.5	15.5	1	1	3	
1401	1358	2/3/67, 0	0747	0412	158°	60°11'E	-17.5	15.2	1	1	3	
1415	1401	2/6/67, 1	2008		112°	50°318'E			1	1	3	
1427	1415	2/7/67, 0-	2033	0333	107°	57°307'E			1	2	1	
1443	1427	2/8/67, 4-							1	3	1	
1498	1457	2/10/67, 0	2320	0320	90°	40°282'E			1	3	2	
1512	1498	2/13/67, 2	2021	0321	90°	38°280'E			1	3	3	
1525	1512	2/14/67, 1+							1	3		
1541	1525	2/15/67, 1-	0807	0307	114°	35°280'E			1	3	2	
1595	1534	2/17/67, 2							1	3	1	
1636	1622	2/22/67, 2+							1	3	1	

PLAY BACK ORBIT 101/102 RECORD ORBIT 90



shown in Figure 3.1 which is a strip chart recording of playback orbit 101/102 realtime orbit 90, showing the data output and the plate high voltage monitors for ESA-1 and -2. The three hour K_p index was 3⁻ and the calculated fluxes are shown in Figure 3.2. Since the satellite spin period is 15 seconds and the ESA sweep period is 10 seconds, a large range of pitch angles could be covered during a single sweep. The pitch angles covered for the two ESA's during 10 sweeps are shown in Figures 3.3 and 3.4 as a function of electron energy.

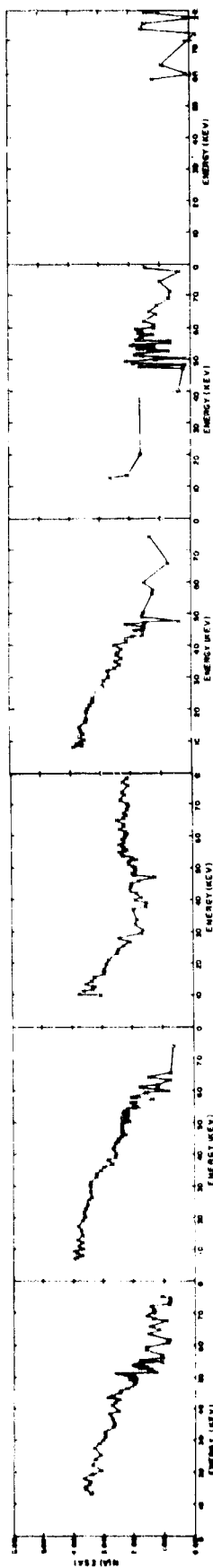
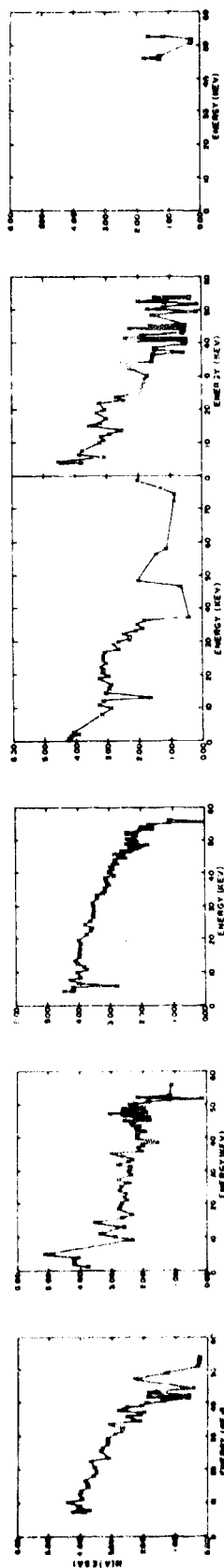
While the two ESA's measured electrons with pitch angles separated by 180° at any given time, they were not set to the same energy (Section 2.3). In order to measure the pitch angle distribution and the energy deposition it is necessary to assume that the incident spectrum does not change over several sweeps or to assume that the pitch angle distribution is energy independent. Both the data from OV3-2 and from the rocket results discussed in Section 3.2 indicate that these assumptions are of limited validity. However, from the distribution shown in Figure 3.3, it is clear that the "reflection coefficient" for this event

$$\left(\text{the ratio } \frac{\text{flux pitch angle} < 90^\circ}{\text{flux pitch angle} > 90^\circ} \right) \text{ is on the order of 10 to 20\%}$$

therefore, this event is a precipitation event and the deposited energy can be set equal to the incident energy within the accuracy of the instrumental calibration.

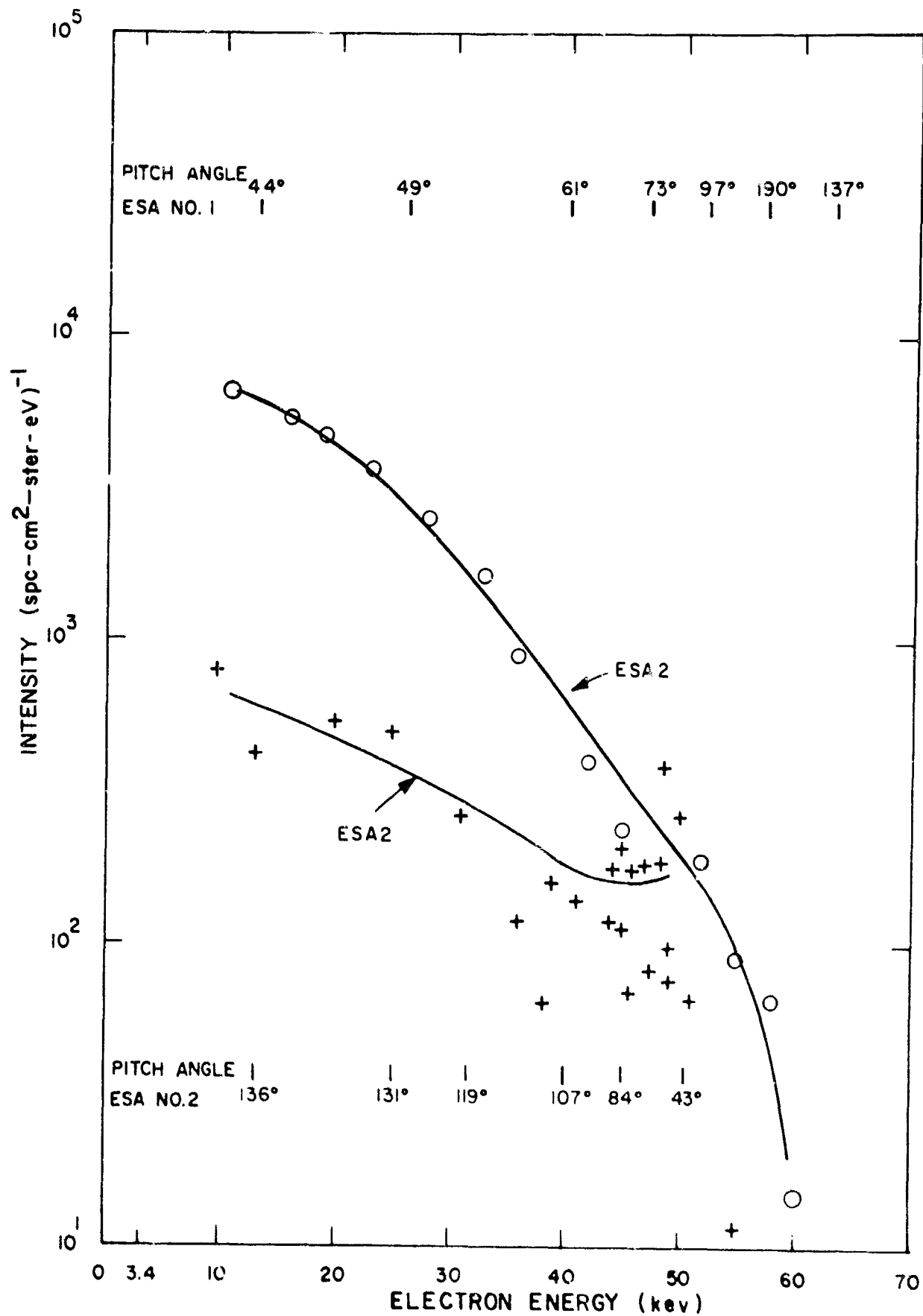
Preliminary results from this orbit and two other orbits in Appendix A which is a paper by E.R. Hegblom, W. Reidy and J. A. Sandock presented at the 49th Annual Meeting of the American Geophysical Union, Washington, 1968.

Table 3.2 lists the relevant parameters for the tape recorded orbits for which a satisfactory ephemeris merge (criterion 1 or 2) and measurable electron flux (criterion 1) were observed.

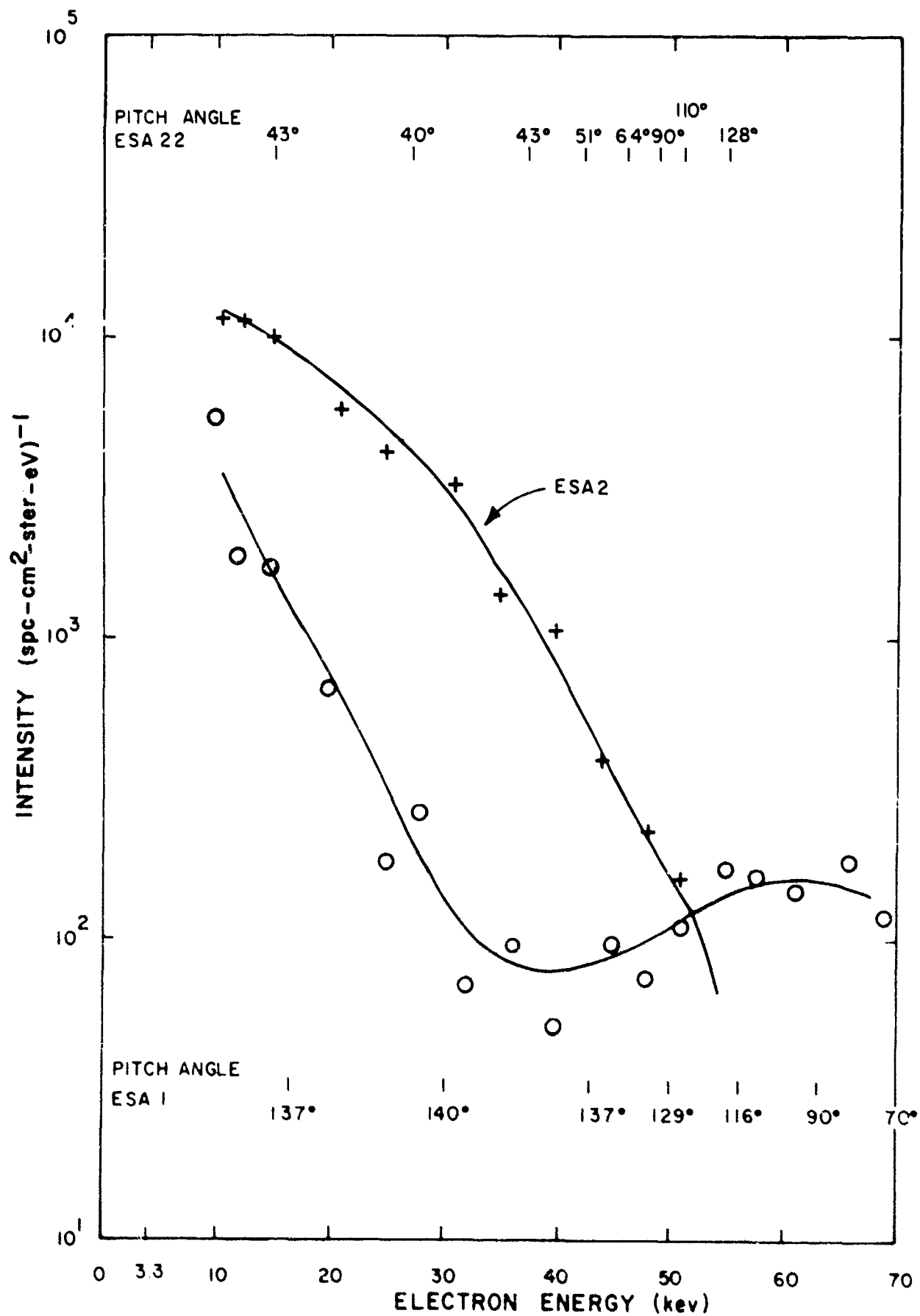


ELECTRON FLUX MEASUREMENTS-PLAYBACK ORBIT 101/102 **RECORD ORBIT 90**

COMPOSITE FLUX AND PITCH ANGLE DEPENDENCE SWEEP 2



COMPOSITE FLUX AND PITCH ANGLE DEPENDENCE SWEEP 3



Orbit Playback Record	Time of Playback (Universal Time) Hr: Min: Sec	Altitude km	Invariant* Latitude degrees	Geocentric* Latitude/Longitude degrees/degrees	Local Time* of Event Hr: Min:	Electron Flux Electron/cm ² sec ⁻¹ ster ⁻¹ eV ⁻¹	Spatial Extent (approximate)	Remarks
74	61 20:01:50 (72.210 sec)		N67	/E47		10 ³ at 20 keV	400 KM	Ephemeris questionable 3 hr Kp 3+
62	19:57:10 (71.830 sec)		N67	/E47		10 ⁴ at 10 keV	1000 KM	Electron flux extends over wide regions of northern night sky.
90	74 22:53:28 (86.008 sec)	563	N74	N78/E41	00:51	weak	70 KM	No measurable flux in southern hemisphere
	3:53:19 (79.997 sec)	489	N66	N70/E60	02:09	moderate	140 KM	Ephemeris questionable 3 hr Kp 3
	23:56:19 (87.871 sec)	454	064	S54/E85	04:23	strong spectra surtit	300 KM	
	23:46:45 (87.557 sec)	462	N67	N69/E34	02:12	peak flux 10 ⁴ spectra flat 10-30 keV	630 KM	

* Position approximately in center of measured event

ELECTRON FLUX MEASUREMENTS-TAPE RECORDER ORBIT

Orbit Playback Record	Time of Playback (Universal Time) Hr Min Sec	Altitude km	Invariant Latitude degrees	Geocentric Latitude/Longitude degrees/degrees	Local Time of Event Hr Min	Electron Flux $\text{cm}^{-2} \text{sec}^{-1} \text{ster}^{-1} \text{eV}^{-1}$ Electron ($\text{cm}^{-2} \text{sec}^{-1} \text{ster}^{-1} \text{eV}^{-1}$)	Spatial Extent	Remarks
102/103 191/102	22:35:-- (81.005 sec)	424	N65.6	N71/E72	1:51	$10^3 - 10^4$ at 1 ⁺ keV	560 KM	3 hr Kp 2 ⁻
239/240 208/209	20:24:12 (73.331 sec)	440	N76.5	N81/E37	19:1:51	---	200 KM	3 hr Kp 1 ⁺

ELECTRON FLUX MEASUREMENTS-TAPE RECORDER ORBIT

Orbit Playback Record	Time of Playback Hr. Min. Sec.	Altitude km	Invariant Latitude degrees	Geocentric Latitude/Longitude degrees/degrees	Local Time of Event Hr. Min.	Electron Flux		Spatial Extent	Remarks
						Electron (cm ⁻² sec ⁻¹ ster ⁻¹ ev ⁻¹)	Electron (cm ⁻² sec ⁻¹ ster ⁻¹ ev ⁻¹)		
447 412	20:04:40 (72.280 sec)	370	56.5	N74.6/E62.1	22:24	10 ⁶ at 10 keV		140 KM	3 hr Kp 5
	20:24:10 (72.271 sec)	400	56.5	N67.2/E72.8	22:12	5 x 10 ⁶ at 10 keV		300 KM	several weak events were also observed in daylight at L shells between 3.8 and 6.5
	19:57:58 (71.878 sec)	421	56.5	N67.4/E48.4	22:16	strong flux		300 KM	
449 501	3:11:38 (110.876 sec)	540	56.7	N64.8/E144	22:02	moderate flux at low energies (~10 ³)		630 KM	
449 614	22:03:17 (74.602 sec)	551	56.7	N66.6/E137	22:47	moderate		200 KM	3 hr Kp 3+
	22:11:17 (74.866 sec)	600	56.7	N66.6/E136.4	22:11	strong		420 KM	sunlit

1 ELECTRON FLUX MEASUREMENTS-TAPE RECORDER ORBIT

Orbit Playback Record	Time of Playback (U.S. Standard Time) Hr: Min: Sec	Altitude km	Invariant Latitude degrees	Geocentric Latitude/Longitude degrees/degrees	Local Time of Event Hr: Min:	Electron Flux Electron (cm ⁻² sec ⁻¹ ster ⁻¹ eV ⁻¹)	Spatial Extent	Remarks
837 752	01:28:13 (5,298 sec)	745	70°	S55/E150	8:50	~ 10 ³ at low energies	370 KM	3 hr Kp 1 ⁻ sunlit
	01:26:12 (5,172 sec)	590	70°	N73/E181	11:20	weak with some spurious signal	390 KM	sunlit
	01:25:31 (5,131 sec)	1074	73°	N65/E314	20:29	low energy spike ~ 10 ³	50 KM	
	01:22:22 (4,942 sec)	1112	74°	S82/E38	2:32	--	70 KM	sunlit
	01:21:41 (4,901 sec)	685	69°	S53/E125	8:52	---	290 KM	sunlit
1427 1415						substantial electron flux measured over appreciable portion of orbit		3 hr Kp 6 ⁻ orbit mainly sunlit, data obtained only in sunlit portion, ephemeris in- complete

ELECTRON FLUX MEASUREMENTS-TAPE RECORDER ORBIT

3.2 Real Time Transmission in the Auroral Zone

In addition to the tape recorded data, real time transmissions were obtained in the auroral zone by ground receiving stations at Kodiak, Churchill and Thule.

Since the satellite power system design did not permit continuous operation, it was necessary to shut-off the instrumentation at regular intervals to recharge. Initially this mode of operation was complicated by the fact that command receivers were not available at the three near auroral zone stations. Therefore, a single data recording required coordinated support by three ground stations; one for turn-on command, one for recording in the auroral region, and one for shut-down and recharge command.

While the initial real time auroral zone recording took place during orbit 1947 at Thule, very limited data was obtained until orbit 4667, approximately 11 months after launch, when a command transmitter was installed at the Churchill Research Range. Table 3.3 lists the periods of time and the corresponding three-hour K_p index when real time transmissions were recorded in the auroral zone.

Table 2.3 shows the performance of the ESA plate high voltages. Initially, the plate high voltage circuits and monitors were operating, however, by the time appreciable real time transmission was available (e. g., orbit 4778), both plate voltage circuits were severely degraded.

In the degraded operation it is not possible to verify whether the high voltage sweep circuit, the sweep monitor circuit or both are defective,

TABLE 3. 3
REAL TIME TRANSMISSIONS
IN THE AURORAL ZONE
CHURCHILL STATION

ORBIT	DATE			START (UT)	STOP (UT)	3HR. K _p	REMARKS
	M	D	Y				
2916	5	26	67	1858	1910	4-	SN
2917	5	26	67	2038	2050	4	SN
2930	5	27	67	1908	1920	2-	S flux observed
2930	5	27	67	2013	2025	2-	S very weak flux
2944	5	28	67	1918	1930	6	SN
4625	9	26	67	0442	0454	0	noisy
4639	9	27	67	0444	0456	1+	N
4653	9	28	67	0448	0500	5-	N
4667	9	29	67	0443	0455	5+	noisy record electron flux
4681	9	30	67	0450	0502	4+	weak flux
4722	10	2	67	0305	0317	1	N
4723	10	2	67	0446	0458	1	very weak flux narrow region
4724	10	2	67	0631	0643	1	N
4736	10	3	67	0310	0322	2	N
4764	10	6	67	0305	0317	3	N
4778	10	7	67	0305	0317	1+	weak flux noisy
5607	12	5	67	0714	0718	1-	
5621	12	6	67	0710	0717	2+	
5635	12	7	67	0706	0711	4-	
5649	12	8	67	0704	0708 (-1508)	4+	electron flux observed

* S - sunlit

N - no observed electron flux

TABLE 3. 3 (Continued)

CHURCHILL STATION

ORBIT	DATE			START (UT)	STOP (UT)	3HR. K _p	REMARKS
	M	D	Y				
5663	12	9	67	0700	0705	2-	N
5691	12	11	67	0650	0700	0	instrument off
5699	12	11		2010	2016	?	
5705	12	12	67	0645	0652	1	
5713	12	12	67	2014	2020	2-	
5719	12	13	67	0644	0656	1	
5733	12	14	67	0641	0649	1	
5747	12	15	67	0635	0645	1	
5761	12	16	67	0634	0643	1	
5789	12	18	67	0624	0632	4	
5802	12	19	67	0437	0445	4	
5803	12	19	67	0620	0630	4	electron flux observed
5816	12	20	67	0433	0441	5	N
5817	12	20	67	0616	0625	4	very large electron flux
5830	12	21	67	0429	0437	3	N
5831	12	21	67	0611	0621	2	N
5844	12	22	67	0424	0431	2	N
5845	12	22	67	0605	0617	3	electron flux observed
5914	12	27	67	0401	0409	1	N
5915	12	27	67	0543	0553	1	N
5928	12	28	67	0354	0404	1	N
5929	12	28	67	0537	0547	1	N
5942	12	29	67	0348	0359	2	
5943	12	29	67	0531	0542	1	

TABLE 3. 3 (Continued)

CHURCHILL STATION

ORBIT	DATE			START (UT)	STOP (UT)	3HR. K _p	REMARKS
	M	D	Y				
6027	1	4	68	0458	0506	1	N
6040	1	5	68	0304	0319	2	
6041	1	5	68	0451	0501	2	
6054	1	6	68	0300	0315	3	
6055	1	6	68	0445	0455	3	
6082	1	8	68	0356	0400	1	
6083	1	8	68	0432	0445	1	
6096	1	9	68	0242	0254	0	
6097	1	9	68	0428	0438	0	
6110	1	10	68	0236	0249	2	
6111	1	10	68	0416	0431	2	
6124	1	11	68	0236	0248	1	
6125	1	11	68	0418	0430	1	
6138	1	12	68	0221	0233		
6152	1	13	68	0213	0225	3	
6153	1	13	68	0355	0407	3	N
6180	1	15	68	0200	0212	2	
6181	1	15	68	0341	0353	2	
6194	1	16	68	0151	0203	3	very weak electron flux
6195	1	16	68	0334	0346	2	
6208	1	17	68	0143	0155	2	
6209	1	17	68	0326	0338	3	
6222	1	18	68	0136	0148	2	
6223	1	18	68	0321	0333	2	
6377	1	29	68	2358	0010	4	

TABLE 3. 3 (Continued)

CHURCHILL STATION

ORBIT	DATE			START	STOP	3HR. K _p	REMARKS
	M	D	Y	(UT)	(UT)		
6390	1	30	68	2213	2225	2	
6391	1	30	68	2253	0005	2	
7128	3	22	68	0748	0800	1	
7156	3	24	68	0715	0725	4-	electron flux observed
7184	3	26	68	0651	0703	3-	electron flux observed
7311	4	4	68	0318	0330	3-	
7325	4	5	68	0310	0322	2	
7339	4	6	68	0553	0605	5-	electron flux observed
7395	4	10	68	0452	0504	2+	
7409	4	11	68	0436	0448	2-	
7423	4	12	68	0418	0430	2-	
7480	4	16	68	0502	0514	3-	electron flux observed
7622	4	26	68	0358	0410	3+	
7636	4	27	68	0338	0350	3	
8260	6	10	68	0530	0542		
8262	6	10	68	0753	0805		
8276	6	10	68				
8283	6	10	68				
10365	11	7	68				
10366	11	7	68				
10367	11	7	68				
10379	11	8	68				
10380	11	8	68				
10381	11	8	68				

TABLE 3. 3 (Continued)

CHURCHILL STATION

ORBIT	DATE			START (UT)	STOP (UT)	3HR. K _p	REMARKS
	M	D	Y				
10393	11	9	68				
10394	11	9	68				
10395	11	9	68				
10407	11	10	68				
10408	11	10	68				
10409	11	10	68				
10422	11	11	68				
10423	11	12	68				
10493	11	15	68				
10563	11	19	68				
10564	11	20	68				
10565	11	20	68				
10570	11	20	68				
10593	11	22	68				

POGO STATION - THULE

1947	3	17	67	?	?	1	
1988	3	20	67	0235	0250	3	
2002	3	22	67	0245	0300	2	
2099	3	28	67	0220	0235	1	
2113	3	30	67	0230	0245	3	
2182	4	4	67	0135	0150	1	
2280	4	10	67	0100	0115	2-	
2916	5	26	67	1905	1930	0	SN
2917	5	26	67	2045	2115	0	N

TABLE 3. 3 (Concluded)

POGO STATION - THULE

ORBIT	DATE			START (UT)	STOP (UT)	3HR. K _p		REMARKS
	M	D	Y					
2930	5	27	67	1910	1935	1		S electron flux observed
2944	5	28	67	1915	1945	1		SN
4625	9	26	67	0445	0510	0		
4639	9	27	67	0445	0510	1		
4653	9	28	67	0445	0515	5-		
4669	9	29	67	0815	0845	5+		
4681	9	30	67	0450	0515	4+		S electron flux observed
4767	10	6	67	0310	0335	3		
4778	10	7	67	0310	0335	1+		
4779	10	7	67	0450	0520	1+		

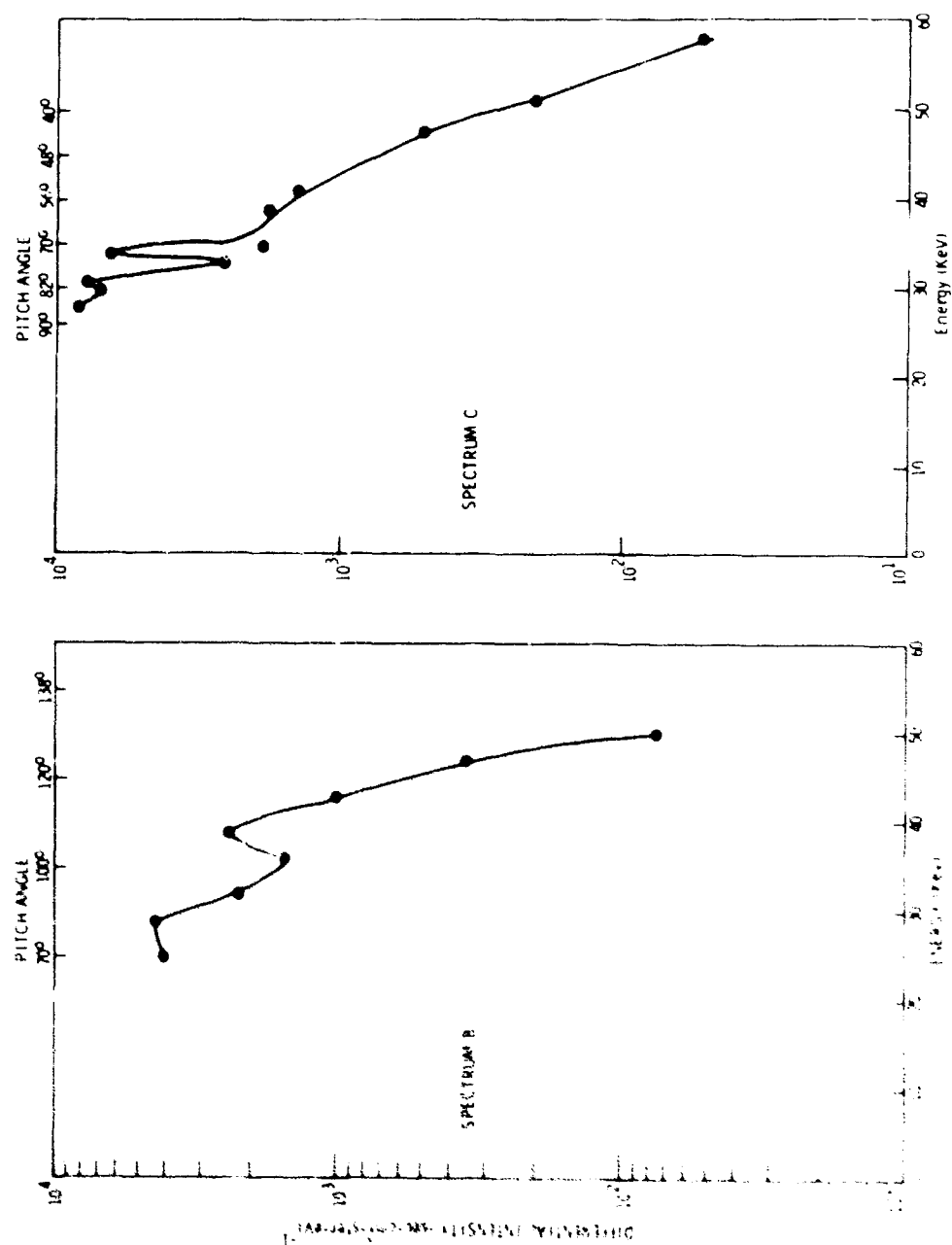
and therefore, it is not possible to accurately determine the energy at which the electron flux is measured. However certain reasonable assumptions can be made to assist in the analysis of the data.

(1) A likely mode of failure is burning out of the light bulb used in the plate high voltage power supply feed back circuit (Ref. Section 2.3). With this failure the output voltage will sweep over a narrower voltage interval starting at the high end of its normal operating range. Therefore, when this is observed it is assumed that the monitor is operating properly.

For example consider orbit 5817, (Table 2.3) the plate sweep monitors indicate that for ESA-2 the positive plate sweep is operating in this mode, while the negative sweep is operating properly though at somewhat higher than normal voltage. The data can be reduced on the assumption that the monitors are correct and Figure 3.5 shows the results for two successive spectra measured with ESA-2 during that orbit in the vicinity of the Churchill Research Range. However, the monitor readings for ESA-1 cannot be interpreted in this manner and additional assumptions must be made.

(2) Spurious signals can be eliminated by requiring that the electron flux exhibit a reasonable pitch angle dependence.

(3) If the plate voltage is sweeping it will sweep from high to low voltage, therefore, the lowest energy electrons will be observed at the end of the sweep. From a preliminary examination of the data it appears that there is always a discontinuity in the electron signal at the beginning of the sweep. This indicates that the measured electron spectrum changes over the sweep. In addition, this indicates that the plate voltages do not go to zero, but must be in excess of the voltage required to transmit 8 keV electrons, which is the low energy electron cutoff produced by the aluminum deposition on the scintillator. Both the instrument monitors and previous operations performance



DIFFERENTIAL ENERGY SPECTRA (OV3-2)
REAL TIME - ORBIT 5817

indicate that the electron energy at the low energy end of the sweep does not exceed 30 keV. The fact that the plate voltage is not zero at the end of the sweep is also proof that the plate high voltage sweep circuits are not properly functioning.

(4) The spectra measured in later orbits will be consistent with earlier measurements which indicate the auroral electron flux between 10 and 30 KeV can be characterized by an exponential spectrum ($N = N_0 e^{-E/E_0}$) with e-folding values (E_0) between 8 and 30 keV.

For the purpose of this analysis, one can choose average values of $E = 20$ and $E_0 = 20$ keV corresponding to the average photomultiplier current measured during the last seconds of the sweep. Using the formulas in Section 2.2.3, for electron energies sufficiently greater than E_L and photomultiplier output currents sufficiently above I_m , the relationship between photomultiplier current (I) and incident flux (N) is $N = kI/E^2$ where k is the appropriate numerical constant. At 20 keV the assumed analyzer value at the end of the sweep $N_{(20)} = N_{0e}^{-E/20} = kI/(20)^2$.

Consider the effect of improper choice of E and E_0 then

$$N_{(E)}^* = N_0 e^{-E/E_0} = k/E^2 \quad \text{where} \quad 8 \leq E_0 \leq 30$$

$$10 \leq E \leq 30$$

where $N_{(E)}^*$ is the correct value of the flux at the unknown energy E to which the analyzer is set.

The correct value of the flux at 20 keV $N_{(20)}^*$ is given by

$$N_{(20)}^*/N_{(E)} = e^{(E-20)/E_0}$$

The ratio of correct flux at 20 keV to the value based on the assumption that $E = E_0 = 20$ keV is

$$N_{(20)}^*/N_{(20)} = e^{(E-20)/E_0} (20/E)^2$$

This ratio can be evaluated for the extremum values of E and E_0 .

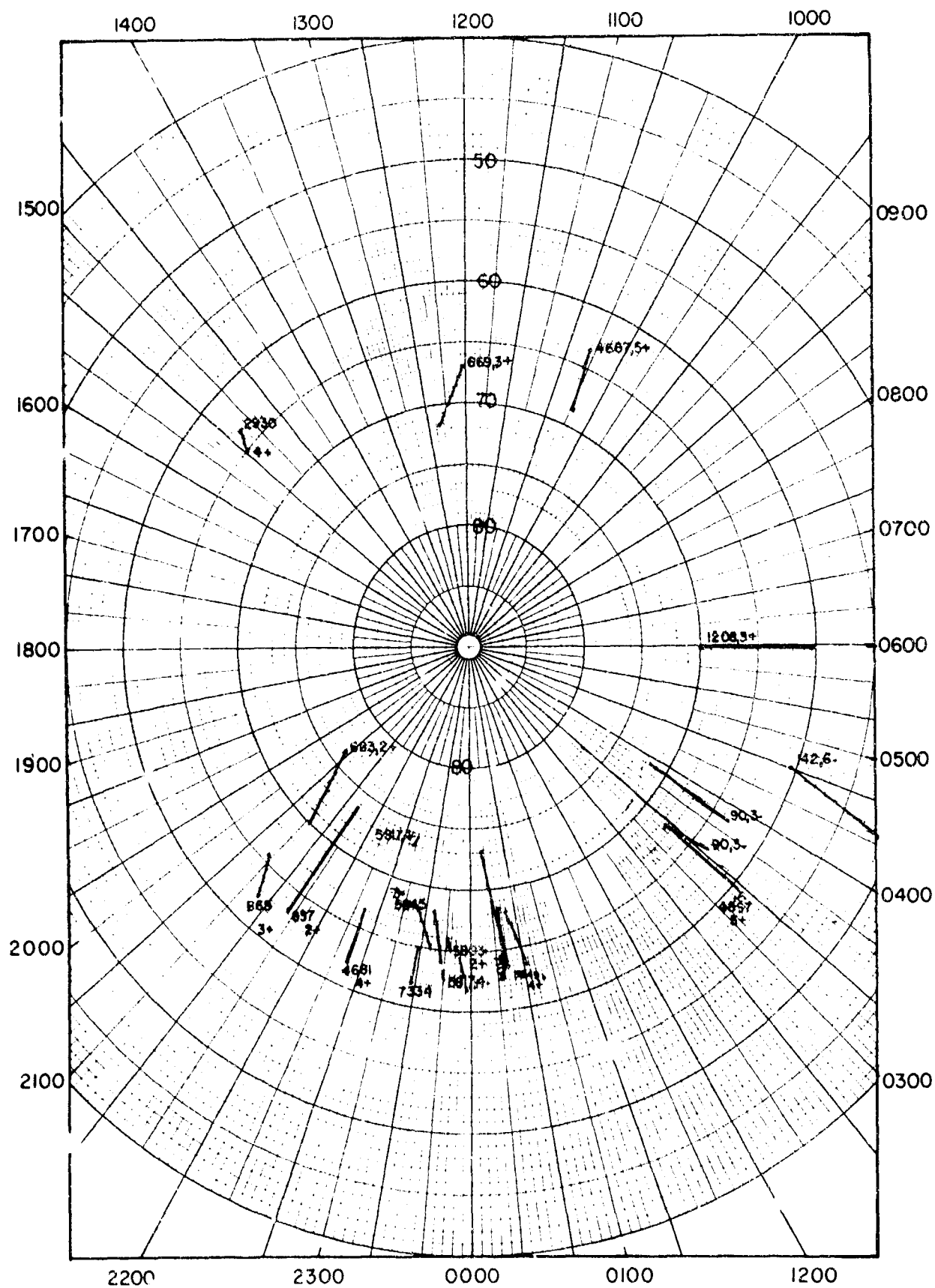
E_0	E	$N_{(20)}^*/N_{(20)}$
8	10	1.2
8	30	1.6
30	10	2.8
30	30	0.6

Therefore, this method of analysis appears to be sufficiently accurate to calculate the flux at 20 keV within a factor of three.

3.3 Spatial Distribution

Figure 3.6 shows the location of the electron fluxes measured by the OV3-2 satellite. The solid lines indicate the portion of the orbit in which measurable flux was observed in the northern hemisphere. The orbit number and the 3 hour K_p index is adjacent to the line. The data is plotted as a function of local time and geomagnetic latitude. Because of the difficulties in obtaining an accurate merge this data must be considered preliminary. However, the locus of the lines shown should constitute a reasonable approximation to the position of the auroral oval during active

DISTRIBUTION OF ELECTRON MEASUREMENTS IN LOCAL TIME AND GEOMAGNETIC LATITUDE



Of particular importance will be the correlation between the electron flux measurements on OV3-2 and the spatial structure observed in the ionization density in the auroral zone. This structure can be observed in the high latitude ionization profile in Figure 3 of Appendix B to this report. An accurate merge is required for detailed correlation of this type.

BLANK

PART II

ROCKET MEASUREMENTS OF AURORAL ELECTRONS

1.0 INTRODUCTION

Astrobee rocket 15.735 was launched from Churchill Research Range on 14 December 1966 during the breakup phase of a strong aurora. It was instrumented with an electrostatic analyzer to measure the incident electron differential electrode flux in the energy region from 26 to 35 keV. In addition, data was obtained with two other instruments on the rocket, a thin window ionization chamber counter to measure the total rate of energy deposition, and a retarding potential analyzer to measure the electron and ion density. The Aerobee rocket 15.735 was launched thirty seconds after Astrobee 3.615³ which was also instrumented for auroral measurements. Coordinated analysis of the measurements obtained from instruments on both rockets should provide a comprehensive view of the auroral distribution.

This section of this report will be directed to the analysis of data obtained with the electrostatic analyzer and, corroborative data, the thin window ionization chamber. These instruments are briefly described in Section 2.0 and are described in detail in ASE-1211 (AFCRL-66-275) Final Report, An Electrostatic Analyzer to Measure Auroral Electron Energy and Angular Distribution, 28 March 1966 and ASE-1244 (AFCRL-66-301) Final Report, Instrumentation to Measure the Rate of Ion Production in the Upper Atmosphere during an Aurora, 22 April 1966. Preliminary results obtained with this data have been published by Reidy, Hegblom, and Ulwick and were presented in ASE-1764 (AFCRL-67-0618) Final Report, Rocket Measurements of Low Energy Auroral Electron Energy Spectra, 31 October 1967.

A discussion of the coordinated measurements from the two rocket payloads is contained in a paper by Ulwick, Baker, and Hegblom which is Appendix C to this report.

2.0 INSTRUMENTATION

The electron flux measurements were made with an electrostatic analyzer designed to measure the electron flux over the energy range from approximately 1 to 40 keV. Each spectral measurement required 350 milliseconds, and the energy resolution of the instrument was 19%. The electrostatic analyzer consisted of a pair of concentric spherical octants with the inner plate grounded and a negative sweep voltage applied to the outer plate. The sweep voltage decreased exponentially from approximately 4 kV to 50 V in 0.35 seconds and was chopped, at a frequency of 1 kc/sec, to modulate the electron current transmitted through the analyzer plates. The electrons were detected by a scintillator (CsI(Tl) in the flights at Fort Wainwright, and $\text{CaF}_2(\text{Eu})$ in the flight at Fort Churchill) which was optically coupled to an EMR 541-D photomultiplier. A thin aluminum coating ($\sim 2500 \text{ \AA}$) on the face of the scintillator prevented light from reaching the photomultiplier. To extend the response of the instrument to lower energies, a potential (typically 6 kV) was applied to the aluminum coating to accelerate the electrons. A temperature compensated logarithmic amplifier with a narrow bandpass filter, which was tuned to the 1 kc/sec plate modulation frequency, measured the photomultiplier current. The amplifier output was rectified, integrated (0.01 second time constant), and telemetered to a ground station. The sweep, post-accelerator, and photomultiplier high voltages as well as all of the low voltage supplies and the temperature were monitored throughout the flights.

The differential intensity $j(E) (\text{cm}^2\text{-sec-sr-eV})^{-1}$ of electrons of energy E was calculated from the measured photomultiplier current I through the equation

$$j(E) = \frac{I}{(S) (KE) (A \Omega) (E + E_{pa} - E_L) (1 - K_b R_b)}$$

S, the sensitivity of the photomultiplier and scintillator, is the ratio of photomultiplier output current to the rate of energy deposition in the scintillator. In reducing the data we have used the results of Collinson and Hill⁴ for the variation of S with electron energy in CsI and we have calculated the energy dependence in CaF_2 using the X-ray data of Aitken⁵. The absolute value of S was obtained by measuring the response to a calibrated Am^{241} source and multiplying this by the known ratio of electron to alpha scintillation efficiency at a fixed electron energy⁶.

K_b is the inherent energy resolution of the plates (5%) measured with an electron beam over the energy range from 2 to 15 keV, and is in agreement within 20% of the value calculated from the dimensions of the plates using the results of Paolini and Theodoridis (Appendix D).

$A \Omega$, is the geometric factor ($= .09 \text{ cm}^2\text{-steradian}$) calculated from the area of the viewing aperture (3 cm^2) and the angular response ($6 \frac{1}{2}$ degrees by 16 degrees) measured with a low energy electron beam.

E_{pa} , represents the energy acquired by the electrons due to the post accelerator potential applied to the aluminum coating and E_L is the average energy loss per incident electron in the aluminum coating calculated from the measured aluminum thickness. For values of E_{pa} higher than E_L the instrument noise level increased significantly with increasing E_{pa} and to maximize the instrument sensitivity E_{pa} was set between 0 to 1 keV higher than E_L for each of the instruments.

K_b , is the fractional mean energy of the electrons backscattered by the scintillator and R_b is the fraction of the incident electrons back-scattered.

An electron beam was used to measure the response of a typical aluminum coated CsI scintillator for values of $(E + E_{pa})$ from 1 to 12 keV. These measurements were used to determine E_L and the energy dependence of the function $S(E + E_{pa} - E_L) (1 - K_b R_b)$. The variation between the calculated and measured energy dependence of this function is within the limits set by the uncertainty in E_L and in the energy dependence of S . Due to this uncertainty, there is an energy dependent systematic error in the calculated flux which is less than a factor of two at 2 keV, less than 30% at 5 keV, and less than 20% at 10 keV.

The rate of energy deposition by the auroral electron was also measured by an ion chamber on the Astrobee rocket. The ionization chamber was filled with 90% nitrogen and 10% methane at a total pressure of 10 cm of Hg. The average range of 20 keV electrons. The cathode high voltage was adjusted so that the chamber operated in the proportional region with a gain of about 90. The anode current was chopped at a 400 cps rate and measured by a temperature compensated logarithmic amplifier with an input range from 5×10^{-11} to 5×10^{-5} amperes (10^{-3} ergs/cm² sec. to 10^3 ergs/cm² sec). This chamber window was formvar, 1600 Å thick, (equal to the range of 1.6 keV electrons), with an area of 0.5 cm², and supported by a nickel mesh with 77% transmission. The field of view was conical with a 60° half angle and its center made an angle of 60° with the rocket axis and was located on the opposite side of the rocket from the electrostatic analyzer.

In-flight calibration of the ion chamber was achieved by mounting a two-microcurie Radium 226 source on a door in front of the entrance aperture and measuring the output current. This calibration source was removed when the door opened at 60 km.

The chamber pressure, door position, cathode voltage, and the low voltage supplies were monitored throughout the flight.

BLANK

3.0 DATA REDUCTION AND ANALYSIS

Figure 3.1 shows the trajectory for the two rockets.

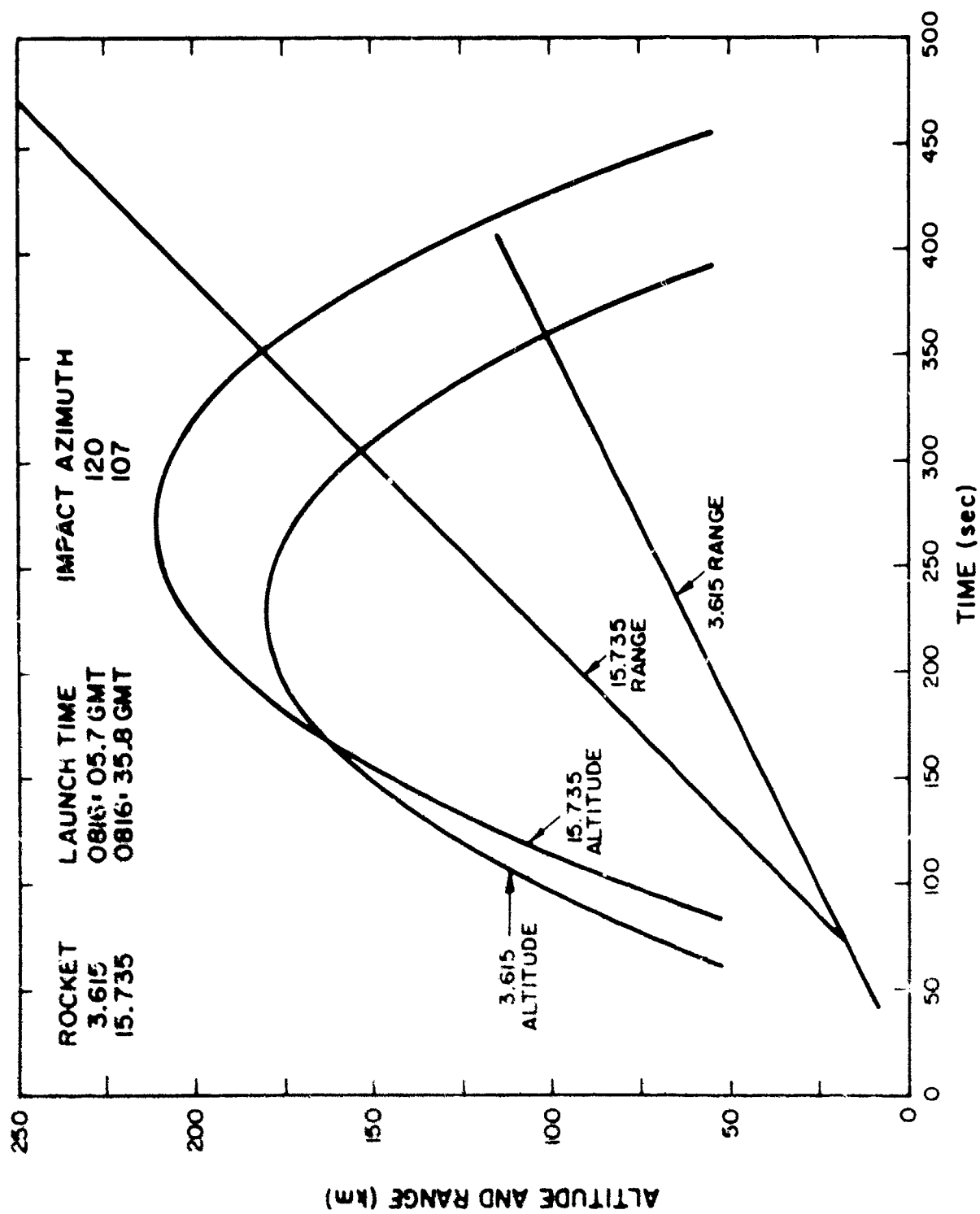
Figure 3.2 shows the rate of energy deposition measured with the ion chamber as a function of time and also the angle between the center of the field of view and the magnetic field (particles with 0 degree pitch angle precipitated into the atmosphere along the magnetic field line). The rate of energy deposition has been corrected for the energy lost in the window by electrons, assuming the exponential spectral form which was measured by the electrostatic analyzer.

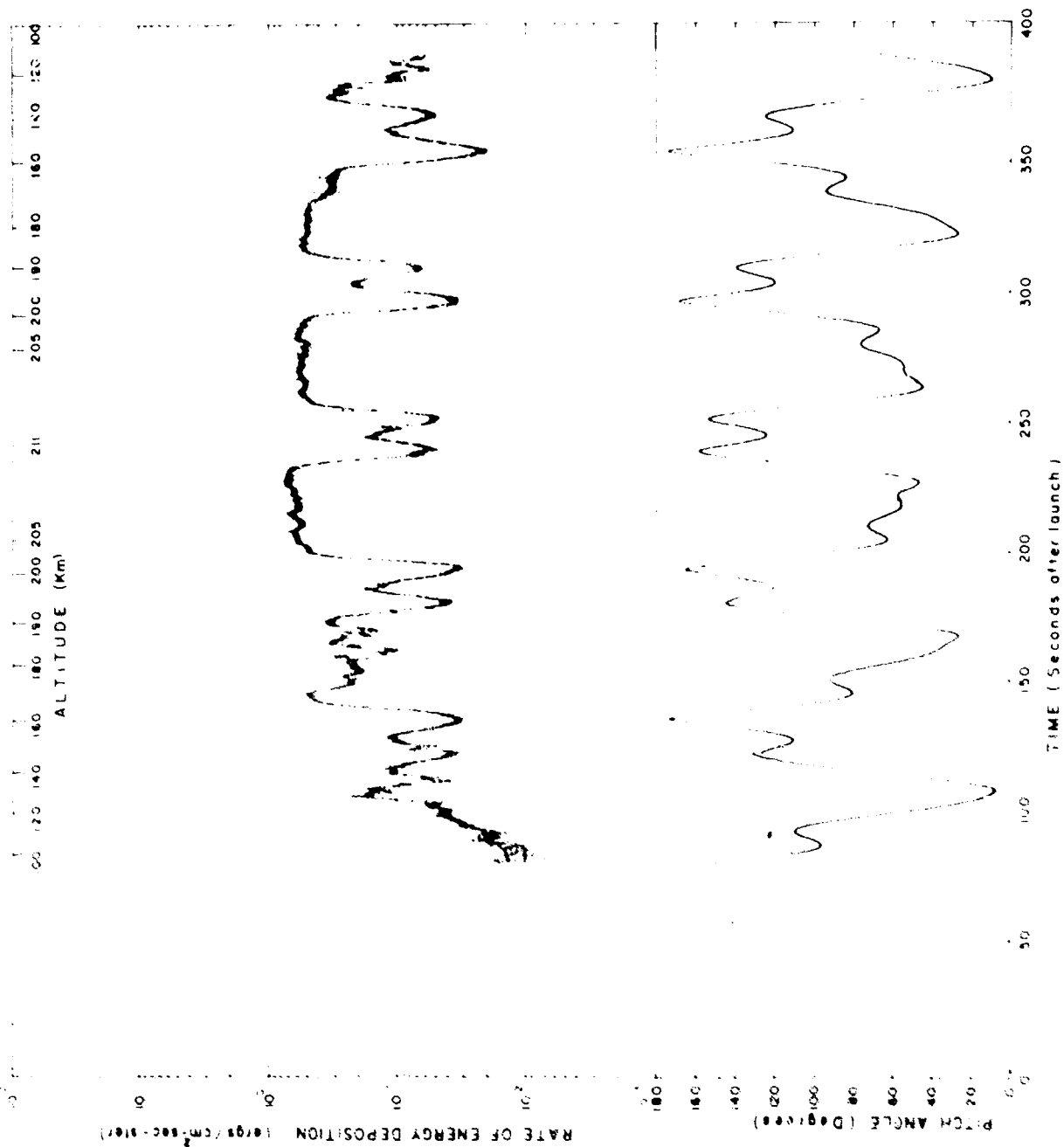
From 200 to 330 seconds, the incident energy flux measured by the ion chamber is relatively constant in agreement with the electrostatic analyzer measurement.

Although the field of view is quite wide, there is a large systematic variation with pitch angle similar to that observed with the electrostatic analyzer. When observing pitch angles less than 90° , the flux is approximately isotropic (within a factor of two) and falls off steeply with increasing pitch angle beyond 90° .

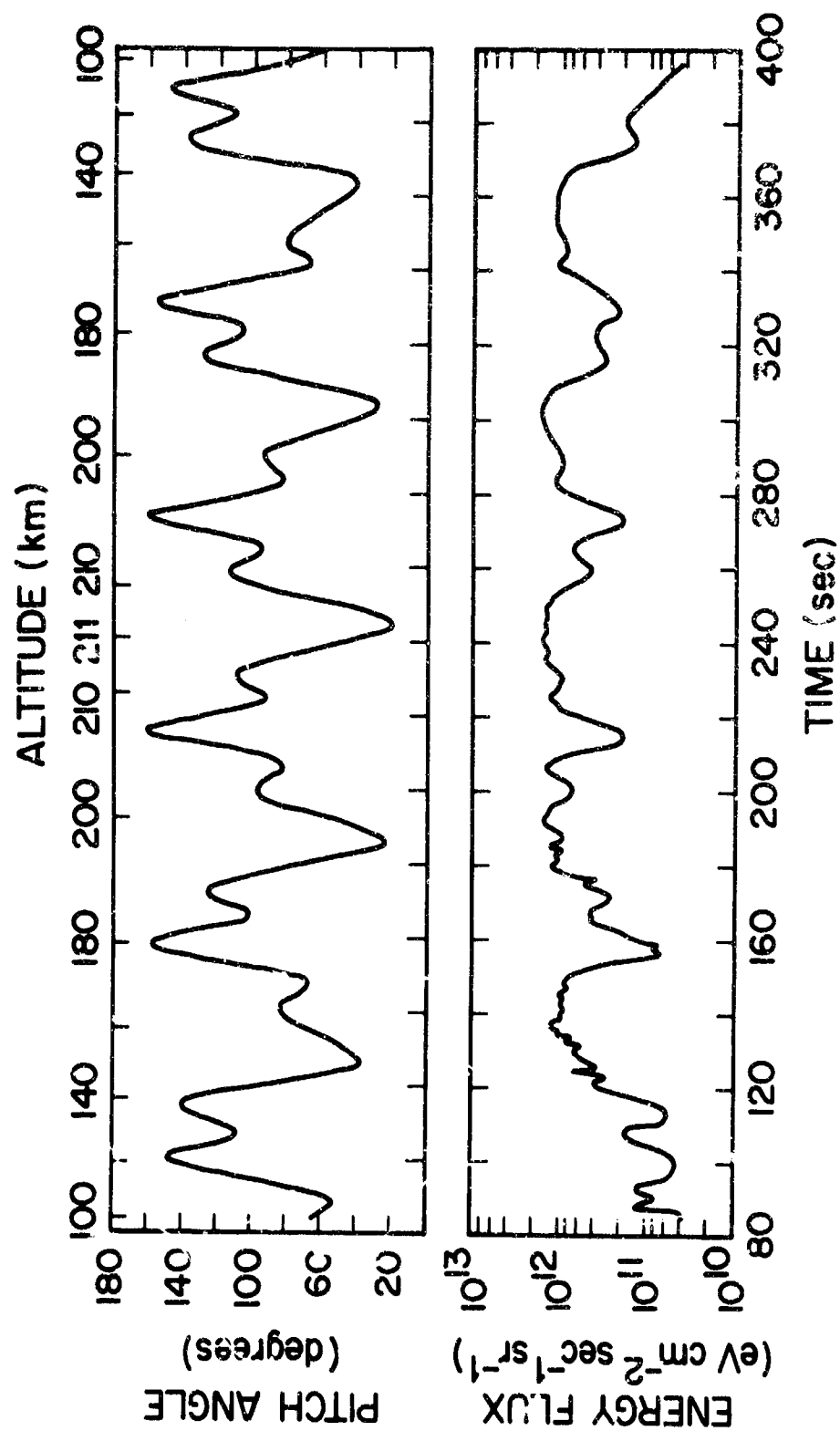
Some fluctuations observed in the earlier part of the flight are not due to pitch angle variations, but rather are temporal or spatial variations in the incident flux. For example, the fluctuation near 110 seconds and the rapid change near 123 seconds were apparently spatially localized.

Figure 3.3 shows the integrated energy flux calculated from the electrostatic analyzer data and corrected for energy loss in the aluminum deposition over the ocintillator. The ionization chamber value is a factor





**PATE OF ENERGY DEPOSITION AND PITCH ANGLE
(ION CHAMBER)**



ENERGY FLUX AND PITCH ANGLE (ELECTROSTATIC ANALYZER)

of three less than the electrostatic analyzer. This discrepancy is within the expected accuracy of the absolute calibration of the two units.

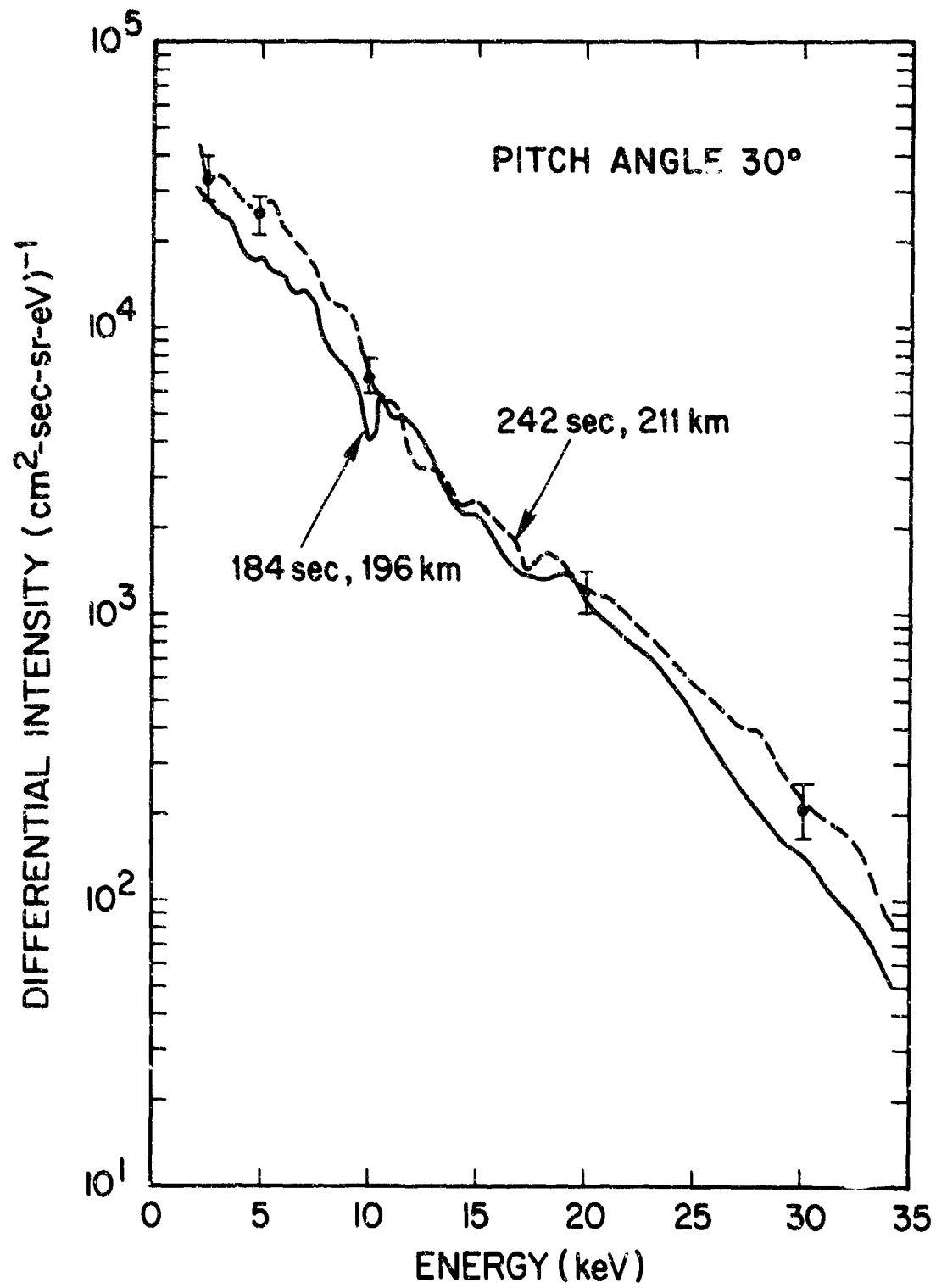
Figure 3.4 exhibits two energy spectra measured at the same pitch angle (near 30°) and 58 seconds apart. The spectra have an approximately exponential form with an e-folding value of 5 keV, which is characteristic of the spectra measured over the entire flight for pitch angles less than 90° . This spectral form differs significantly from the observations of monoenergetic electrons reported by Albert⁷ and Evans⁸.

Two spectra, A and B, measured near apogee for consecutive sweeps at a pitch angle of 64° are shown in Figure 3.5. The instrument noise fluctuations are less than $\pm 20\%$ of the flux and fluctuations such as that near 10 keV are indicative of the rapid variations (spatial or temporal) associated with the aurora.

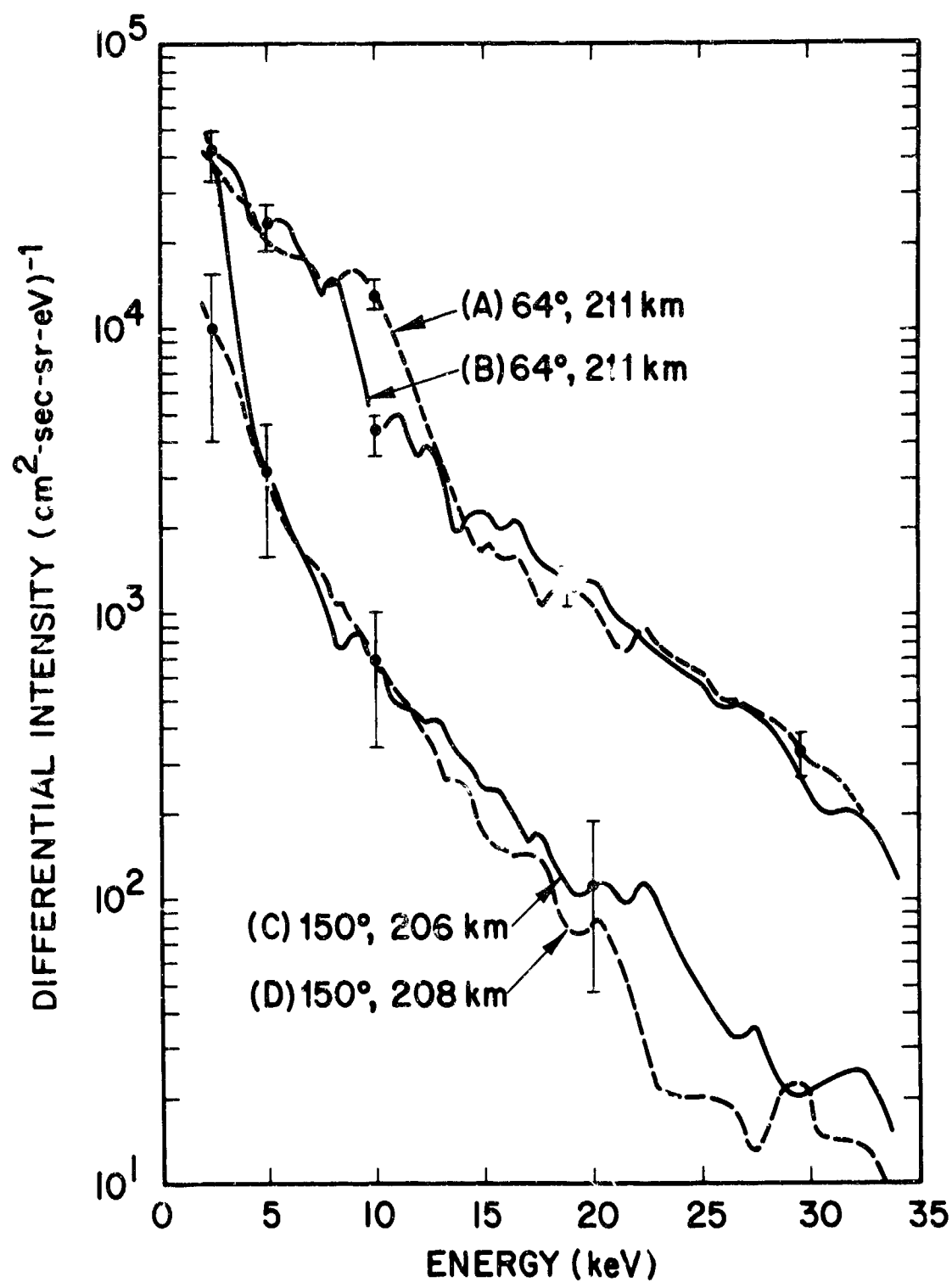
The other spectra, C and D, were measured at a pitch angle of 150° . For energies greater than 8 keV, the spectral shape is similar to the incident spectra but with an intensity lower by about an order of magnitude. Below 4 keV the reflected spectrum at times (curve C) increases steeply to a peak near 2 keV which was nearly the same as the intensity of the incident 2 keV electrons (measured about 20 seconds later). At other times, spectra such as that shown in curve D were observed. An anomalously high reflection of low energy electrons, such as that shown in curve C, has previously been reported by Evans.

Figure 3.6 shows the variation of the energy flux contained in various energy intervals as a function of time. The variation of the spectral form is shown by the top three curves which show the fraction of the total energy flux in various energy intervals. These curves indicate that the spectral form is relatively constant and softens at larger pitch angles. There is a noticeable hardening of the spectrum at 145 seconds and 170 seconds when the incident flux is observed to increase.

ENERGY SPECTRA AT 30° PITCH ANGLE



ENERGY SPECTRA AT 64° AND 150° PITCH ANGLE

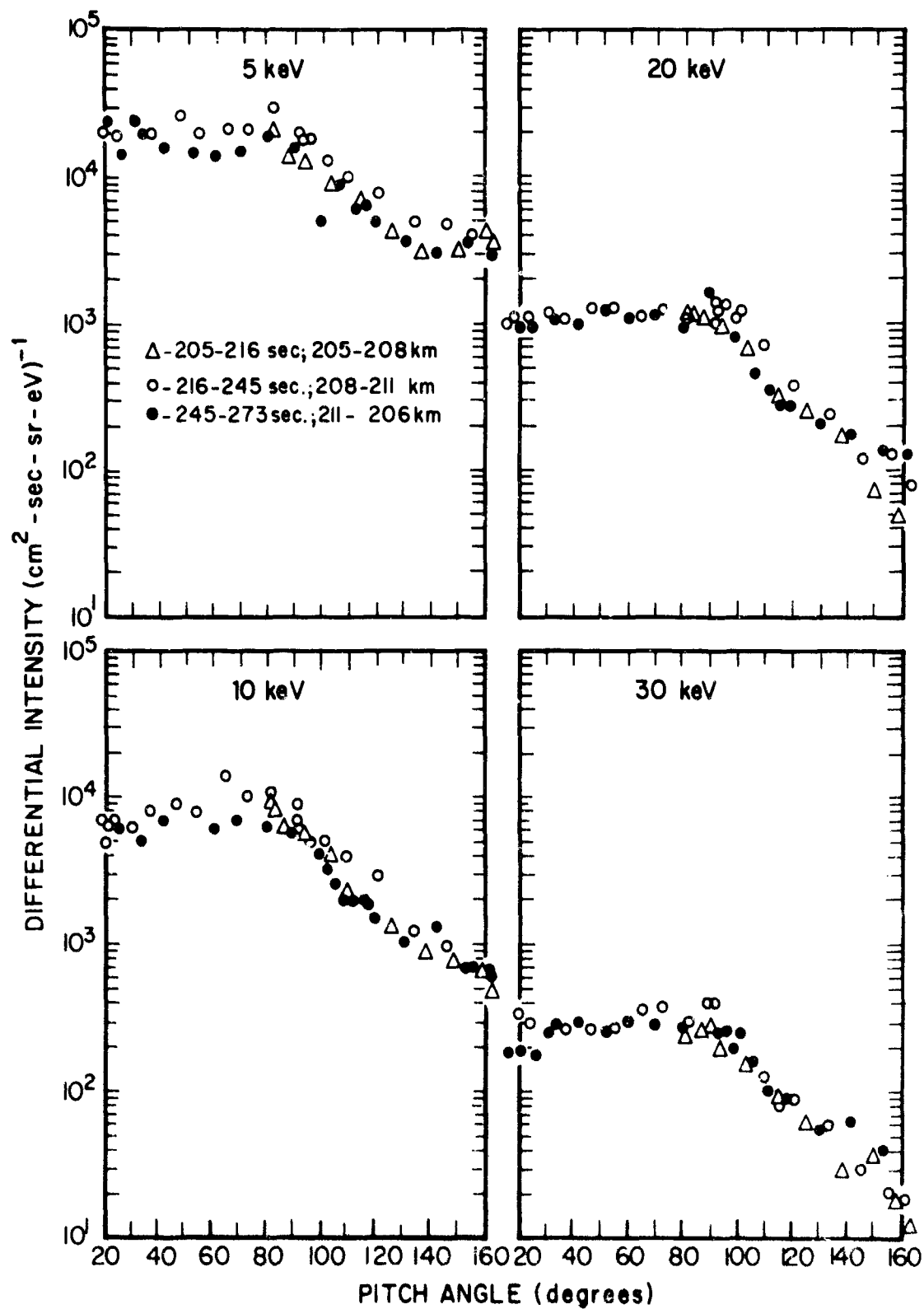


The pitch angle distribution of electrons in the energy range from 2 to 34 keV can be determined from the measured spectra. Previous measurements have been limited to higher electron energies. McDiarmid and Budzinski⁹ and McDiarmid, Budzinski, Whalen and Sckopke¹⁰ have reported a variety of distributions for pitch angles less than 90° and for energies greater than 40 keV which vary from isotropic to distributions strongly peaked near 90° . Mozer and Bruston¹¹ have reported pitch angle distributions for electrons with energies between 65 and 400 keV, which are strongly peaked at 90° . Figure 3.7 shows the pitch angle distribution observed in this experiment for electrons with energies of 5, 10, 20, and 30 KeV. The electron flux is isotropic within a factor of 2 for pitch angles from 20° to 90° . At lower energies the ratio of the incident to "reflected" intensity decreases and at 5 keV the distribution was nearly isotropic from 130° to 160° with an intensity that was only a factor of 5 less than that measured from 20° to 90° .

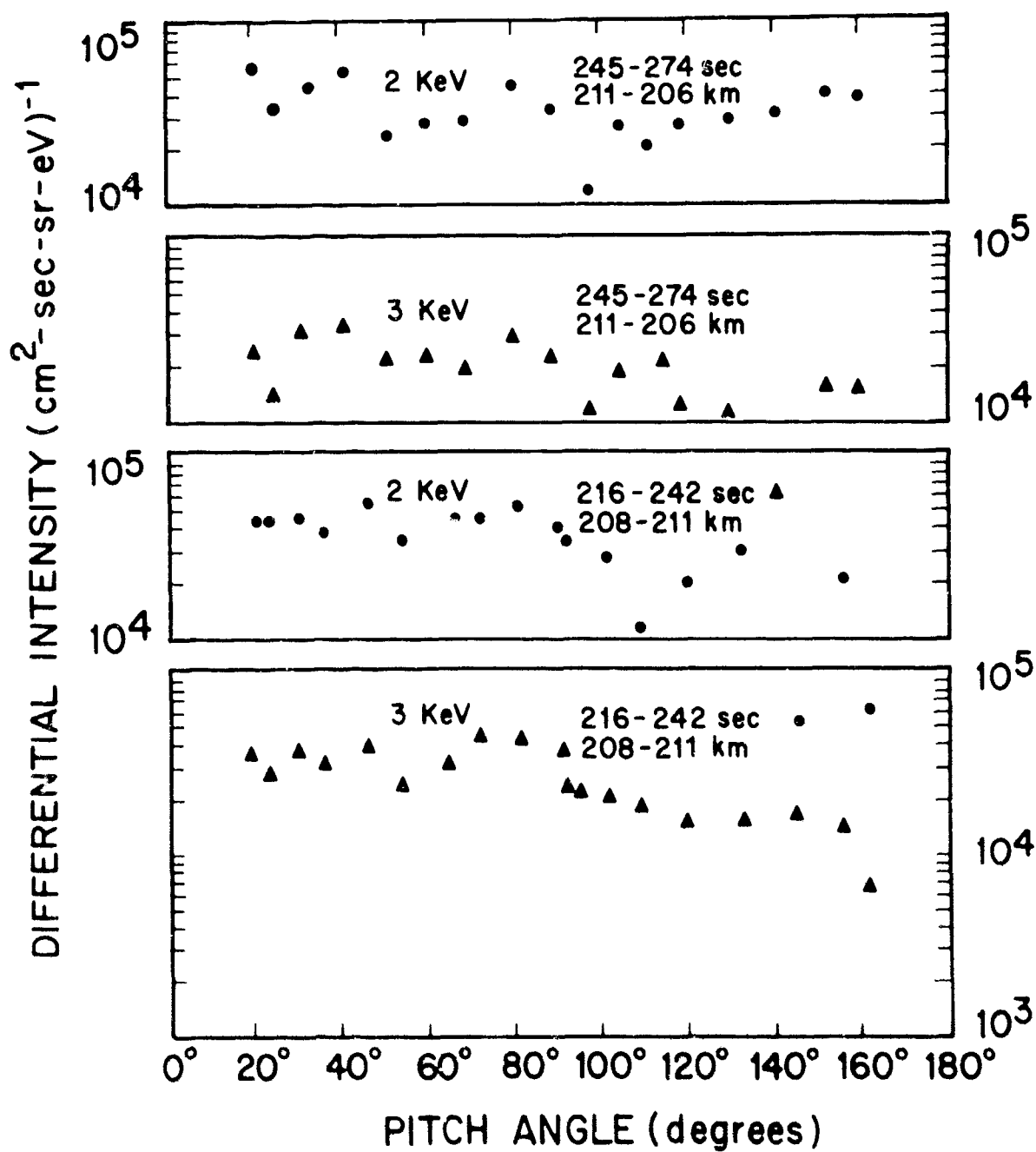
The pitch angle distribution for measured 2 and 3 keV electrons is variable. This can be seen in Figure 3.8, where the data is shown for two succeeding intervals of time.

Figure 3.9 shows the pitch angle distribution measured with the ion chamber. Since the ion chamber has a relatively large field of view. The measured pitch angle distribution is modified by the large field of view ($\sim 120^\circ$ full angle) of the ion chamber and this result cannot be directly compared with the electrostatic analyzer results. Qualitatively the two measurements appear to be in agreement.

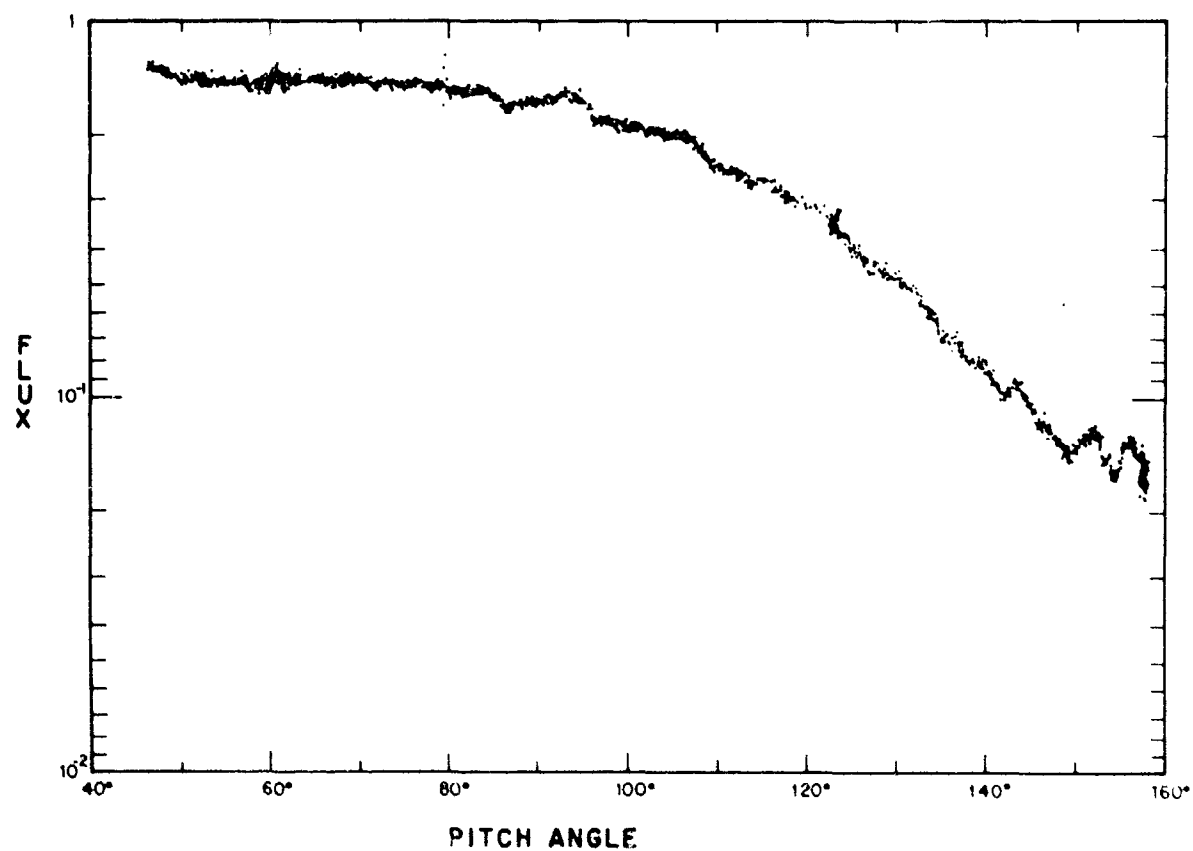
PITCH ANGLE DISTRIBUTION AT 5, 10, 20, AND 30 keV (ESA)



PITCH ANGLE DISTRIBUTION AT 2 AND 3 KeV (ESA)



PITCH ANGLE DISTRIBUTION OF TOTAL ENERGY FLUX (ION CHAMBER)



REFERENCES

1. H. Kanter and E. J. Sternglass. Physics Review 126 (2), (1962), 620.
2. F. R. Paolini, R. Giacconi, J. R. Waters, L. Katz, and D. Smart. Space Research V (North Holland Publishing Co.), 466-488, (1965).
3. K. E. Baker, D. A. Burt, R. H. Haycock, K. G. Seljaas, L. C. Howlett, and G. D. Allred. Rocket Instrumentation for Auroral Measurements, Aerobee 3.615, (Upper Air Research Laboratory: University of Utah), AFCRL-68-0538, UU-68-10, September, 1968.

K. E. Phillips. Characteristics of Auroral Particle Flux, (Upper Air Research Laboratory: University of Utah), UU-69-4, April 1969.
4. A. J. L. Collinson and R. Hill. Proc. Phys. Soc. (London), 1963, pp. 81, 883.
5. D. W. Aitkin, G. L. Beron, G. Yenecay, and H. R. Zulliger. IEEE Trans. Nuclear Science, (1967), NS-14, 468.
6. R. Gwin and R. B. Murray. Physics Review 131, (1963), 501.
J. Menefee, C. F. Swinehart, and E. W. O'Dell. IEEE Trans. Nuclear Science, NS-13, (1966), 720.
7. R. D. Albert. Physics Review Letters, 18, (1967), 369.
8. D. S. Evans. "An Auroral Electron," Paper presented at the Birkeland Symposium on Aurora and Magnetic Storms, Sandefjord, Norway, 1967.
9. I. B. McDarmid and E. E. Budzinski. Can. J. Physics, 42, (1964), 2048.
10. I. B. McDarmid, E. E. Budzinski, G. A. Whalen, and N. Sekopke. Can. J. Physics, 45, (1967), 1755.
11. F. S. Mozer and P. Bruston. J. Geophysics Research, 71, (1966), 4451.

APPENDIX A

Satellite Measurements of Low Energy Electrons
in the Auroral Regions

by

E. R. Hegblom and W. P. Reidy
American Science and Engineering, Inc.

J. A. Sandock
Air Force Cambridge Research Laboratories

Text of paper presented at the 49th Annual Meeting of the
American Geophysical Union, Washington, D. C., April 1968

The research reported in this paper was sponsored by, but does not necessarily
constitute the opinion of the Air Force Cambridge Research Laboratories, Office
of Aerospace Research under Contract F19628-68-C-0287.

ABSTRACT

Measurements of the differential energy spectra of low-energy electrons have been made with two electrostatic analyzers flown on the OAR-OV3-2 satellite. The satellite was launched October 28, 1966, into a polar orbit with an inclination of 82° and an apogee and perigee of 1600 and 330 km, respectively. The electrostatic analyzers were designed to measure electrons in the energy range from 8 to 100 keV in a period of 10 seconds with an energy resolution of 8%. A variety of electron spectra were measured near the auroral regions, and spatial and temporal variations of the spectra are discussed. The regions where intense fluxes were observed and correlations with magnetic activity are enumerated.

This paper presents the preliminary results of the measurement of the differential energy flux of electrons by means of electrostatic analyzers in the energy range from 10 to 70 KeV made from the OV3-2 satellite.

The OV3-2 satellite was launched into a polar orbit with an inclination of 82° on October 28, 1966. The satellite has a perigee of 330 km and an apogee of 1600 km. An on board tape recorder enabled data to be accumulated for 2 1/2 hours. The results presented here were obtained in the period from November 1 to December 15, 1966. The satellite spun at a rate of about 4 RPM and the pitch angle distribution was obtained with the aid of a three-axis magnetometer.

The satellite had two electrostatic analyzers arranged so that their fields of view were 180° apart and at 90° to the spin axis of the satellite. The purpose of this arrangement was to measure the fore and aft asymmetry in the pitch angle distribution of electrons and to measure the flux of precipitated and reflected electrons.

The electrostatic analyzer utilized spherical quadrants to achieve energy selection. The electrons were detected by an aluminum coated Pilot B scintillator coupled to a photomultiplier. The coating reduced the sensitivity of the instrument to light, and it imposed a low energy cut-off of about 8 KeV on the measurement. A logarithmic amplifier measured the photomultiplier current.

The responses of the instruments to sunlight and to high energy penetrating particles in the inner radiation belt enable a rough in-flight check to be made of their relative sensitivity.

The instruments had an energy resolution of about 8% and plate voltage was swept with a period of ten seconds.

The power supplies were synchronized so that the sweeps of both would start at the same time, but the energy measured by each as a function of time is slightly different. The power supplies were designed so that electrons could be measured up to 100 KeV but a malfunction generally limited the range to about 70 KeV.

The viewing aperture of the instruments was about 8° by 20° , and they had a geometric factor of about $.05 \text{ cm}^2\text{-ster.}$

Figure 1 shows the minimum detectable signal as a function of energy that could be observed with these analyzers, and this limit is imposed by the observed noise, including telemetry and photo-multiplier dark current noise.

Both trapped and precipitated electrons were measured, and for this preliminary analysis, about six orbits with the most intense fluxes out of about 24 available with tape recorder data were chosen for examination. It was observed that these orbits generally occurred on geomagnetically disturbed days and the three hour index K_p was above 2^+ .

Figure 2 shows a polar plot of the location of the region where electrons were detected on these selected orbits as a function of invariant latitude and local time. It is preferable to use geomagnetic

local time and this will eventually be done. The lines on the plot illustrate the portion of the orbit for which data were accumulated.

With this small sample of data, no attempt has been made yet to determine the latitudinal variation with K_p . It can be seen that data is generally accumulated near the auroral regions between 60° and 75° invariant latitude and that the data are accumulated at higher latitudes on the day side than on the night side. This is consistent with the observations reported that the boundary of the trapping region and the auroral oval are at higher latitudes on the day side than on the night side.

Figure 3 attempts to show in a somewhat rough way the correlation observed with K_p . Values of K_p where no bar is shown means that no orbit with that value of K_p was observed rather than that no data was observed.

The number of sweeps per orbit which gives a rough indication of the total electron flux occurring above the threshold of the instrument at these times is plotted.

There is a correlation observed as would be expected from the results reported by other observers who have measured precipitated and trapped fluxes in the auroral regions and the outer belt.

A variety of differential energy spectra were observed during the orbits. If the spectra are approximately by an exponential form the e-folding values in the 10-60 KeV energy range vary from 8 to 30 KeV. The satellite spin period was 15 seconds while the energy sweep period is 10 seconds, and a large range of pitch angles is sampled in one sweep period. This complicates the data analysis because it is not easy to separate the variations in the energy and pitch angle distributions.

In addition, the satellite was moving at 7km/sec and possible spatial and temporal variations may also occur during one sweep period. Another complication is that the instruments are sensitive to sunlight and the data must be corrected for this during sunlit orbits.

The next figure (Figure 4) shows an example of particle precipitation observed at 0200 Local Time $K_p = 3$, L value of 6.5 and altitude of 465 km. Generally particle precipitation is measured on these orbits and at times, the measured incident spectra is the same for a few sweeps. This slide shows the spectra measured on two successive sweeps and the upper curve on each graph represents the incident flux. It is relatively constant with an approximate e-folding value of 9 KeV. The pitch angles for each ESA are plotted along the top and bottom of the graph. It can be seen that the reflected spectra are about 10% of the incident flux in agreement with the expected value of 10 to 20%. There is relatively little variation in pitch angle when measuring the incident flux from 10 to 40 KeV, and the spectrum has not changed much from one sweep to the next so that this should be a reasonable measurement of the electron spectrum. At pitch angles near 90° , the incident and reflected spectra are approximately equal. The precipitated energy is about $4 \text{ ergs/cm}^{-2} \text{ sec}^{-1} \text{ ster}^{-1}$.

In the next figure (Figure 5) the interpretation of the data is not as simple because of the large variation in pitch angle that is observed. These spectra were measured during another orbit on the night side of the earth at about 500 km, $K_p = 4$. The shape of the incident spectrum on the left is similar to that of the previous slide with an e-folding value of 9 KeV, but the spectrum on the right measured 40 seconds later is considerably softer with an e-folding value of about 4 KeV. However, this would be observed if the energy distribution was harder with a pitch angle distribution that was peaked around 0° .

These spectra may be compared with previously measured spectra observed during aurora. These spectra have the same intensity at 10 KeV as some previously reported measurement for types I - II aurora and have e-folding values which are close to that measured for aurora.

An example of apparently trapped electrons is shown in Figure 6.

From about 10 to 40 KeV the measured fluxes are nearly equal but above 40 KeV they diverge sharply. The flux is very intense and the e-folding value is about 13 KeV and is somewhat harder than that observed for precipitated particles.

MINIMUM DETECTABLE DIFFERENTIAL INTENSITY (OV3-2)

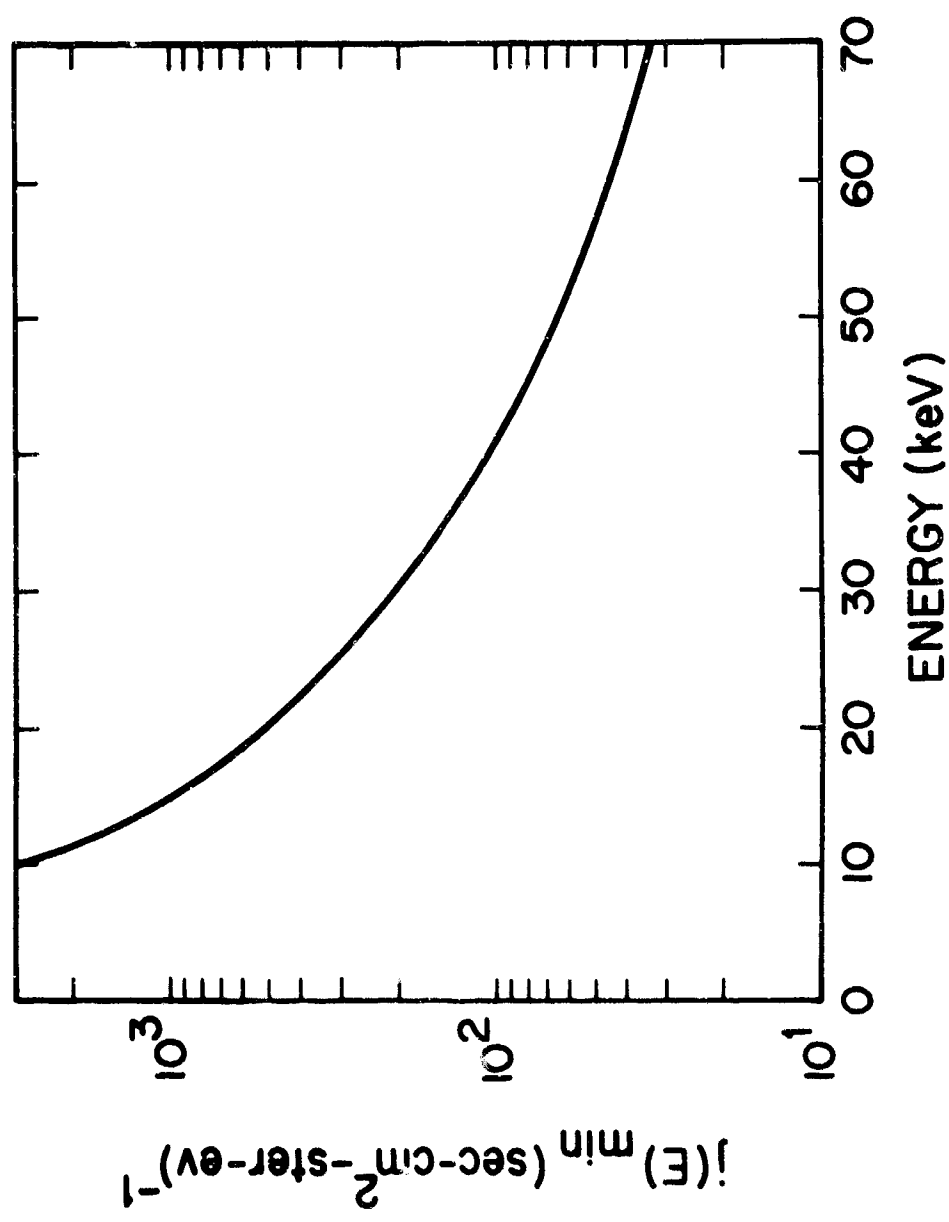


Figure 1

POLAR PLOT FOR DETECTION OF ELECTRON (10-100keV)
AS A FUNCTION OF
INVARIANT LATITUDE AND LOCAL TIME

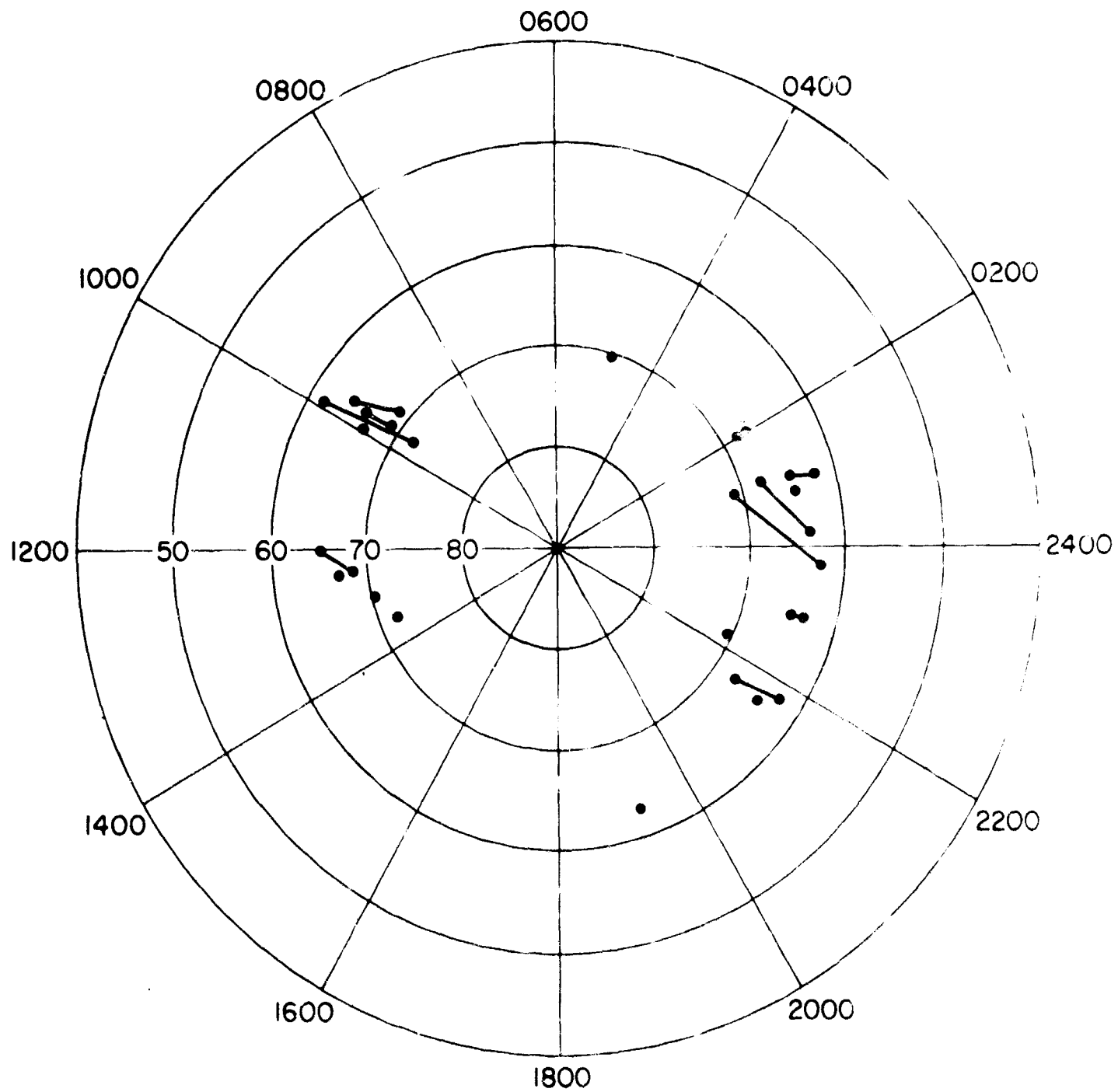


Figure 2

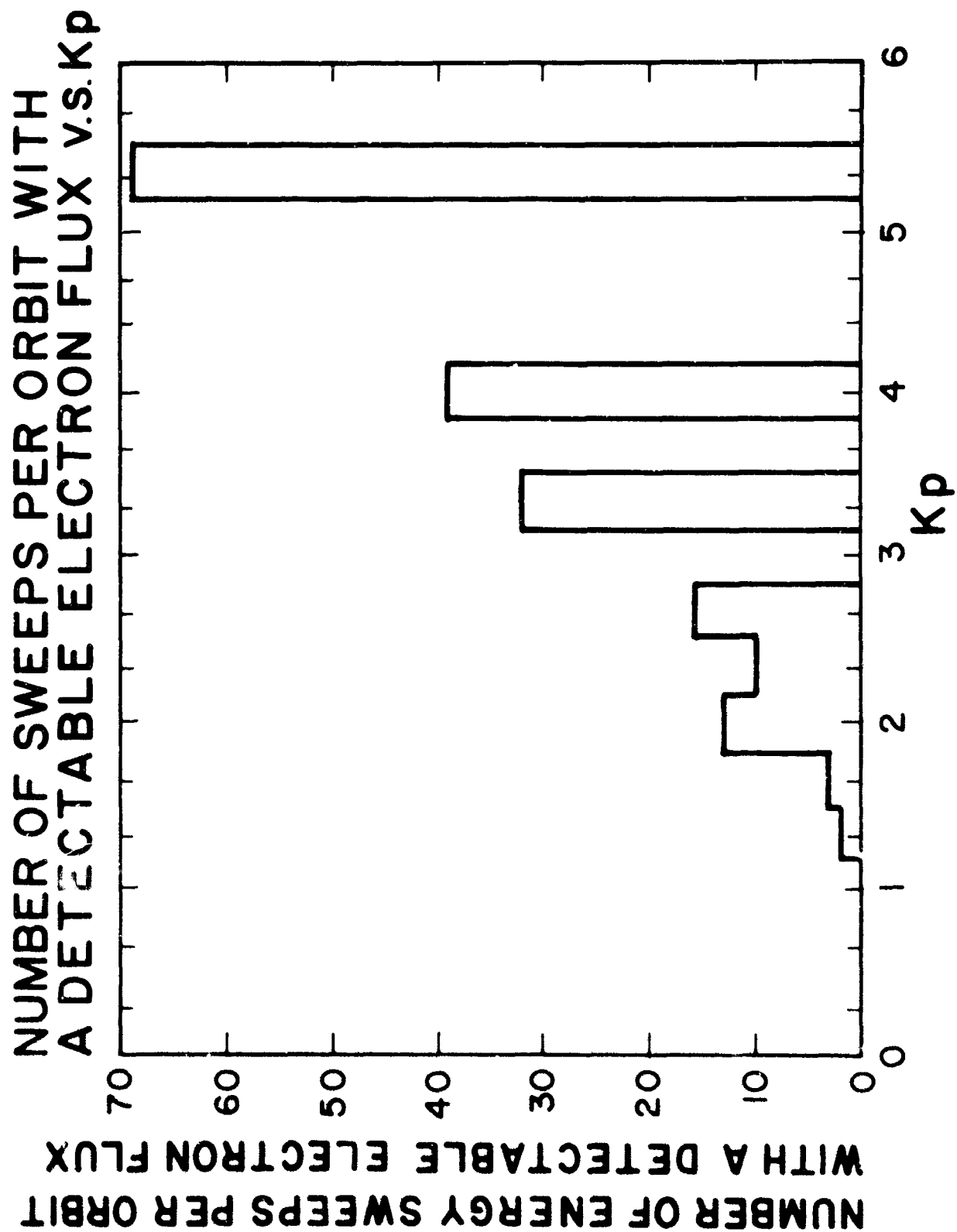


Figure 3

DIFFERENTIAL ENERGY SPECTRA (OV3-2)

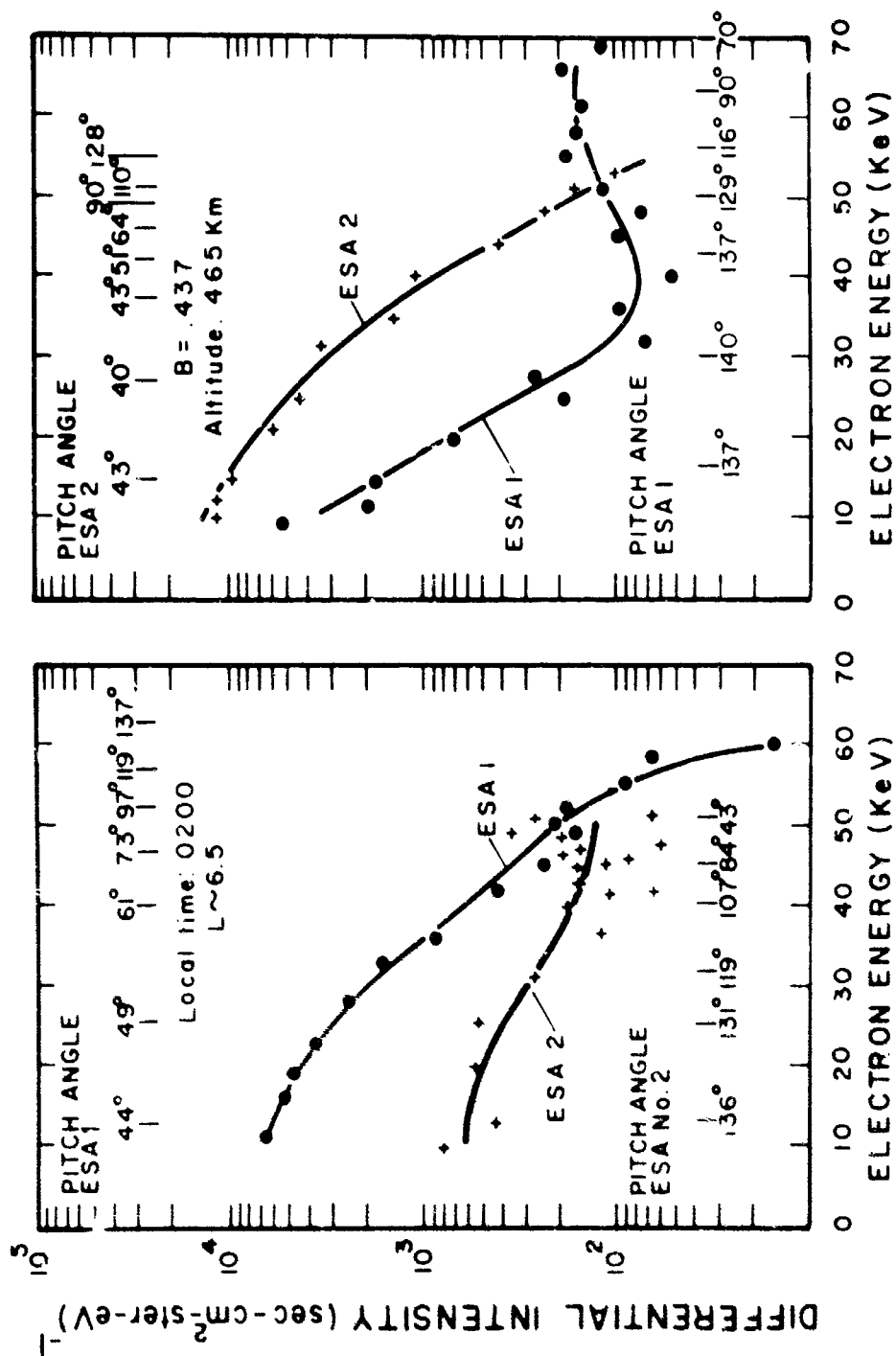
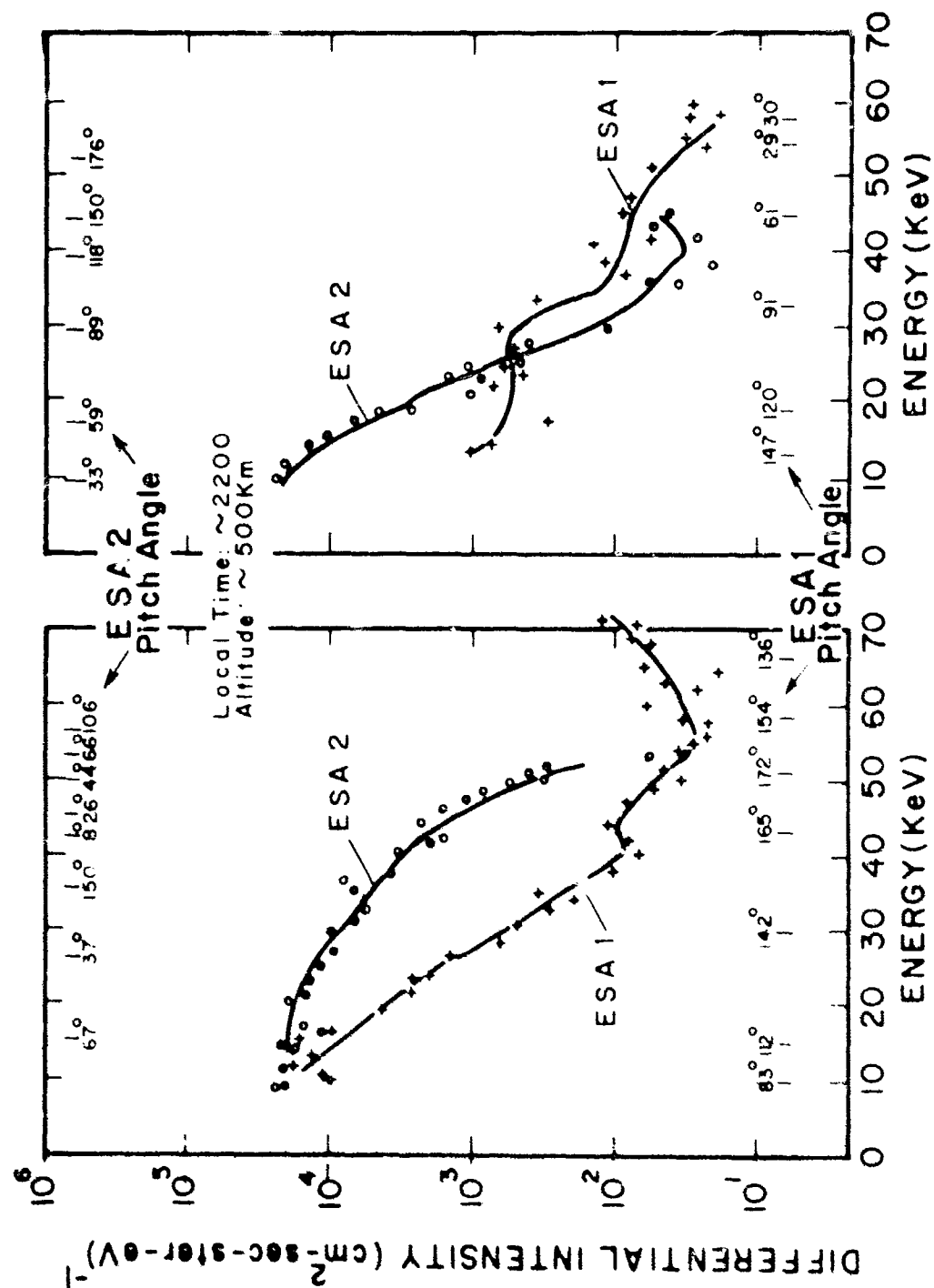


Figure 4

DIFFERENTIAL ENERGY SPECTRA



DIFFERENTIAL ENERGY SPECTRA (OV 3-2)

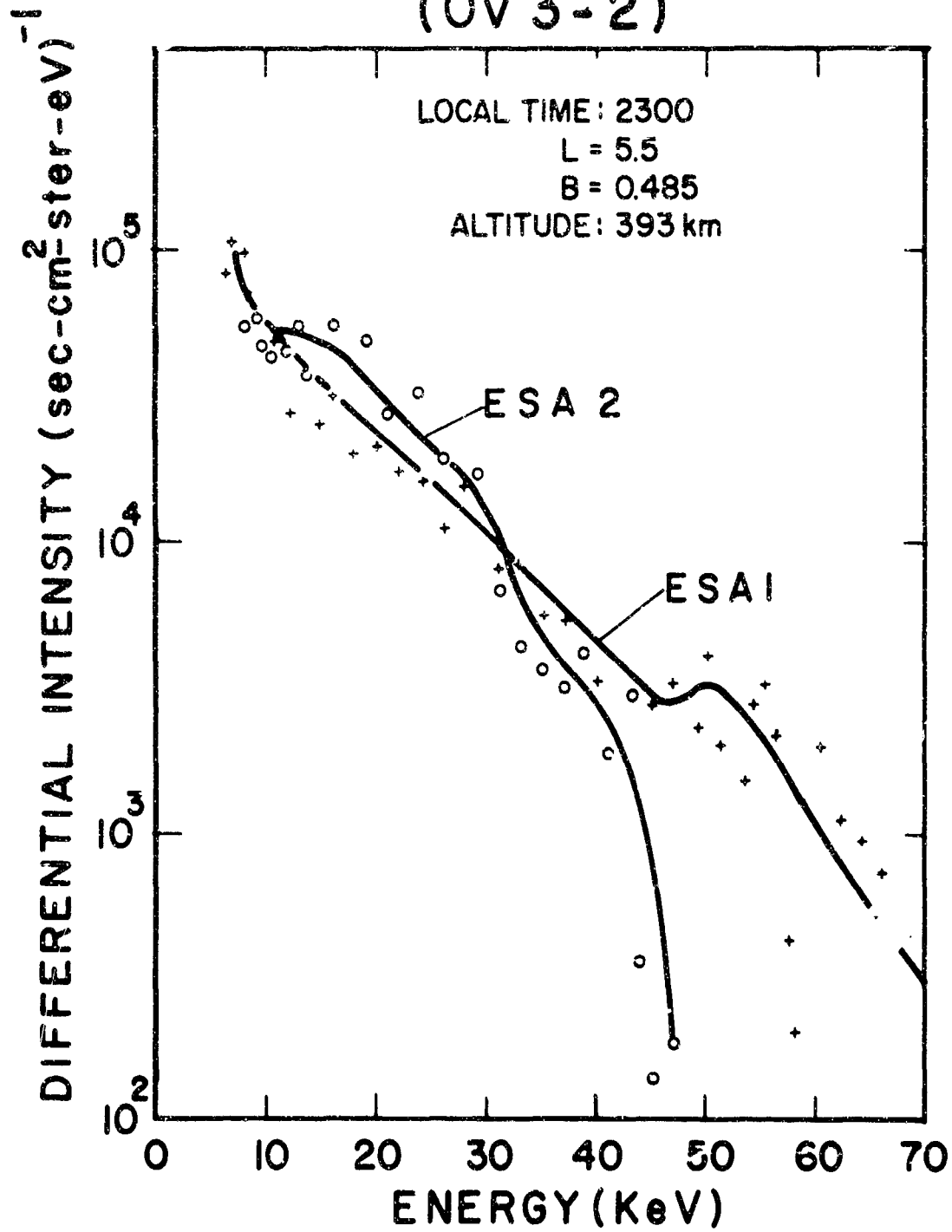


Figure 6

APPENDIX B

Correlated Satellite and Ground Based Measurements
from the OV3-2 Satellite and Churchill Research Range

by

J. A. Sandock
Air Force Cambridge Research Laboratories

and

E. R. Hegblom
Boston College

Text of paper presented at the 7th National Fall Meeting of the
American Geophysical Union, San Francisco, California,
December 1968.

Two electrostatic analyzers were included as part of the payload of the OV3-2 Satellite. This polar orbiting Satellite had the following orbital parameters an inclination (I) of 82° and an apogee/perigee of 1600/330 km. After two years in orbit the apogee/perigee has been reduced to 1200/310 km.

A satellite command transmitter was installed at Churchill Research Range to conduct investigations of the precipitated and trapped electrons which are associated with local magnetic disturbances and the auroral phenomena (Figure 1). This figure shows the field of view of the two electrostatic analyzers mounted 180° apart and normal to the spacecraft axis. Each sensor has an $8^{\circ} \times 20^{\circ}$ field of view and its geometric factor is $.05 \text{ cm}^2 \text{ ster.}$ The minimum detectable differential intensity is $3 \times 10^2 \text{ electron/sec-cm}^2 \text{ ster-ev.}$ At 25 KeV and $1.1 \times 10^2 \text{ electron/sec-cm}^2 \text{ ster-ev.}$ No differential flux has been observed beyond 70 KeV (Figure 2).

On December 4, 1967, Churchill Research Range commanded the OV3-2 Satellite on and off for the first time. Since that time approximately 100 passes have been recorded and sent to AFCRL for analysis. Figure 2 shows a histogram of passes taken from 2130 to 0200 hours local time at Churchill. The passes are broken down into intervals of 1/2 hour. This slide represents 60 passes of which 10 displayed enough energetic particle flux to be analyzed. The occurrence of measured particle flux are plotted versus invariant latitude and local time with the associated 3 hr. Kp index noted beside each pass. The invariant latitude of CRR is shown by the broken line. In general energetic electron flux is only observed when a Kp 2^{+} is in effect. However, there are passes when high Kp of 4, during which no

observable flux from the detectors. The position of the observed flux during magnetic disturbed conditions is shown to be south of CRP prior to local midnight and shifts northward after local midnight which is consistent with the concept of the auroral oval as stated by Akasofu. (Figure 2).

Figure 3 shows the recorded telemetry output from the amplifiers of the two ESA for one of the passes (5817) shown in the preceding figure. A period of 10 seconds is required for the electrostatic analyzer to sweep the energy range between 25 and 100 keV. The pitch angle is determined by using the magnetometer data shown in the figure. An appreciable electron flux was observed during this pass.

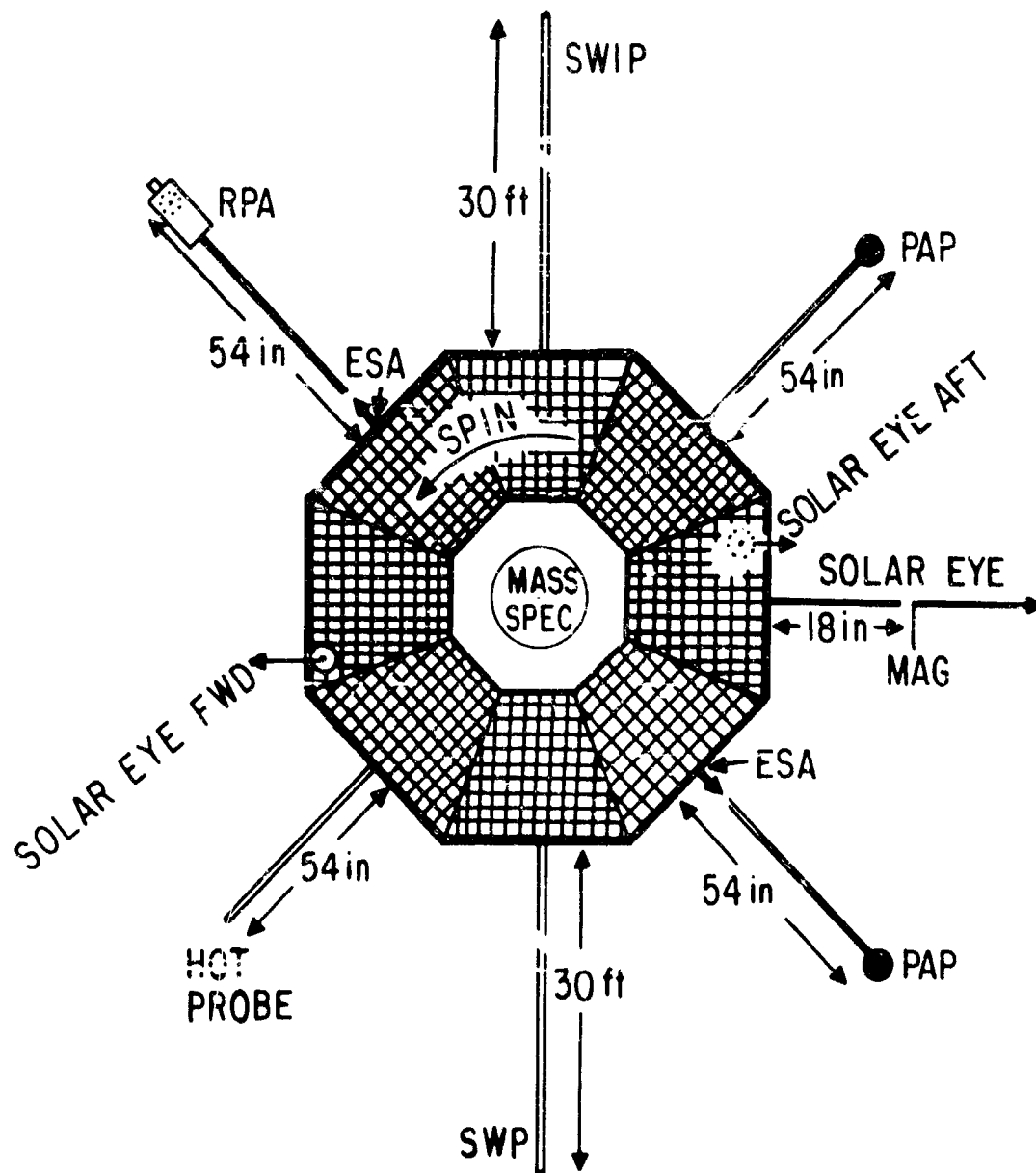
The next Figure (4) shows the output of the X, Y, Z ground-based magnetometers and the 30 MHz polar riometer at Churchill Research Range. On pass 5816, no electron spectra was observed from the satellite. However on pass 5817, 104 minutes later the spectra discussed above was observed. This later pass was much closer to the ground-based measurements than the previous pass. The riometer was showing absorption of 1 db and the pass took place shortly after an auroral substorm which is normally associated with the auroral breakup. It could be argued that the energetic electrons associated with the auroral absorption observed at Churchill Research Range are those observed by the satellite at 600 km.

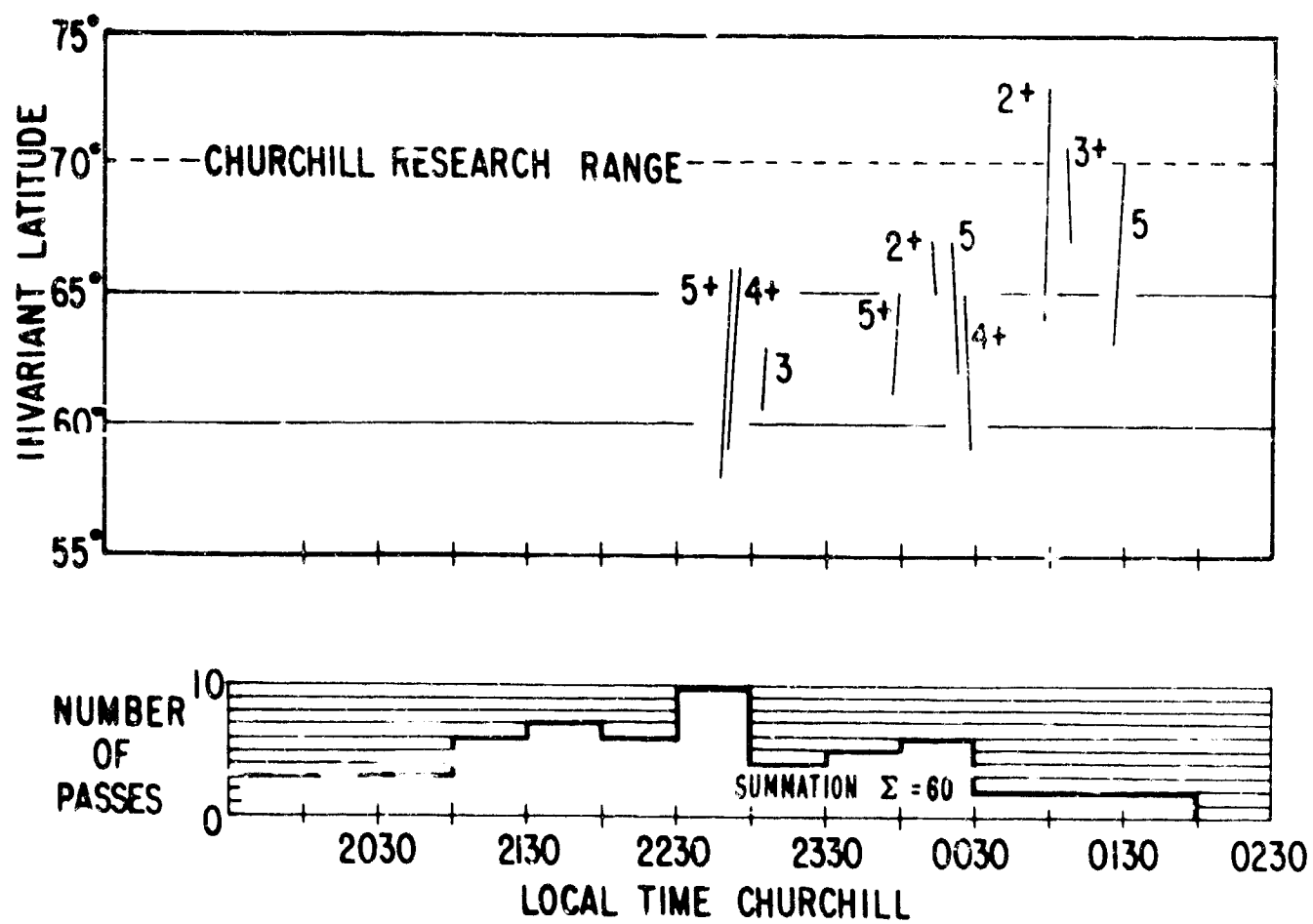
Figure 5 shows the differential intensity (electrons/sec-cm²ster-ev) versus energy and pitch angle measured during this event (pass 5817). It should be noted that the pitch angle varies according to the spin of the satellite and is shown at the top of the slide. Spectrum C has the proper pitch angles to look at precipitating particles. If one assumes that the distribution is isotropic between pitch angles of 60° and 40°, the data can be fitted to an exponential distribution with an e-folding value of 5.5 keV. The integral particle flux for electrons with energies greater

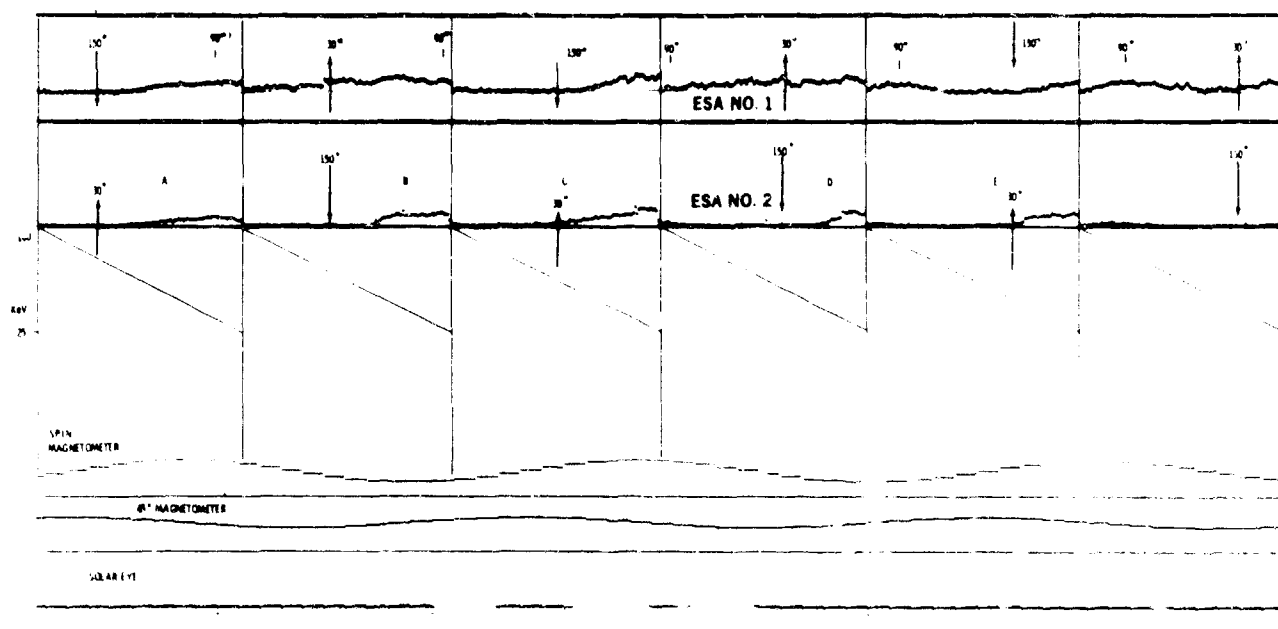
than 25 KeV is 5×10^7 particles $\text{cm}^{-2} \text{sec}^{-1} \text{ster}^{-1}$. Extrapolating between 0 and 25 KeV the resulting energy corresponds to a flux of $15 \text{ ergs cm}^2 \text{sec}^{-1}$. This energy corresponds to the energy associated with a class II aurora.

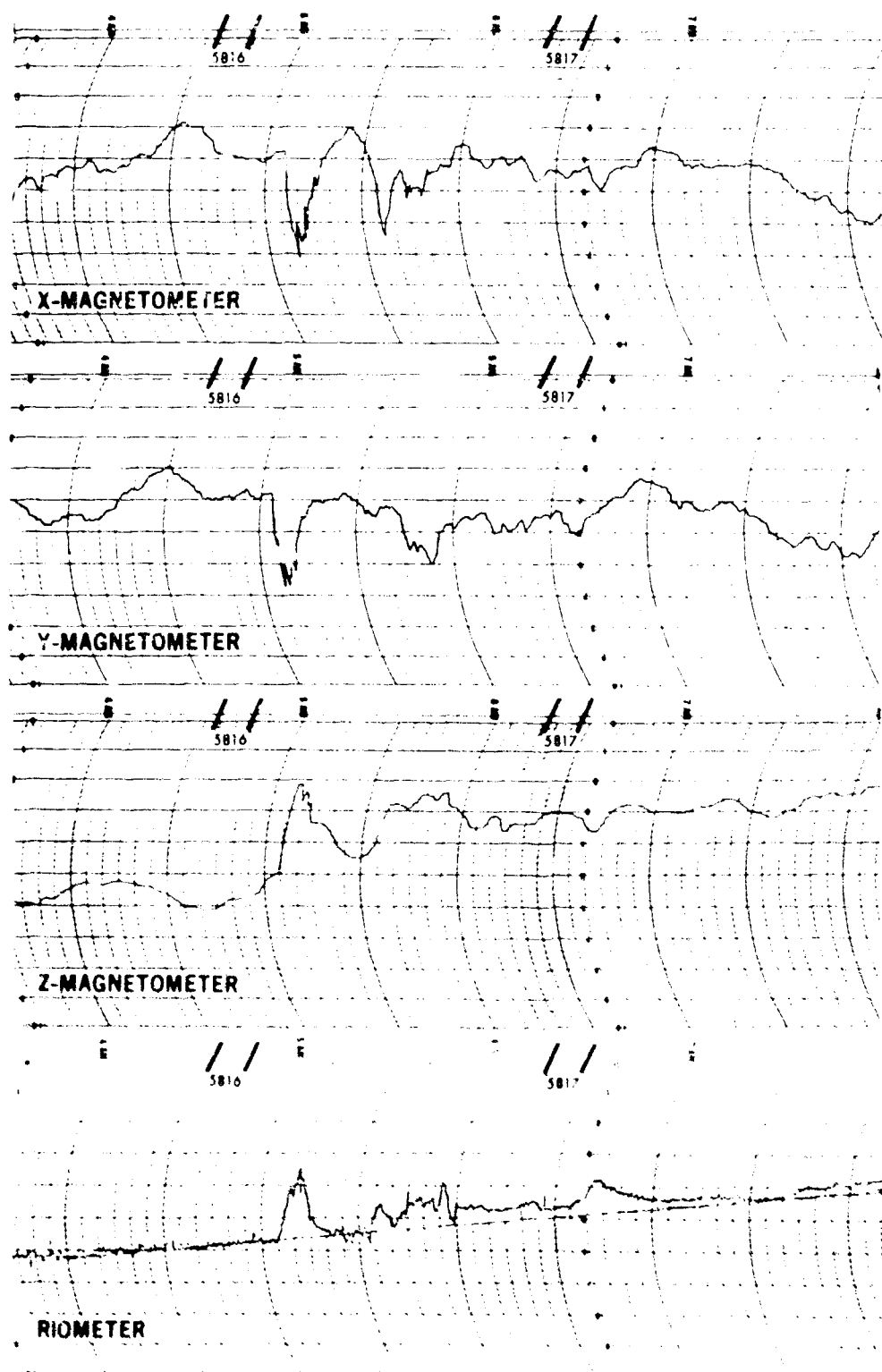
In conclusion we intend to continue to correlate all sky camera data with observed spectra from this satellite. Also we intend to obtain more magnetometer data at stations near Churchill in order to determine local magnetic activity during satellite passes and the location of the auroral electrojet with respect to the observed spectra.

OV3-2 SATELLITE PLAN VIEW

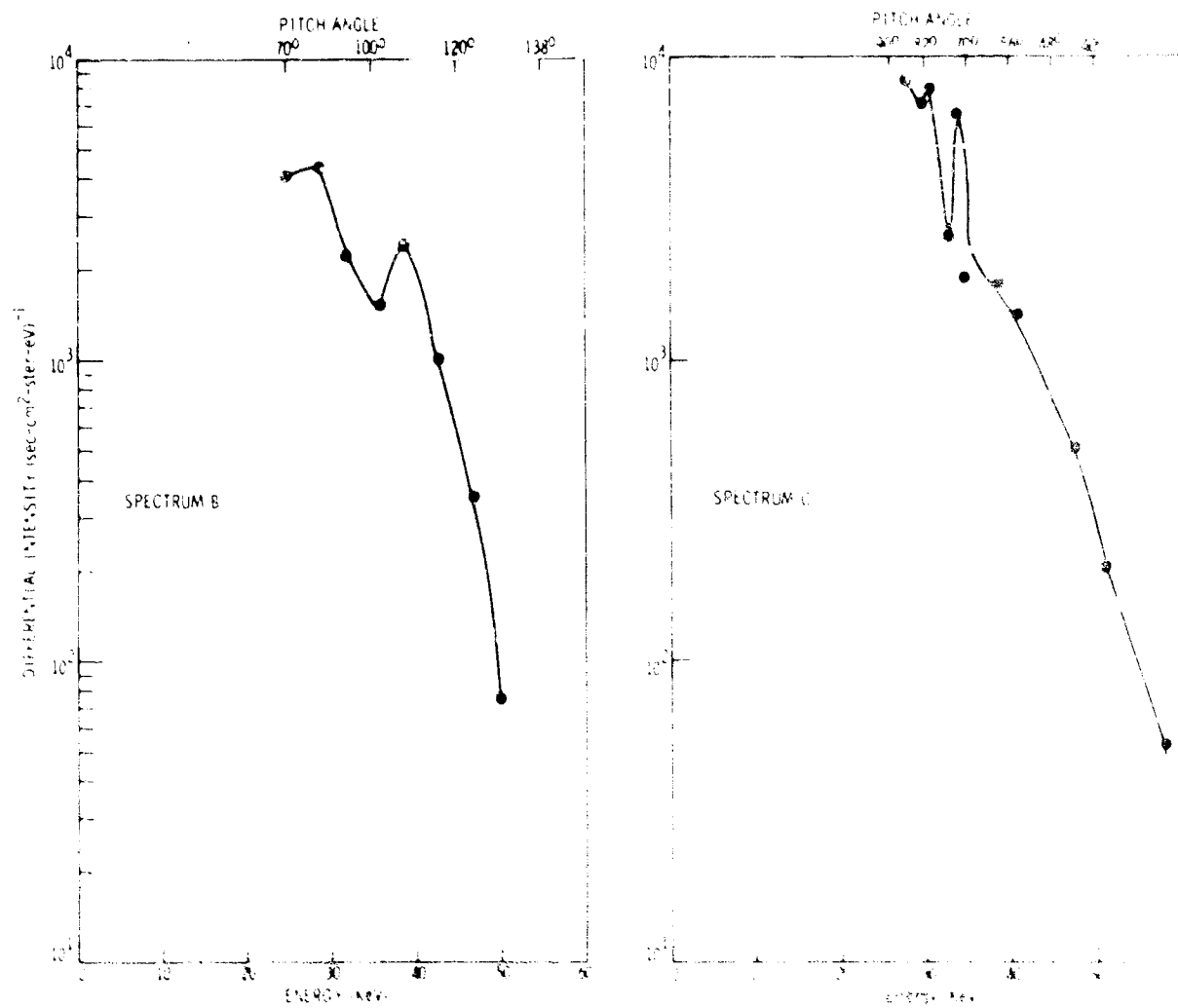








DIFFERENTIAL ENERGY SPECTRA (OV3-2)



APPENDIX C

Coordinated Measurements from Two Multi-Experiment
Rockets in an Aurora

by

J. C. Ulwick

Air Force Cambridge Research Laboratories (OAR)
L. G. Hanscom Field, Bedford, Massachusetts

K. D. Baker

University of Utah, Salt Lake City, Utah

and

E. R. Hegblom

American Science and Engineering, Cambridge, Massachusetts

Reprint from Space Science IX, North Holland Publishing Company,
Amsterdam (1969).

ABSTRACT

Measurements have been made recently of several related auroral parameters on two rockets flown within 30 seconds at Churchill, Canada. Each rocket carried a comprehensive payload for the measurement of electron and ion density and temperature, primary and secondary electron flux and spectra, portion flux, X-rays, and N_2^+ and OI light emissions. The rockets penetrated a dim, diffuse aurora (several Kilorayleighs of 5577 Å emission) during the break-up phase. The incident electron energy flux did not change appreciably over most of the flight for pitch angles less than 90° and the spectra had an approximately exponential form with an e-folding value between 5 and 7 KeV. The pitch angle distribution was approximately isotropic over the upper hemisphere with a drop off for higher pitch angles that is more pronounced at higher energies. Short time variations in the flux in general were not correlated at the two rocket positions. One, associated with a rapidly developing arc near one of the rockets, is observed to produce only effects characterized by an increase in flux especially at lower energies. It is shown, however, that a short time increase in flux can also occur over an extended area accompanied by corresponding increases in hyperthermal electrons and electron temperatures.

INTRODUCTION

A problem in rocket probing of an aurora is the difficulty in separating spatial and temporal variations of the phenomena involved, since the rocket moves rather rapidly through the region of interest. In the case of a rapidly changing aurora, as in the break-up phase of an auroral arc, this becomes more important than in the stable or quasi-equilibrium conditions. To study this problem, two rockets carrying the auroral "Input-Output" experiment (where the input, the energy flux of primary particles and the output, the atmospheric ionization, heating and light emission, are measured by probes) were launched at Churchill, Canada approximately 30 seconds apart during the break-up phase of an aurora. Although both rockets contained probes for measuring charge density, temperature, composition, and luminosity, the emphasis in this paper is given to measurements of auroral electron total energy, energy spectrum, and angular distribution from a few KeV to 100 KeV.

GROUND OBSERVATIONS

Photometer, magnetometer, and all-sky camera data were provided by the Churchill Research Range. The 5577 Å line measured at the predicted position of the rocket at 100 km showed an increase of about a factor of four over the duration of the flight from 1.5 to 6.5 KR. At launch there was a decrease in the horizontal component of the earth's magnetic field of about 300 γ , and no appreciable change during the flight. According to all-sky camera data the rockets penetrated the diffused background associated with an auroral arc and not the region of maximum intensity.

ROCKET PERFORMANCE

The two rockets were an Aerobee (3.615) and an Astrobee 200 (15.735). Both rockets were fired with almost the same azimuth (115°) with the Astrobee 200 launched 30 seconds after the Aerobee. The Astrobee's apogee was 211 km compared to the Aerobee's 180 km. More important, however, is the fact that the Astrobee impacted almost 250 km downrange compared to 125 km for the Aerobee. Thus, on rocket ascent from 100 to 160 km the two rockets penetrated the same region of the sky, but at apogee and on rocket descent the two rockets were more than 70 km apart. The Aerobee rocket had a small precessional cone which allowed the side-looking detectors to scan pitch angles $90^{\circ} \pm 5^{\circ}$ to $90^{\circ} \pm 12^{\circ}$. The ejected nose tip, however, tumbled giving 0 to 180° pitch angles. The Astrobee 200, rather fortuitously, tumbled throughout the flight which allowed the instruments to scan pitch angles from 20 to 160° .

ASTROBEE 200 RESULTS

The rate of energy deposition of auroral particles was measured by an ion chamber and by an electrostatic analyzer (ESA). The ionization chamber filled with 90% nitrogen and 10% methane at a total pressure of 10 cm Hg, had a formvar window 1600 Å thick, (equal to the range of 1.6 KeV electrons), with an area of 0.5 cm^2 . The field of view was conical with a 6° half angle and its center made an angle of 60° with the rocket axis and was located on the opposite side of the rocket from the electrostatic analyzer. In-flight calibration of the ion chamber was achieved by measuring the output current due to a two-microcurie Radium 226 source mounted in front of the entrance aperture on a door that was opened at 60 km.

Figure 1 shows the measured rate of energy deposition (corrected for the energy loss in the window) and the angle between the center of the field of view and the magnetic field as a function of time. The incident energy flux measured by the ion chamber is obviously correlated with the pitch angles. Especially from 180 to 360 seconds the energy flux is rather stable and approximately isotropic (within a factor of two) for pitch angles less than 90° , but falls off steeply (to over an order of magnitude) with increasing pitch angle beyond 90° .

The electrostatic analyzer flown on this rocket and the results, including the spectra and pitch angle distribution in the energy range 2 to 34 KeV, have been described (1), (2). The rate of energy deposition calculated from the measured electron spectra (approximately exponential with an e-folding value between 5 and 7 KeV) was about a factor of three greater than that measured by the ion chamber, but within the expected accuracy of the absolute calibration of the instruments (about a factor of two for each instrument). Although the instruments were mounted on opposite sides of the rocket and, therefore, looking nearly 180° out of phase, the results with respect to pitch angle distribution compare quite favorably in the time interval 180 to 360 seconds indicating how stable conditions were. Only in the early part of the flight are some significant fluctuations observed that are not due to pitch angle variations. Adding the information obtained from the Aerobee rocket these variations are identified as spacial in nature.

A more complete determination of the electron pitch angle distribution for energies 2, 5, 10, and 20 KeV is shown in Figure 2 for the data of the ESA between 170 and 310 seconds. The pitch angle distribution is isotropic within a factor of two for pitch angles less than 90° with a drop-off for higher pitch angles which was more pronounced at higher energies.

AEROBEE RESULTS

Two energy deposition scintillators were flown on board the Aerobee rocket. The instruments basically consist of a scintillation phosphor viewed by a multiplier phototube. One scintillator was in the ejected nose tip, energy cut-off (50%) for electrons 3 KeV and protons 10 KeV, and the other in the main payload, energy cut-off 50% for electrons 7 KeV and protons 50 KeV. The fields of view for the 3 and 7 KeV scintillators were 28 and 24 degrees respectively. Figure 3 shows both scintillator outputs from 225 to 325 seconds after launch and an expanded section from 325 to 350 seconds.

The side-viewing 7 KeV scintillator, due to a small precessional motion of the spinning rocket, viewed pitch angles $90^{\circ} \pm 5^{\circ}$ to $90^{\circ} \pm 12^{\circ}$. When viewing $90^{\circ} \pm 12^{\circ}$ the energy changes by a factor of about three, which is about what the EAS data in Figure 2 indicates. The expanded record shows more clearly the spin variations.

Since the ejected nose tip tumbled, pitch angles 0 to 180° were scanned by the 3 KeV scintillator. Due to a level shift in the solid state commutator the data are only good during rocket descent as shown. Two places in the figure (at approximately 240 and 350 seconds) still suffer from cut-off. For 0 to 180° pitch angles there is about two orders of magnitude decrease in energy. For comparison the ESA data on the other rocket were integrated above 3 KeV and a decrease by a factor of about 30 was noted for pitch angles 20° to 160° . Looking at the expanded scale on the right, the flux is relatively constant when the instrument is looking over the upper

hemisphere, which is about 50% of the time. When looking down (pitch angles 90° to 180°) the flux changes very rapidly. Both observations are consistent with Figures 1 and 2 for the other rocket.

There is good agreement between the two scintillator results relative to fine structure variations. Thus, the short time variations of the flux are approximately identical at the three pitch angles 0, 90 and 180 degrees. The largest variation of the flux shown around 350 seconds occurred when the rocket was at 110 km on the far edge of a rapidly developing arc. The increase in flux is especially noticeable at the lower energies. On the other hand, the Astrobee rocket, 60 km higher and 75 km down range at this time observed no variations in flux. The remarkably stable flux in the whole interval from 180 to 360 seconds was noted previously. In fact, in general the short time variations are not correlated at the two rocket positions. A notable exception, however, is the flux increase at 335 seconds time of flight in Figure 3. A corresponding increase was observed on the ESA data at 305 seconds time of flight. This is not very noticeable on the integrated energy flux, but it can be seen very clearly at the lower energies. For example at 3 KeV the increase is about 50%. The ion chamber was looking at high pitch angles and changing rapidly at this time so no correlation is possible. This increase in flux was also characterized by corresponding increases in electron temperature and hyperthermal electron flux. A retarding potential analyzer on the Aerobee rocket showed an increase in electron temperature about 600 degrees and hyperthermal (1.5 eV) electron flux about a factor of four. (Figure 4 and 1 respectively '3'). A retarding potential analyzer on the Astrobee rocket showed an increase by a factor of two in the hyperthermal (5 eV) electron flux. It is interesting that this short time variation extended over such a large area and also was the only one to show corresponding increases in electron temperature and hyperthermal electron flux.

ACKNOWLEDGMENTS

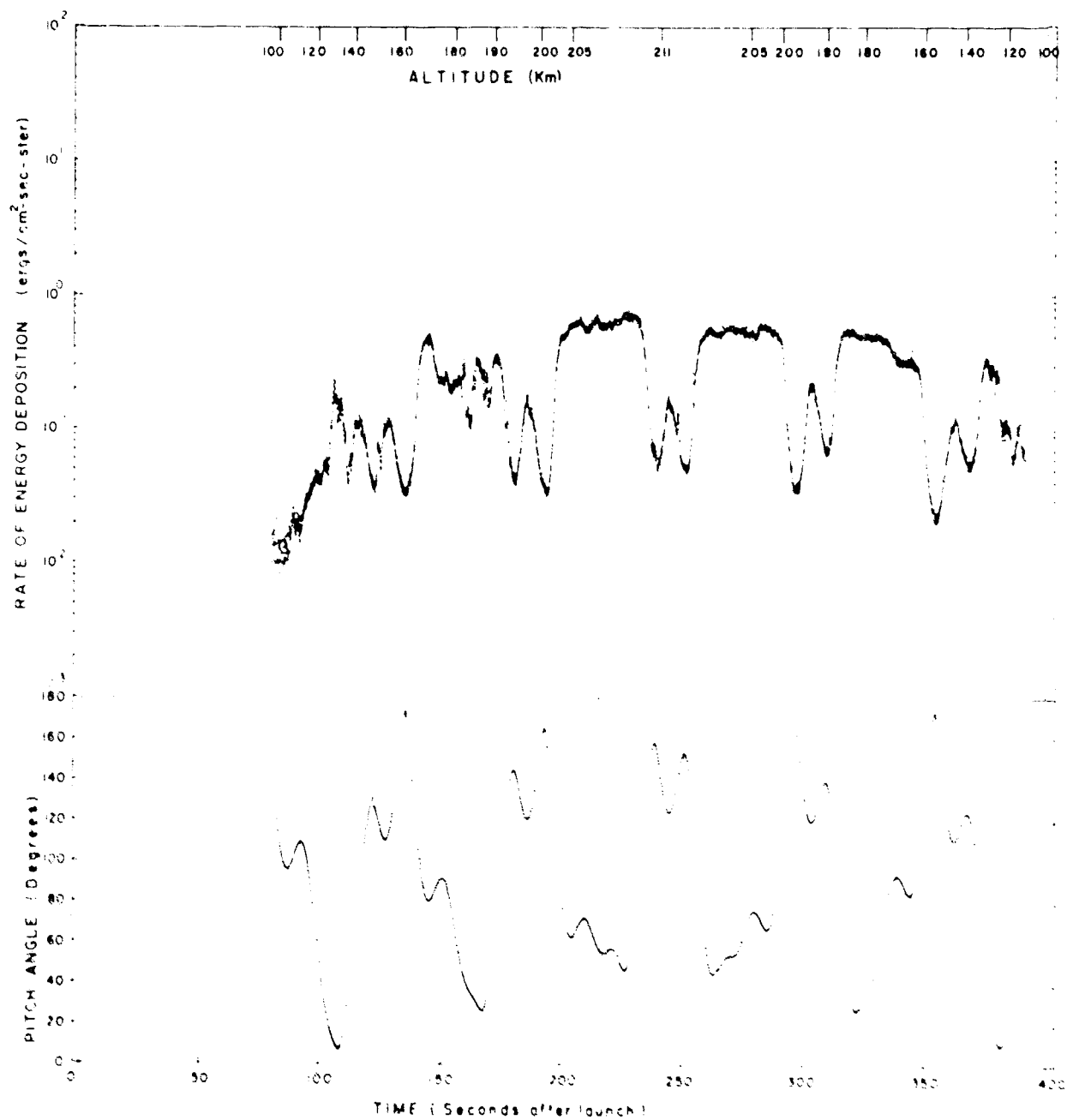
The research in this paper was sponsored in part by the Defense Atomic Support Agency. We wish to acknowledge the staff of the Upper Air Research Laboratory of the University of Utah under the direction of O. C. Haycock and D. A. Burt for conducting the rocket measurements and the staff of the Space Data Analysis Laboratory of Boston College under the direction of R. Marcou and L. Power, Jr. for data reduction.

REFERENCES

1. Reidy, W. P., E. R. Hegblom and J. C. Ulwick, "Low-Energy Electron Spectra in Three Visible Auroras", J. Geophys. Res., 73 3072, 1968.
2. Reidy, W. P., E. R. Hegblom and J. C. Ulwick, "Low Energy Electron Spectra and Angular Distributions", Annales de Geophysique, to be published, 1968.
3. Ulwick, J. C., "Rocket Measurements of the Energy Distribution of Secondary Electrons and Electron Temperatures in Auroras", Annales de Geophysique, to be published, 1968.

FIGURE CAPTIONS

1. Rate of energy deposition and pitch angle vs. time of flight from ion chamber on Astrobe rocket AE 15.735.
2. Pitch angle distributions of 2, 5, 10, and 20 KeV electrons from 170 seconds (190 km rocket ascent) to 310 seconds (190 km rocket descent) for Astrobe rocket AE 15.735.
3. Rate of energy deposition vs time of flight for ejected scintillator ($E \leq 3$ KeV) and main body scintillator ($E > 7$ KeV) Aerobee rocket AF 3.615.



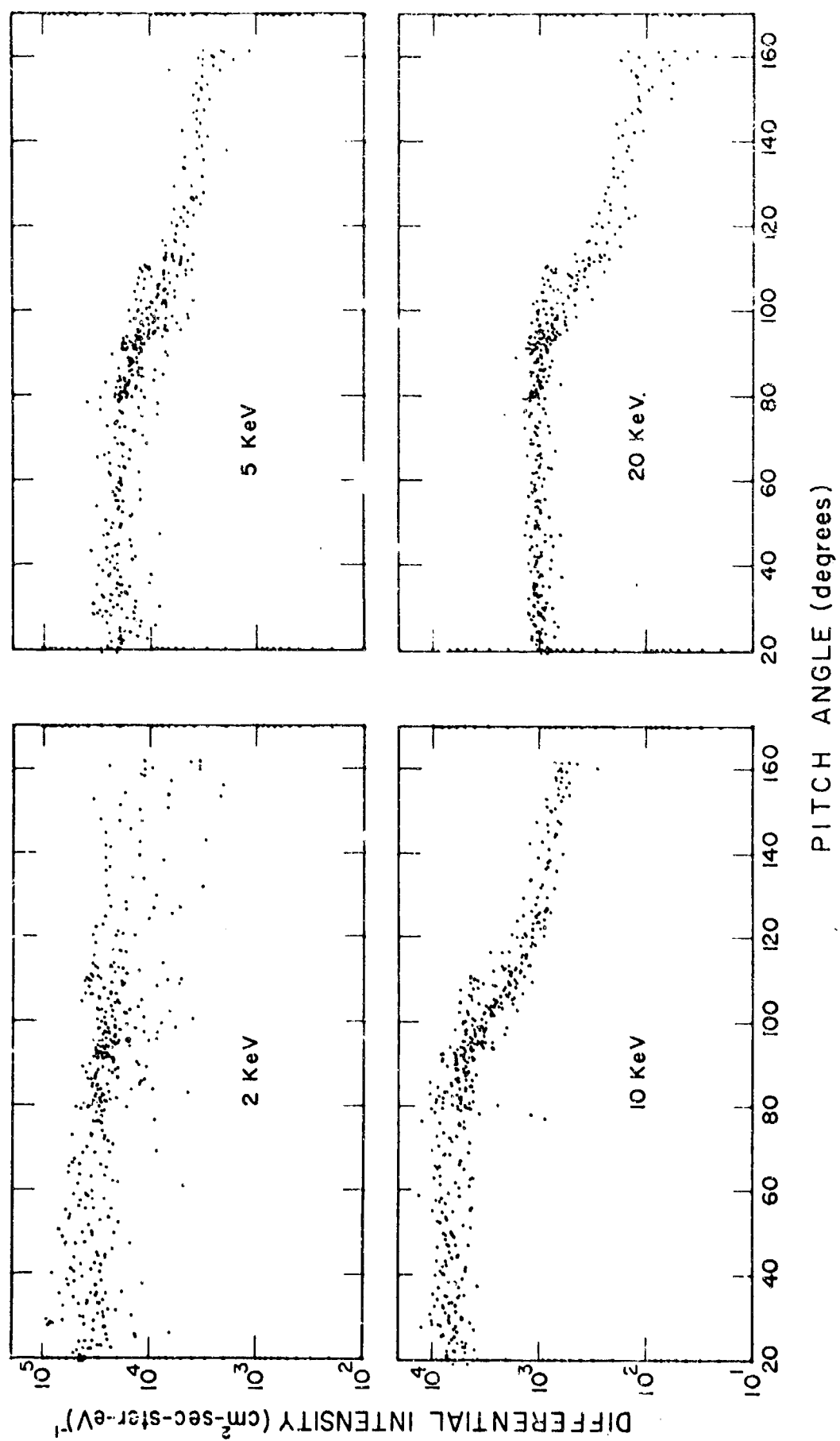
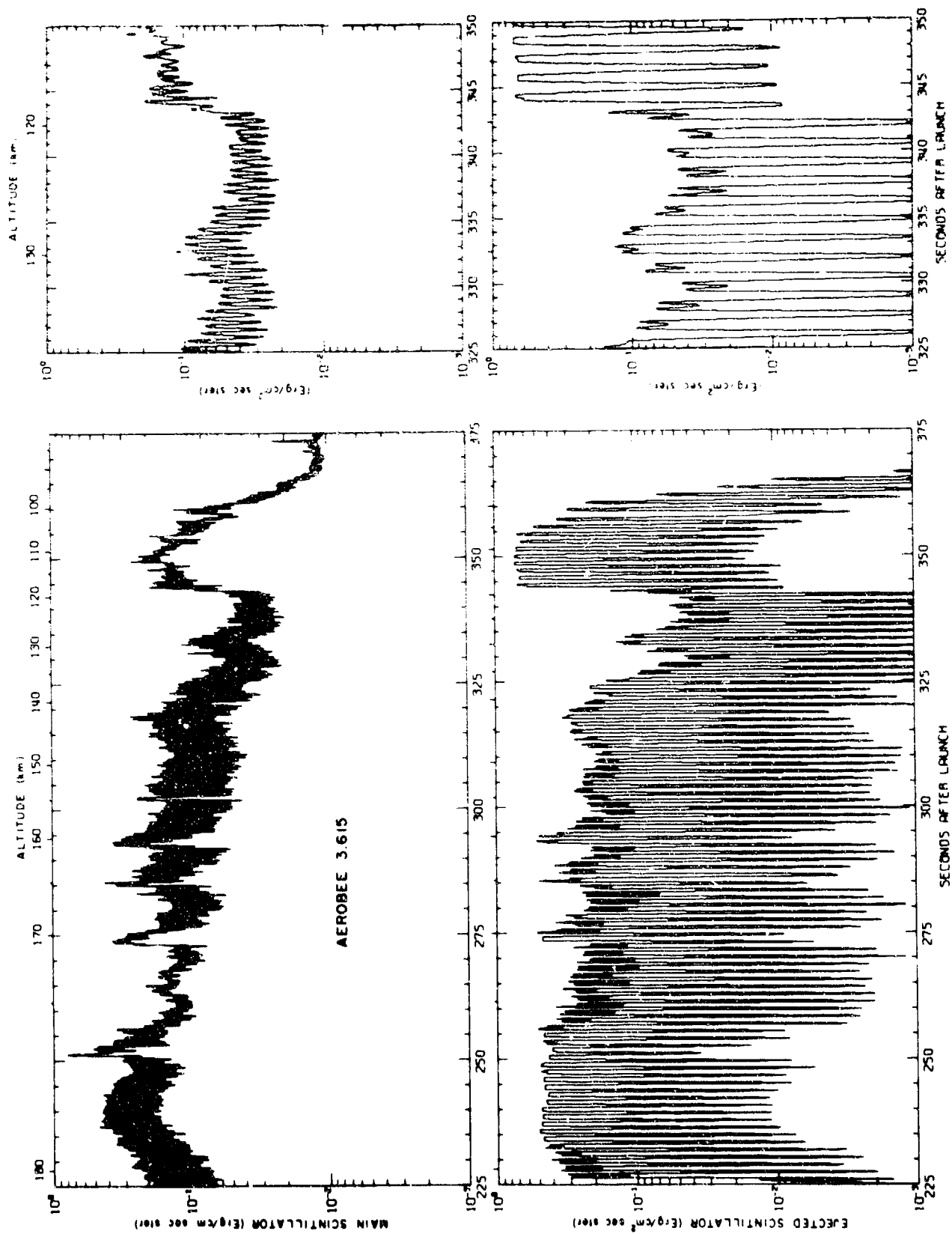


Figure 2



APPENDIX DCharged Particle Transmission Through
Spherical Plate Electrostatic Analyzers*

F. R. Paolini and G. C. Theodoridis
American Science and Engineering, Inc., Cambridge, Massachusetts

ABSTRACT

The transmission characteristics of spherical plate electrostatic analyzers for external sources are studied. Transmission as a function of particle point of incidence, angle of incidence, and kinetic energy, and of analyzer plate geometry (central angle and radii of curvature) and plate potentials, is determined analytically and graphically. Our method (which assumes that the ratio of plate spacing to mean radius is small) uses derived relationships between these parameters and the position of the center of the particle's trajectory, which trajectory is approximated by a circular arc. For a fine incident beam of particles angular resolution at mean transmitted energy and energy resolution at normal incidence are independent of the point of incidence; the angular resolution is moreover a constant and the energy resolution varies linearly with the mean energy. The area of energy-angle transmission diagrams is likewise independent of point of incidence. Energy and angle response functions for diffuse beams of particles are derived semi-empirically. The energy response function (integrated over angle) has the same FWHM as the function for a fine beam incident normally. The angle response function (integrated over energy) has the same FWHM as the function for a fine beam at appropriate fixed energy. Theoretical results for fine beams are compared with experiment and agree well. A practical instrument, specifically for satellite use but suitable for the laboratory, is also described.

*The research reported in this paper was sponsored by, but does not necessarily constitute the opinion of the Air Force Cambridge Research Laboratories, Office of Aerospace Research, under Contract AF 19(628)-5712.

INTRODUCTION

The electrostatic analyzer finds optimum application in the spectral analysis of electrons and protons over the energy range from a few keV to several tens of keV. Faraday cup probes with retarding grids, such as the MIT plasma probe¹, are generally limited to the range below 5 keV due to problems attendant upon the use of much higher voltages. Conventional means of pulse height analysis in scintillators are generally limited to the range above 50 keV due to photomultiplier noise and/or poor energy resolution at low energies. The use of pulse height analysis in proportional counters is limited primarily by window thickness to the range above 40 keV for electrons and 125 keV for protons.

The basic theory of electrostatic analyzers has been presented by Purcell², Rogers³, Ritchie⁴, Birkhoff⁵, and Hubbell⁶. Minkov⁷ furthermore has given an exact solution for the electric field between open spherical segments. The team of Ritchie, Birkhoff, Hubbell et al. have also described a practical instrument for beta ray spectroscopy in which the source is mounted internally⁶. The electrostatic analyzer has not, however, caught on as a laboratory instrument for such work despite its extremely high transmission to resolution ratio. Apparently this is because the practical upper limit of usefulness is about 100 keV. Magnetic analyzers on the other hand can span the range from a few keV to several Mev.

The electrostatic analyzer has been most exploited as a satellite-borne instrument for the spectral analysis of particles in space. In such investigations the analysis of protons from a few to several tens of keV is as essential as the analysis of electrons. Magnetic analyzers are at a definite disadvantage in such an application because of their generally greater weight and power requirements and because of the stiffness of protons of these energies. Internal magnetic fields in a satellite also interfere with sensitive experiments on the measurement of the local geomagnetic and/or interplanetary magnetic fields.

Spherical plate electrostatic analyzers have been used on the Cosmos-12 satellite (Mel'nikov et al.⁸), on Hitch-Hiker I (Paolini et al.⁹), on Vela satellites (Coon¹⁰ and Bame et al.¹¹) and on IMP-I (Wolfe et al.¹²). Descriptions of similar satellite instruments (including cylindrical plate analyzers) have also been given by Bader et al.¹³ and Frank¹⁴.

In this paper the transmission characteristics of spherical plate analyzers for external sources are studied. Transmission as a function of analyzer plate geometry (central angle and radii of curvature) and plate potentials, and of particle point of incidence, angle of incidence, and kinetic energy is first determined both analytically and graphically. Our method of analysis (which assumes that the ratio of plate spacing to mean plate radius is small) uses derived relationships between these parameters and the position of the center of a particle's trajectory, which trajectory is approximated by a circular arc. Theoretical results are next compared with experiment. Response functions for diffuse incident beams are then derived semi-empirically. Finally, a practical instrument is described, suitable for laboratory or satellite use.

THEORY

We initially define the following geometrical parameters, illustrated in Figure 1:

- ϕ_0 , central angle subtended by each analyzer plate;
- R_0 , outer plate radius of curvature;
- R_i , inner plate radius;
- ΔR , separation of plates; in the present case, $\Delta R = R_0 - R_i$;
- r, ϕ , usual polar coordinates with origin at O in Figure 1; ϕ is measured clockwise from OA ;
- $A(r_0, 0)$, point of incidence of particle within entrance aperture;
- α , angle of incidence of particle with respect to normal to diameter AOP lying within the entrance aperture; sense defined as shown;
- m, n , measures of position of incident particle, as shown; $m+n=1$.

The electrostatic force on a particle in the potential field generated between two completely closed spherical metal surfaces is central. Particle angular momentum and total energy are therefore conserved and motion is in a plane. In the following analysis we assume that the same is true for spherical segments; this amounts to neglecting fringing field effects. In following the development of equations (1) through (8) it may be helpful to refer to Goldstein¹⁵. We further define:

q , the charge of the particle being analyzed including its conventional algebraic sign; thus, q is $+e$ for a proton and $-e$ for an electron, where e is the magnitude of the electronic charge;

V , the potential difference $V_o - V_i$ between outer and inner plate potentials, V_o and V_i respectively;

$\Phi(r)$, the electrostatic potential energy of a particle in the field between the plates at point (r, ϕ) ;

$T(r)$, the kinetic energy of a particle at point (r, ϕ) ;

T_∞ , the kinetic energy of a particle which will be incident at $A(r_o, 0)$ when the particle is far distant from the instrument, i.e., what one usually means by the particle's energy.

We have that

$$\Phi(r) = -Kr^{-1} + \Phi_\infty \quad (1)$$

where

$$K = qVR_oR_i/\Delta R \quad (2)$$

and Φ_∞ is a gauge constant determined by the absolute potentials on each plate. For example, with "balanced plates", i.e., with potentials of $+\frac{1}{2}V$ and $-\frac{1}{2}V$ on outer and inner plates respectively, we would have

$$\Phi_\infty = qV(R_o + R_i)/2\Delta R.$$

We note that

$$T_\infty = T(r) + \Phi(r) = T(r) - Kr^{-1} + \Phi_\infty. \quad (3)$$

T_{∞} is conserved, and Φ_{∞} is a constant; also conserved, therefore, is the energy E defined by the equation

$$E \equiv T_{\infty} - \Phi_{\infty} = T(r) - Kr^{-1} \quad . \quad (4)$$

For particles transmitted through the analyzer plates $E < 0$ and the trajectory is an ellipse. The major semi-axis a is given by the relation

$$a = -K/2E \quad (5)$$

and the eccentricity ϵ is given by the equation

$$\epsilon = \left[1 + 2EL^2/MK^2 \right]^{\frac{1}{2}} \quad (6)$$

where M is the particle mass and L its angular momentum. L is related to $T(r_0)$ at the point of incidence $A(r_0, 0)$ for an arbitrary angle of incidence α through the expression

$$L^2 = 2Mr_0^2 T(r_0) \cos^2 \alpha \quad . \quad (7)$$

The equation of the elliptical trajectory is given by

$$r = a(1-\epsilon)^2 \left[1 + \epsilon \cos(\phi - \phi') \right]^{-1} \quad (8)$$

where ϕ' , the angle of the apsides, may be evaluated from the boundary conditions at $A(r_0, 0)$.

For a particle entering at A with $\alpha = 0^\circ$, it follows from equations (5), (6), and (7) that the trajectory will be a circle if

$$E = -K/2r_0 \quad . \quad (9)$$

From equations (9) and (4), it then follows that

$$T(r_0) = K/2r_0 = -E \quad . \quad (10)$$

We now consider the effect of varying α about $\alpha = 0^\circ$ while E remains fixed at the value given in equation (9). From equations (5) through (10) there follow that

$$\begin{aligned} a &= r_0 \quad , \\ \epsilon &= |\sin \alpha| \approx |\alpha| \quad , \\ \phi' &= \frac{1}{2}\pi - \alpha \quad , \quad \text{and} \\ 2\epsilon &= r_0 |\sin \alpha| \approx r_0 |\alpha| \equiv y \quad , \end{aligned} \quad (11)$$

where ΔE is the displacement of the trajectory center (the semi-separation of the foci) and approximations hold for α small. The originally circular trajectory becomes an ellipse with one focus at the center O , the second focus on a circle of radius r_0 with center at A , and the center of the ellipse midway between. Figure 1 shows second foci F' and F'' and displaced centers O' and O'' of trajectories of particles tangent respectively to outer and inner plates of a 180° analyzer. For these cases, the respective limiting angles of incidence $\Delta\alpha_+$ and $\Delta\alpha_-$ are thus given by the relations

$$\begin{aligned} r_0 \sin \Delta\alpha_+ &= m \Delta R \quad \text{and} \\ -r_0 \sin \Delta\alpha_- &= n \Delta R . \end{aligned} \quad (12)$$

For $\Delta R/r_0$ small (therefore $\Delta\alpha_+$ and $\Delta\alpha_-$ small) we have that

$$\begin{aligned} \Delta\alpha_+ &\approx m \Delta R / r_0 , \\ -\Delta\alpha_- &\approx n \Delta R / r_0 , \quad \text{and} \\ \Delta\alpha_w &\equiv (\Delta\alpha_+ + |\Delta\alpha_-|) \approx \Delta R / r_0 \approx \text{const.} . \end{aligned} \quad (13)$$

We next consider the effect of varying E about the value given in equation (9) while α remains fixed at 0° . From equations (5) through (10) there follow that

$$\begin{aligned} \epsilon &= |\Delta E / E| , \\ \phi &= 0 , \quad \text{and} \\ \Delta E &= r_0 |\Delta E (E + \Delta E)^{-1}| \approx r_0 |\Delta E / E| \equiv \chi . \end{aligned} \quad (14)$$

Equations (14) are exact for a finite change ΔE in energy where indicated; approximations hold for ΔE small. The originally circular trajectory becomes an ellipse with one focus at O , and the second focus located on the diameter AOP of Figure 2. Figure 2 shows second foci F' and F'' , and displaced centers O' and O'' , of trajectories of particles tangent respectively to outer and inner plates (at the exit aperture) of a 180° analyzer. For these cases respective

limiting energies ΔE_+ and ΔE_- follow from equation (5) and are given by the expressions

$$\begin{aligned} E + \Delta E_+ &= -K(2r_0 + m\Delta R)^{-1}, \text{ and} \\ E + \Delta E_- &= -K(2r_0 - n\Delta R)^{-1}. \end{aligned} \quad (15)$$

For $\Delta R/r_0$ small (ΔE_+ and ΔE_- therefore small) equations (15) lead to the approximations

$$\begin{aligned} -\Delta E_+/E &\approx m\Delta R/2r_0, \\ -\Delta E_-/E &\approx -n\Delta R/2r_0, \text{ and} \\ -\Delta E_w/E &\equiv -(\Delta E_+ + |\Delta E_-|)E^{-1} \approx \Delta R/2r_0 \approx \text{const.} \end{aligned} \quad (16)$$

For $\Delta R/r_0$ small we have shown that variations in the angle of incidence α about the normal to the diameter AOP lying in the entrance aperture in the plane of the trajectory produce displacements of trajectory centers (and foci) perpendicular to the diameter and that variations in the particle energy E about the energy corresponding to a circular trajectory produces displacements of trajectory centers (and foci) along the diameter. We have furthermore derived explicit relationships between orbital parameters and energy/angle variations.

We next consider the general problem of determining energy/angle values which allow transmission of particles incident at an arbitrary point **A** in the entrance aperture. It is clear that these values are determinable through equations (5), (11), and (14) if the locus of centers of trajectories of transmitted particles are known. The problem of determining this locus is simplified greatly if we can legitimately approximate such elliptical trajectories by circles.

Taking the major semi-axis a of the ellipse as the radius of the approximating circle, the maximum radial deviation Δr between the two curves is given by

$$\Delta r = a - b = a \left[1 - (1 - \epsilon^2)^{\frac{1}{2}} \right] \quad (17)$$

where b is the minor semi-axis. The maximum value of ϵ is of the order of

$\Delta R/r_0$ (see equations 11 and 13) which by hypothesis is much less than 1. Thus, since $a \approx r_0$ it follows that

$$\Delta r \approx \frac{1}{2} \Delta R (\Delta R/r_0) \ll \Delta R . \quad (18)$$

In most cases ϵ will be less than $\Delta R/r_0$. In some instances, e.g., as illustrated in Figure 2, limits depend only on the length of the major axis and the approximation will introduce no error at all. The approximation thus seems a very good one. We finally point out that the error introduced by the approximation can be exactly evaluated if (after the approximate determination of the locus) it is felt that a correction is necessary.

We can now proceed to examine the general problem. We refer to Figure 3 for the following development. The boundary of the region of allowed trajectory centers is the locus of the centers of those trajectories that are tangent to the outer or inner plate and/or go through the points J or L at the ^{exit} aperture, i.e., which graze the plates somewhere. The complete set of limiting trajectories therefore comprise four distinct classes.

(1) Trajectories tangent to the outer plate with exit points between J and L. B is the center of the trajectory tangent to the outer plate at L and is therefore the intersection of OL (a part of the major axis) with the perpendicular bisector of AL (since AB = BL = a). In general, the center C of the trajectory tangent to the outer plate at C', at an arbitrary polar angle ϕ , and with an exit point between J and L, is at the intersection of OC' with the perpendicular bisector of AC'. The displacement OC of the center is therefore, to first order in $m\Delta R$, given by the relation

$$\begin{aligned} (OC) &= m\Delta R + (OC)\cos\phi & \text{or} \\ (OC) &= m\Delta R (1 - \cos\phi)^{-1} . & (19) \end{aligned}$$

This locus is a parabola opening to the left. The center D of the trajectory tangent to the outer plate, and with exit point at J , lies on the perpendicular bisector of AJ . The angular coordinate of D , call it ϕ_D , may be most conveniently found from the expression (correct to first order in $\Delta R/r_0$)

$$\cot \frac{1}{2} \phi_D = \cot \frac{1}{2} \phi_0 + m^{-\frac{1}{2}} \csc \frac{1}{2} \phi_0. \quad (20)$$

For $m \rightarrow 1$, $\phi_D \rightarrow \frac{1}{2} \phi_0$; for $m \rightarrow 0$, $\phi_D \rightarrow 0$.

Equation (20) assumes that $\frac{1}{2} \pi < \phi_0 < \pi$.

(2) Trajectories tangent to neither plate with exit point at J . The centers of these trajectories lie along the perpendicular bisector of AJ between the points D and E . E is the center of the trajectory tangent to the inner plate at J and is therefore the intersection of OJ (a part of the major axis) with the perpendicular bisector of AJ . DE is approximately parallel to the bisector of the angle ϕ_0 ; for ϕ_0 equal to 180° , it is exactly so.

(3) Trajectories tangent to the inner plate with exit points between J and L . The center G of a trajectory tangent to the inner plate at an arbitrary point G' with angular coordinate ϕ is at the intersection of OG' with the perpendicular bisector of AG' . The displacement of the center is, to first order in $n\Delta R$, given by the relation

$$(OG) = n\Delta R + (OG) \cos \phi \quad \text{or}$$

$$(OG) = n\Delta R (1 - \cos \phi)^{-1} = n\Delta R [1 + \cos(\pi + \phi)]^{-1}. \quad (21)$$

This locus is a parabola opening to the right, where all coordinate angles are defined so that $0 < \phi < \pi$. (In Figure 3, for example, the same angle ϕ corresponds to the locus points C and G .) The center H of the trajectory tangent to the inner plate and with exit point at L , lies on the perpendicular bisector of AL . The angular coordinate of H , call it ϕ_H , can be found from an equation similar to (20), with n replacing m .

(4) Trajectories tangent to neither plate, with exit point at L . The centers of these trajectories lie along the perpendicular bisector of AL , between points H and B . The line BH , as well as the line DE , is approximately parallel to the bisector of the angle ϕ_0 , and is exactly so for $\phi_0 = 180^\circ$. BH and DE are tangent to the curves BCD and EHG respectively.

The energy angle factor $\langle \Delta \alpha \Delta E \rangle$, which gives the area in $E-\alpha$ space of values of E and α which allow transmission of a particle for an arbitrary point of incidence, is calculated from the area Δ^2 of the locus of allowed trajectory centers by the relation

$$\langle \Delta \alpha \Delta E \rangle = (-E/r_0)(1/r_0) \Delta^2 = qV R_0 R_i \Delta^2 / 2 r_0^3 \Delta R \approx qV \Delta^2 / 2 r_0 \Delta R \quad (22)$$

which follows from equations (11), (14), (9), and (2). The area Δ^2 can be approximated by the area of the quadrilateral $DEHB$ which is almost a trapezoid. DE and HB are nearly parallel with perpendicular separation p given approximately by the equation

$$p = \Delta R / 2 \sin \frac{1}{2} \phi_0 \quad (23)$$

The lengths of BH and DE can be found from the approximations

$$R_i + (BH) - (OB) \sin \frac{1}{2} (\pi - \phi_0) \approx n \Delta R + R_i + (OB) \cos (\pi - \phi_0) + (BH) \cos \frac{1}{2} \phi_0 \quad \text{and}$$

$$R_0 - (DE) + (OE) \sin \frac{1}{2} (\pi - \phi_0) \approx n \Delta R + R_i - (OE) \cos (\pi - \phi_0) - (DE) \cos \frac{1}{2} \phi_0 ,$$

which simplify to the expressions

$$\begin{aligned} (BH)(\Delta R)^{-1} \sin^2 \frac{1}{2} \phi_0 &= \frac{1}{2} (1+n) + \cos \frac{1}{2} \phi_0 \quad \text{and} \\ (DE)(\Delta R)^{-1} \sin^2 \frac{1}{2} \phi_0 &= \frac{1}{2} (1+m) + \cos \frac{1}{2} \phi_0 \quad (24) \end{aligned}$$

It therefore follows that

$$\Delta^2 \approx \frac{1}{2} p [(BH) + (DE)] = \frac{1}{2} \Delta R^2 \csc^3 \frac{1}{2} \phi_0 \left(\frac{3}{4} + \cos \frac{1}{2} \phi_0 \right) \quad (25)$$

so that

$$\langle \Delta\alpha\Delta E \rangle \approx -\frac{1}{2}E(\Delta R/r_o)^2 \csc^3 \frac{1}{2}\phi_o \left(\frac{3}{4} + \cos \frac{1}{2}\phi_o \right)$$

or

$$\langle \Delta\alpha\Delta E \rangle \approx \frac{1}{4}qV(\Delta R/r_o) \left[\csc^3 \frac{1}{2}\phi_o \left(\frac{3}{4} + \cos \frac{1}{2}\phi_o \right) \right] . \quad (26)$$

If s is the arc length of the entrance aperture (along a circle of radius r_o), and $\Delta\beta$ (assumed small) is the angular aperture of the plates in the plane normal to the plane of the trajectory, the complete energy-geometrical factor $\langle A\Omega\Delta E \rangle$ is then given by the relation

$$\langle A\Omega\Delta E \rangle \approx s\Delta R\Delta\beta \langle \Delta\alpha\Delta E \rangle . \quad (27)$$

The dependence of this factor on ϕ_o is determined by the bracketed term in equation (26); this is plotted as a function of ϕ_o in Figure 4. The bracketed term increases from a value of 0.75 for ϕ_o equal to 180° , to a value of about 1.5 at 135° .

We note from equation (26) that $\langle \Delta\alpha\Delta E \rangle$ depends on position within the entrance aperture only through r_o and is therefore essentially constant. The factor $\langle \Delta\alpha\Delta E \rangle$ furthermore varies linearly with V (or E or T_∞); thus $\langle A\Omega\Delta E \rangle/E$ is nearly constant and the instrument has a nearly constant percentage energy resolution.

In dealing with practical instruments it is convenient to define some additional parameters. We limit our discussion to analyzers used in a balanced configuration (that is, with potentials of equal magnitudes but opposite polarities) applied to the plates, but similar relations may be derived for arbitrary plate potentials. We define an average radius \bar{R} by the equation

$$\bar{R} \equiv 2R_o R_i (R_o + R_i)^{-1} . \quad (28)$$

This is the radius of the 0 volt equipotential surface. We define the energies \bar{E} and \bar{T}_∞ corresponding to a particle whose trajectory lies within this surface (i.e., incident normally at $r = \bar{R}$, and having a circular trajectory). There consequently follow from equations (5) and (4) the relations

$$\bar{E} = -\frac{1}{2} K \bar{R}^{-1} = \bar{T}_\infty - K \bar{R}^{-1} \quad \text{and} \quad \bar{T}_\infty = \frac{1}{2} K \bar{R}^{-1} = -\bar{E} \quad (29)$$

Substituting equations ^{(2) and} (28) in (29), we obtain the expression

$$\bar{T}_\infty = \frac{1}{2} k q V = k q V_0 \quad (30)$$

where k , the "calibration factor" of the analyzer system, is defined by the equation

$$k = \frac{1}{2} (R_0 + R_i)(R_0 - R_i)^{-1} \quad (31)$$

and is a function of plate geometry only. For a 180° electrostatic analyzer we also have, from equations (16), (28), (31) and (13), that

$$-\Delta E_w / \bar{E} = \Delta E_w / \bar{T}_\infty = \frac{1}{2} (\Delta R / \bar{R}) \approx \frac{1}{2} k^{-1} [1 + (\Delta R / 2 R_i)^2] \approx \frac{1}{2} k^{-1} \quad (32)$$

$$\text{and} \quad \Delta \alpha_w = \Delta R / \bar{R} \approx k^{-1} \quad (33)$$

EXPERIMENTAL RESULTS

The results of the preceding analysis were compared with experimental results. A pair of spherical electrostatic analyzer plates with the following geometry was used: ϕ_0 , $180^\circ \pm 1/2^\circ$; R_0 , 2.242 ± 0.001 in.; R_i , 1.974 ± 0.001 in.; ΔR , 0.268 ± 0.002 in.; \bar{R} , 2.100 ± 0.002 in.; k , 7.87 ± 0.06 .

Figure 5 shows the important features of the experimental setup. The pair of analyzer plates was mounted on a goniometer whose rotation axis passed through the plane of the entrance aperture. The goniometer was remotely driven by a stepping motor in steps of 1° . Positive potential was applied to the inner analyzer plate from a Fluke Model 421B High Voltage Power Supply, variable from 0 to +2.1 kV. The finest control knob on this supply is calibrated in units of 0.1V, and can be read to 0.01V. Absolute calibration accuracy is $\pm 0.25\%$ ($\pm 2.5V$ at +1000 V). Negative potential was applied to the outer analyzer plate from a Fluke Model 408A DC Power Supply, variable from 0.5 to 6.0 kV. Its finest control knob is calibrated in units of 1.V and can be read to 0.1V. Absolute calibration accuracy is $\pm 0.25\%$, ($\pm 2.5V$ at -1000 V).

A commercial cathode ray tube electron gun with a 20 kV rating was used as an electron source. The beam diameter was 0.040 inches. The gun accelerating potential was established with a Northeast Scientific Corporation Model RE-10010 Regulated High-Voltage Supply, variable from -1 to -10 kV. Its finest control knob is calibrated in units of 10.V and can be read to 1.V. Absolute calibration accuracy is $\pm 2\%$, or about $\pm 150V$ in the vicinity of 7.5 kV. The electron beam could be steered by means of vertical and horizontal electrostatic deflection plates.

The electron beam was introduced at specific points on the entrance aperture at various angles of incidence; incident beam current was maintained at roughly $10\mu A$. Transmitted current was measured with a Faraday cup connected to a Keithley Model 411 Micro-microammeter (range 10^{-13} to 10^{-3} amperes). Earlier experiments had established that 100% peak transmission is attainable with the spherical plate analyzer under these experimental conditions, so it was considered unnecessary to monitor input current in these experiments.

The determination of position within the entrance aperture (i.e., the parameters m and n) was facilitated by using a phosphorescent coating on the ground plane around the entrance aperture. By applying a vertical deflection only the beam could be brought onto some of the coated area and m and n estimated by eye to ± 0.1 .

In comparing theory with experiment, major sources of error could be due to:

- (1) Finite electron beam diameter; a 0.04 inch displacement on the entrance aperture produces effects equivalent to a 150.V electron energy change.
- (2) Errors in estimating m (or n); an error of ± 0.1 produces effects equivalent to a $\pm 150.V$ electron energy change.
- (3) The $\pm 2\%$ calibration accuracy of the electron gun power supply; this corresponds to an uncertainty in $(-E)$ or T_{∞} of $\pm 150.V$.
- (4) The minimum of 1° in the angular displacement that is possible with the present goniometer; this limits the accuracy in the absolute measurement of α .
- (5) Uncertainty in the electron beam direction; this amounts to about $\pm 0.5^\circ$ due to uncertainty in the alignment of the electron gun filament and electrodes.
- (6) Possible analyzer plate misalignment, e.g. the centers of curvatures of the plates not coincident; the resulting error in angle of incidence is estimated to be about $\pm 1/2^\circ$.
- (7) Fringing fields at entrance and exit apertures; such systematic errors were estimated to be of the order of -1° (in the convention of Figure 1).

Deflection due to the earth's magnetic field and due to voltages on the horizontal deflection plates of the electron gun (used to vary the point of incidence of the electron beam) were corrected for.

Figure 6 shows typical experimental transmission curves: in 6a as a function of energy (at fixed angle of incidence) and in 6b as a function of angle of incidence (at fixed energy). The side peaks in Figure 6a are due to scattering off the plates and may be effectively eliminated by various mechanical means such as "grooving". (See, for example, Hubbel' et al⁶.) The experimentally determined resolution is poorer than the theoretical value partly due to this scattering. The fringing field also contributes to poorer resolution because of an effective reduction in ϕ_0 . The experimental value is even so seen to be within 10% of the theoretical value. If the absolute magnitude of the particle energy is made to agree with the theoretical value then the angle for which it applies is $\sim 2^\circ$ off as indicated in Figure 6b. This angular discrepancy is, however, consistent with magnitudes of anticipated errors.

Figure 7 gives theoretical transmission diagrams in the E - α plane compared with 50% transmission points determined experimentally by finding the energy limits at various fixed angles of incidence. Each set of experimental points has been shifted by the indicated amount of energy δE and the indicated amount of angle $\delta \alpha$ to give the best fit to the theoretical diagram. The magnitudes of such corrections are consistent with the magnitudes of the errors anticipated in comments (1) through (7) above.

Experimental errors thus prevent a fully detailed comparison between experiment and theory. The present experiment is nevertheless sufficiently accurate to permit comparisons in shapes of diagrams (as distinguished from locations of centroids of diagrams). This is because only finite changes ΔT_∞ (equal to the change in electron gun voltage) and $\Delta \alpha$ ($\approx 1^\circ$) are required to define a shape and these changes are very accurately determinable. Theoretical and experimental shapes are indeed consistent within the accuracy of the approximations used in the theoretical analysis. Specifically we verify equations (13), (16), (26), (32), and (33).

SEMI-EMPIRICAL RESULTS

The response of the instrument to a unidirectional, monoenergetic, diffuse beam of particles (which irradiates the whole entrance aperture) can be determined by integrating the response to a fine beam over the area of the entrance aperture. From diagrams such as those in Figure 7, a matrix, whose elements are relative transmissions for energy-angle (finite) differentials, may be composed. Such a matrix, derived from 7 full areal elements and 2 half elements, is presented in Table I. Rows are labeled by angle of incidence α ; the interval of each angular element is from $(\alpha - 0.5)$ to $(\alpha + 0.5)$ degrees. Columns are labeled by kinetic energy T_{∞} ; the interval of each energy element is from $(T_{\infty} - 0.025)$ to $(T_{\infty} + 0.025)$ keV. Each row of the matrix, plotted versus energy, thus gives an energy response function for a unidirectional diffuse beam; various such functions are shown in Figure 8. Each column of the matrix, plotted versus angle, gives an angular response function for a monoenergetic diffuse beam; some such functions are plotted in Figure 9.

Sums of the elements of the columns (equivalent to integrating over angle) give an energy response function for an isotropic diffuse beam. This function is plotted in Figure 10a. In measuring trapped radiation in space, within the narrow angular aperture of the instrument (except when looking near atmospheric cut-off pitch angles), the angular distribution does not vary much and can be considered constant. The width of the function in Figure 10a therefore is the effective energy bin width of the instrument in such an application. It is interesting to note that this function has the same FWHM value as the function for a fine beam although its shape is triangular rather than rectangular.

Sums of the elements of the rows (equivalent to integrating over energy) give an angular response function for a diffuse beam having a flat energy spectrum. This function is plotted in Figure 10b. In measuring trapped radiation in space, within the narrow energy bin of the instrument, spectra do not vary much and can be considered flat. The width of the function in Figure 10b is therefore the effective angular aperture of the instrument in such an application and is the factor to be used in calculating the geometrical factor. Note that this angular response function has the same FWHM value as the function for a fine beam although its shape is curved rather than rectangular.

DESCRIPTION OF A PRACTICAL INSTRUMENT

Figure 11 gives photographs of an electrostatic analyzer (ESA) developed for spacecraft use.* Table II gives a summary of its principle characteristics.

A Bendix magnetic electron multiplier (MEM) Model M-306 is used as a quantum detector for both protons and electrons. This permits detection of individual low energy particles (protons especially) which would be stopped by a vacuum window or any other intervening material. This device is fairly small, rugged, and relatively unaffected by exposure to air; it is relatively solar-blind, has low noise (less than 0.1 pulse/sec observed) and high gain (10^6 to 10^7). The quantum efficiency of one of these detectors varied from about 5 to 15% over the range 2 to 100 keV for electrons and from about 15% to 20% over the range 30 keV to 100 keV for protons. The MEM is described in the literature by Goodrich and Wiley¹⁶.

Figure 12 is a block diagram of the ESA as it will be used in a flight on OV1-9. The MEM is operated with grounded dynode strip input and magnet structure so that either protons or electrons can be detected with negligible deceleration. (The magnetic fringing field imposes a lower limit of about 2 keV on electrons.) Pulses from the MEM are amplified, discriminated, shaped and counted in the Logarithmic Count Rate Meter (LCRM) and in the Scaler.

The electrostatic analyzer plates are driven by a programmable high voltage power supply manufactured to our specifications by MIL Associates and designated Model S-22-2-200 UHV. This supply consists essentially of a chopper feeding two voltage-multiplying diode pumps, one for generating positive, the other negative, voltage. The output voltage from the positive pump is divided and compared with a programmed reference in a high gain difference amplifier whose output is used in a negative feed-back loop to control the chopper pulse amplitude. The reference voltage for the difference amplifier is one of eight discrete values defining a geometric progression of mean energies of particles to be transmitted by the analyzer plates over a decade range. On every eighth frame of the

* Under Air Force Contract AF 19(628)-5209

telemetry commutator the high voltage division is changed by a factor of ten thereby changing the range of energies covered by the analyzer by the same factor. This method of covering 1 to 100 keV in 16 channels allows the use of a modular 8 point electronic commutator, reduces the number of components required, and gives more stable energy threshold definition. On every sixteenth frame of the telemetry commutator a latching relay, activating a high voltage commutating switch, reverses the polarity of the voltages applied to the analyzer plates. This happens at minimum values of the plate voltage to minimize switching currents. The ESA is thereby converted from an electron to a proton analyzer or vice versa.

The potential difference between the analyzer plates is monitored by a logarithmic difference amplifier. This not only identifies in which mode the ESA is working (electron or proton) by indicating the voltage polarities but also gives direct information on the magnitudes of the applied plate voltages and therefore on the energy to which the ESA is tuned.

The sync pulse which switches energy levels is phased with respect to the data points fed by the ESA so that all data points of one complete telemetry data frame pertain to the same energy level. This is accomplished on OV1-9 by using a two-ring commutator; only one ring is used for data and the other (the sync pulse ring) with its wiper returned to ground is used for switching. Appropriate outputs of the three flip-flops in the electronic commutator and the two flip-flops in the range-polarity control (controlling the voltage divider and the latching relay) are connected in a standard resistance ladder so as to generate a 32 step staircase, each step of which identifies scaler states and therefore the energy and particle mode being used.

The scaler is for counting pulse repetition rates below 10 counts/sec, the lower useful limit of the LCRM. It is reset once per data frame by an appropriately timed pulse from the sync pulse ring. A command line is available for resetting the instrument to the lowest electron energy bin. The MEM high voltage is monitored to check proper functioning. Auger electrons from an Fe-55

source mounted at the entrance aperture of the analyzer plates give counts in the two lower electron channels thereby providing in-flight calibration.

A Kaman Nuclear Corporation electron/proton accelerator was used in calibrating the instrument between 30 and 100 keV. The calibration factor was adequately determined using the 0 to 20 keV electron gun but determination of MEM detector efficiency necessitated the use of the accelerator.

The energy-geometrical factor $\langle A\Omega\Delta E \rangle$ was first calculated from energy and angle parameters determined with the 20 keV electron gun and was later checked using a uniformly distributed, accurately assayed, Pm-147 source (230 keV beta end point energy) which completely covered the extreme entrance aperture.

The instrument shown underwent environmental tests (acceleration, vibration, shock, temperature, and vacuum) as specified for Air Force Blue Scout vehicles.

SUMMARY

We can summarize our findings on electrostatic analyzers, for $\Delta R/r_0 \ll 1$, as follows:

- (1) For a particle with an arbitrary point of incidence within the entrance aperture deviations in the angle of incidence (about normal incidence) and energy (about the energy giving a circular trajectory) cause approximately orthogonal displacements of the center of the particle's trajectory (which becomes an ellipse) uniquely defined by the angle/energy deviations.
- (2) The perturbed (elliptical) trajectory can be approximated by a circle (to second order).
- (3) Centers of trajectories of particles which are transmitted, i. e., allowed trajectories, lie within an area whose boundaries can be determined graphically and analytically.
- (4) Equations (11) and (14) relate trajectory center displacements with angle α and relative energy deviations $\Delta E/E$; r_0 is defined by the point of incidence. Equations (9) and (4) subsequently relate E to T_∞ .
- (5) For a fine beam of incident particles, angular resolution $\Delta\alpha_w$ at mean transmitted energy is independent of the point of incidence although limits on α vary; $\Delta\alpha_w$ is moreover a constant.
- (6) For a fine beam, energy resolution ΔE_w at normal incidence is independent of the point of incidence although limits on E vary; moreover ΔE_w varies linearly with E so that percentage resolution is constant.
- (7) The area of energy-angle transmission diagrams $\langle \Delta\alpha \Delta E \rangle$ is likewise independent of the point of incidence and changes by about a factor of two as the analyzer central angle ϕ_0 varies from 180° to 135° .
- (8) From energy-angle transmission diagrams, energy and angle response functions for diffuse beams of particles may be derived.

(9) For a diffuse beam of incident particles, the semi-empirical energy response function (obtained by integrating over angle of incidence) has the same FWHM as the function for a fine beam incident normally; its shape is triangular rather than rectangular, however.

(10) For a diffuse beam, the semi-empirical angle response function (obtained by integrating over energy) has the same FWHM as the function for a fine beam at appropriate fixed energy; its shape is curved rather than rectangular, however.

(11) For $\phi_0 = 180^\circ$, with + and - potentials of equal magnitude applied to analyzer plates, the following relations hold for both fine and diffuse particle beams:

$$-\bar{E} = \bar{T}_\infty = kqV_0 ,$$

$$\Delta E_w / \bar{T}_\infty = \frac{1}{2} k^{-1} \quad \text{and} \quad \Delta \alpha_w = k^{-1} .$$

where k is defined in equation (31).

(12) Agreement between experiment and theory is good.

FOOT NOTES

1. H.S. Bridge, A. Egidi, A. Lazarus, E. Lyon, L. Jacobson,
Space Science 5, 969 (1965) .
2. E.M. Purcell, Phys. Rev. 54, 818 (1938) .
3. F.T. Rogers Jr., Rev. Sci. Instr. 22, 723 (1951) ;
see also references therein to earlier work of Rogers.
4. R.H. Ritchie, J.S. Cheka, R.D. Birkhoff,
Nucl. Instr. and Meth. 6, 157 (1960).
5. R.D. Birkhoff, J.M. Kohn, H.B. Eldridge, R.H. Ritchie,
Nucl. Instr. and Meth. 8, 313 (1960).
6. H.H. Hubbell, W.J. McConnell, R.D. Birkhoff,
Nucl. Instr. and Meth. 31, 18 (1964).
7. I.M. Minkov, Soviet Physics - Tech. Phys. 5, 1285 (1961).
8. V.V. Mel'nikov, I.A. Savenko, B.I. Savin, P.I. Shavrin,
Geomagnetism and Aeronomy 5, 107 (1965).
9. F.R. Paolini, R. Giacconi, J.R. Waters, L. Katz, D. Smart,
Space Research V, 466 (1965).
10. J.H. Coon, Radiation Trapped in the Earth's Magnetic Field,
(D. Reidel Publ. Co., Dordrecht, Holland, 1966) p. 231.
11. S.J. Bame, J.R. Asbridge, H.E. Felthausen, R.A. Olsen, I.B. Strong,
Phys. Rev. Letters 16, 138 (1966).
12. J.H. Wolfe, R.W. Silva, M.A. Myers,
J. Geophys. Res. 71, 1319 (1966).
13. M. Bader, T.B. Fryer, F.C. Witteborn, Two Instruments for Measuring
Distributions of Low Energy Charged Particles in Space,
NASA TND-1035 (1961).

14. L.A. Frank, Low Energy Proton and Electron Experiment for the
Orbiting Geophysical Observatories B and E,
State University of Iowa Publication 65-22 (1965) .
15. H. Goldstein, Classical Mechanics (Addison-Wesley Press, Inc,
Cambridge, Massachusetts, 1951) pp. 76-80 .
16. G.W. Goodrich, W.C. Wiley, Rev. Sci. Instr. 32, 846 (1961) .

Table I

Energy-Angle Response Matrix for Diffuse Beams

$\alpha \backslash T_{\infty}$	7.375	7.425	7.475	7.525	7.575	7.625	7.675	7.725	7.775	7.825	7.875	7.925	7.975	8.025	8.075	8.125	8.175	8.225	8.275	8.325	8.375	Sum
7.0	1	2	0	0	0	0	0	0	0	0	0	0	0	0	0	0	0	0	0	0	0	3
6.0	4	11	16	8	0	0	0	0	0	0	0	0	0	0	0	0	0	0	0	0	0	39
5.0	4	11	18	25	33	28	10	0	0	0	0	0	0	0	0	0	0	0	0	0	0	129
4.0	4	11	18	25	33	41	49	53	41	14	0	0	0	0	0	0	0	0	0	0	0	289
3.0	4	11	18	25	33	41	49	57	64	68	60	42	12	0	0	0	0	0	0	0	0	484
2.0	4	11	18	25	33	41	49	57	64	70	70	59	48	37	23	5	0	0	0	0	0	614
1.0	4	11	18	25	33	41	49	57	64	71	75	64	55	47	39	31	23	15	2	0	0	724
0	1	6	14	22	30	38	46	54	62	70	78	70	62	54	46	38	30	22	14	6	1	764
1.0	0	0	2	15	23	31	39	47	55	64	75	71	64	57	49	41	33	25	18	11	4	724
2.0	0	0	0	0	0	5	23	37	48	59	70	70	64	57	49	41	33	25	18	11	4	614
3.0	0	0	0	0	0	0	0	0	12	42	60	68	64	57	49	41	33	25	16	11	4	484
4.0	0	0	0	0	0	0	0	0	0	0	0	14	41	53	49	41	33	25	18	11	4	289
5.0	0	0	0	0	0	0	0	0	0	0	0	0	0	0	10	28	33	25	18	11	4	129
6.0	0	0	0	0	0	0	0	0	0	0	0	0	0	0	0	0	0	8	16	11	4	39
7.0	0	0	0	0	0	0	0	0	0	0	0	0	0	0	0	0	0	0	0	2	1	3
Sum	26	74	122	170	218	266	314	362	410	458	488	458	410	362	314	266	218	170	122	74	26	

Energy intervals are from $(T_{\infty} - 0.025)$ to $(T_{\infty} + 0.025)$ keV,
and angle intervals are from $(\alpha - 0.5)$ to $(\alpha + 0.5)$ deg.

TABLE II

Summary of Electrostatic Analyzer Characteristics

Particles Detected:	Electrons (e) and Protons (p) .
Detectors:	Bendix Magnetic Electron Multiplier .
Calibration Factor k :	6.68 .
Energy Range:	e-Mode, Low Range: 2 keV - 10 keV ;
(sequence as	e-Mode, High Range: 10 keV - 100 keV ;
shown) :	p-Mode, Low Range: 1 keV - 10 keV ;
	p-Mode, High Range: 10 keV - 100 keV .
Number of Energy Bins:	e-Mode, 8(low) + 8(high) = 16 ;
	p-Mode, 8(low) + 8(high) = 16 .
Energy Bin Interval:	35% .
Energy Bin Width:	$\Delta E_w / \bar{T}_\infty = 7.5\%$.
Angular Aperture:	7° . x 6.5° FWHM .
Geometrical Factor:	$1.0 \times 10^{-2} \text{ cm}^2\text{-ster}$.
Absolute Dynamic Range:	1×10^2 to $1 \times 10^9 / \text{cm}^2\text{-sec-ster-bin}$.
Counting Accuracy:	$\pm 5\%$ or statistical .
In Flight Calibration Means:	Fe ⁵⁵ (Auger electrons) .
Size:	Logic Box: 8-3/8 x 8 x 4 in. ³ ; Power Supply Box: 5 x 7 x 3 in. ³ .
Weight:	7.5 lb. + 5.4 lb. .
Power:	+28V, Unreg: 71 ma + 172 ma, 2.0 W + 4.8 W; +6.75V, Reg: 47 + 0 ma, 0.32 W; -6.75V, Reg: 28 + 0 ma, 0.19 W.
Output Signal Range:	0.0 to 5.0 V, Analog .
Output Impedence	3.0 K .
Output Lines:	Count Rate (Logarithmic Count Rate Meter), Counts (Scaler), Energy Signal , Energy Code , MEM HV Monitor .
External Pulse Requirements:	Switch Energy Level , Reset Scaler .

FIGURE CAPTIONS

Figure 1. Trajectories of transmitted particles in a hemispherical analyzer for an arbitrary point of incidence. Energy E is fixed and the angle of incidence α varies. T' and T'' are points of tangency of trajectories with plates and determine the allowable angular deviations $\Delta\alpha_+$ and $\Delta\alpha_-$ respectively. O is the center of curvature of the analyzer plates and of the unperturbed circular trajectory.

Figure 2. Trajectories of transmitted particles in a hemispherical analyzer for an arbitrary point of incidence. The angle of incidence α is fixed at 0° and the energy E varies. P' and P'' are points of intersection of trajectories with plates and determine the allowable deviations in major semi-axis Δa_+ and Δa_- respectively which thereby determine allowable energy deviations.

Figure 3. Locus^{of} centers of transmitted particle trajectories in an analyzer of arbitrary central angle ϕ_0 for an arbitrary point of incidence. C' and G' are points of tangencies of trajectories with analyzer plates and J and L are points of intersection. The locus is the total area within the curve $DEGHBCD$. The vertical displacement of any point within this area from AO is linearly proportional to the angle of incidence α of the particle whose trajectory center is that point. The horizontal displacement of that point from the normal to AO ^{at O} is linearly proportional to the energy deviation ΔE of the particle from the energy giving the unperturbed circular orbit. Scale factors are as given in the figure.

Figure 4. Dependence of the energy-angle factor on the central angle ϕ_0 of analyzer plates. The angular part only of the function $\langle \Delta\alpha \Delta E \rangle$ is plotted.

Figure 5. Experimental setup. A, pair of electrostatic analyzer plates mounted in a jig on the goniometer table. B, electron beam incident upon entrance aperture of electrostatic analyzer. C, electron gun control voltage supplies for filament, grid, and focussing electrode (accelerator). D, deflection voltage supplies for vertical and horizontal deflection plates of gun. E, commercial cathode ray tube electron gun. F, Faraday cup to catch current transmitted through analyzer plates. G, goniometer stepping motor and angle readout controls. I, Keithley Micro-microammeter (10^{-13} to 10^{-3} A range). M, stepping motor to drive goniometer table. O, ground plane located before electrostatic analyzer plates with apertures which match in width entrance and exit apertures defined by analyzer plate separation; the area around the entrance aperture is coated with phosphor. P1, electron gun post-accelerator voltage supply which defines the energy of electrons incident on analyzer plates; its range is -1 to -10 kV and calibration accuracy is $\pm 1\%$. P2, power supply for outer analyzer plate; its range is -0.5 to -6.0 kV and calibration accuracy is $\pm 0.25\%$. P3, power supply for inner analyzer plate; its range is 0 to +2 kV and calibration accuracy is $\pm 0.25\%$. R, visual readout unit for goniometer table. V, vacuum chamber containing gun, analyzer plates, and goniometer assembly; pressure is less than 10^{-5} Torr with a liquid nitrogen cold trap. W, lead glass viewing ports. Z, an electrical feed-through into vacuum chamber; similar symbols indicate others.

Figure 6. Experimental transmission functions of electrostatic analyzer for a fine electron beam incident at the center of the entrance aperture. In 6a, the angle of incidence α is fixed and energy E varies. In 6b, the energy E is fixed and the angle of incidence α varies. Notice the sharpness of the cutoffs; tails beyond the cutoffs are due to particle scattering.

Figure 7. Energy-angle transmission diagrams for a fine electron beam. For the various positions of beam incidence indicated solid closed curves are

theoretical diagram shapes and the data points are the experimentally determined values of E and α for which particle transmission falls to 50%. Values δE and $\delta \alpha$ are amounts by which the indicated sets of data points have been translated to give best fit to the theoretical curves; such values are consistent with the magnitudes of experimental errors expected. What should be noted is that the shapes (rather than the centroids) of theoretical and experimental transmission diagrams agree well.

Figure 8. Energy response functions for unidirectional diffuse electron beams.

A "diffuse beam" in this context is one which irradiates the total area of the entrance aperture. The functions are plots of the rows of Table I, the Energy-Angle Response Matrix, which was derived from directly measured smoothed and from interpolated transmission diagram data of Figure 7. Functions are given for various angular intervals of limits ($\alpha - 0.5$) to ($\alpha + 0.5$) degrees. The ordinate scale is arbitrary.

Figure 9. Angle response functions for mono-energetic diffuse electron beams.

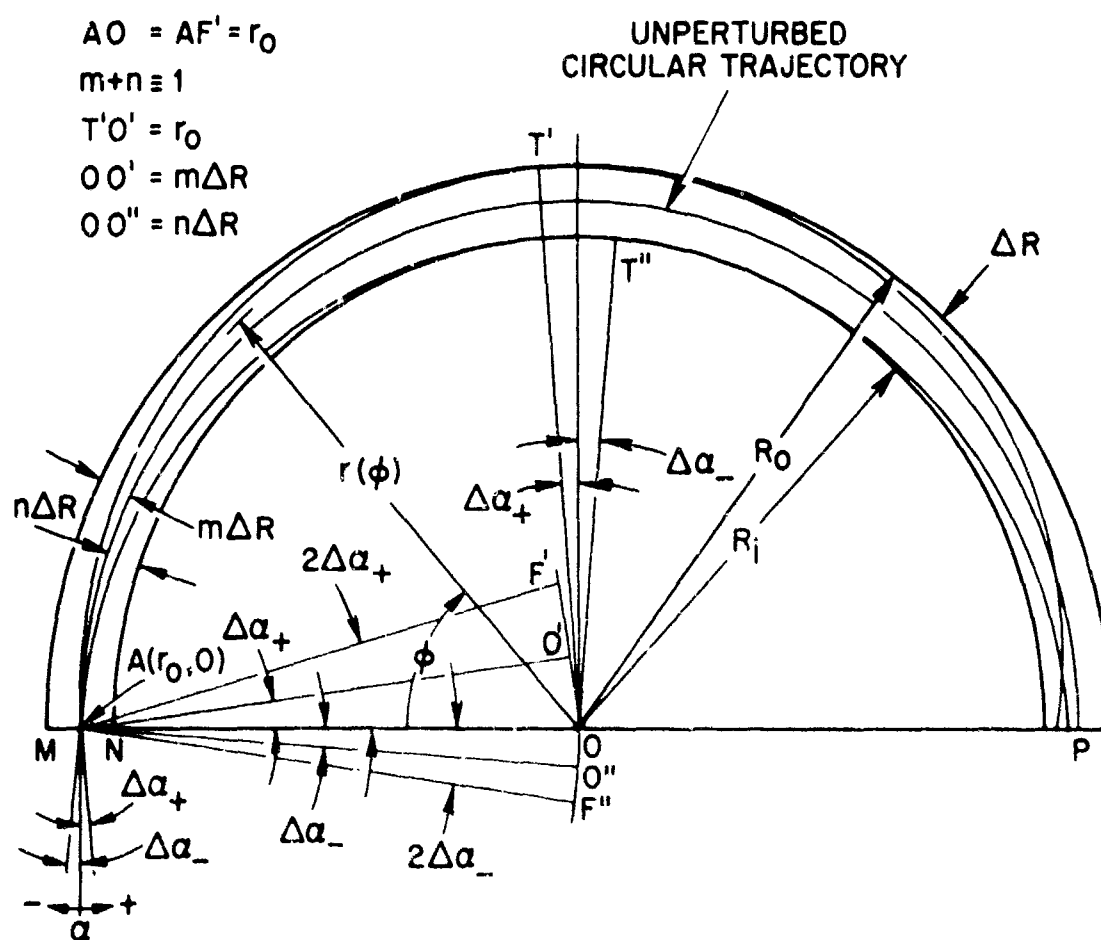
The functions are plots of the columns of Table I and are given for various energy intervals of limits ($T_{\infty} - 0.025$) to ($T_{\infty} + 0.025$) keV. The ordinate scale is arbitrary.

Figure 10. Integrated response functions for diffuse electron beams. The energy response function, shown in 10a, is a plot of the sums of columns of Table I (equivalent to integrating over angle) and gives the relative response of the instrument to radiation that is independent of angle within the narrow angular aperture of the instrument. The angle response function, shown in 10b, is a plot of the sums of rows of Table I (equivalent to integrating over energy) and gives the relative response of the instrument to radiation which has a flat spectrum over the range of energies for which transmission is non-zero. Notice that the widths of the functions at half-maximum response (FWHM) are equal to the widths of the functions in Figure 6 (giving responses to fine beams) but that detailed shapes are much different.

Figure 11. Block diagram of electrostatic analyzer. Numbers on input and output lines are connector pin numbers. T on the amplifier output line represents an internal test point used during calibration. M denotes modular electronic units, i.e., those used on other kinds of space instruments. Abbreviations are: MEM, magnetic electron multiplier; HV, high voltage; PS, power supply; MON, monitor; SS, single-shot circuit; LCRM, logarithmic count rate meter; DAC, digital-to-analog converter; REF, reference voltage; XFR, transformer coupling; REG, regulated; RET, power return; PHVPS, programmable high voltage power supply; RPC, range and polarity control; SC, scaler; SM, switching matrix; COMM, commutator.

TRAJECTORIES OF TRANSMITTED PARTICLES

ENERGY E FIXED, ANGLE OF INCIDENCE α VARYING



TRAJECTORIES OF TRANSMITTED PARTICLES

ANGLE OF INCIDENCE $\alpha=0$, ENERGY E VARYING

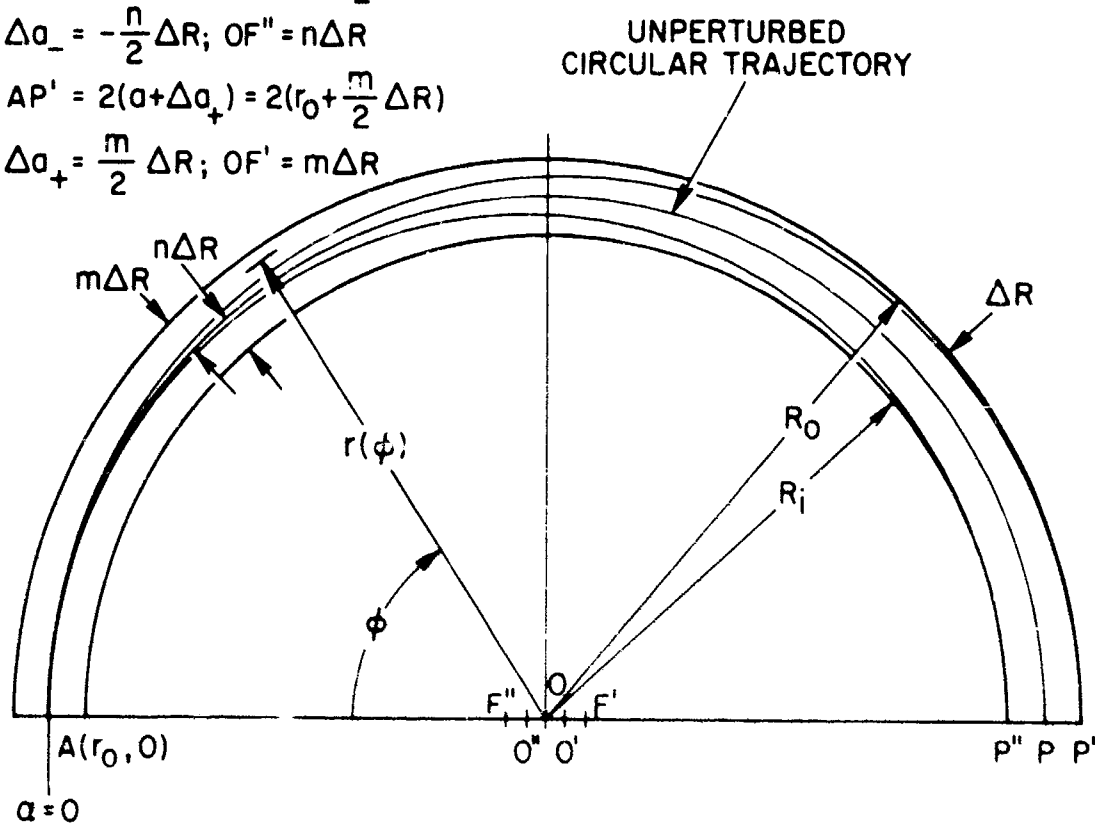
$$AP \equiv 2a = 2r_0$$

$$AP'' = 2(a + \Delta a_-) = 2(r_0 - \frac{n}{2} \Delta R)$$

$$\Delta a_- = -\frac{n}{2} \Delta R; OF'' = n\Delta R$$

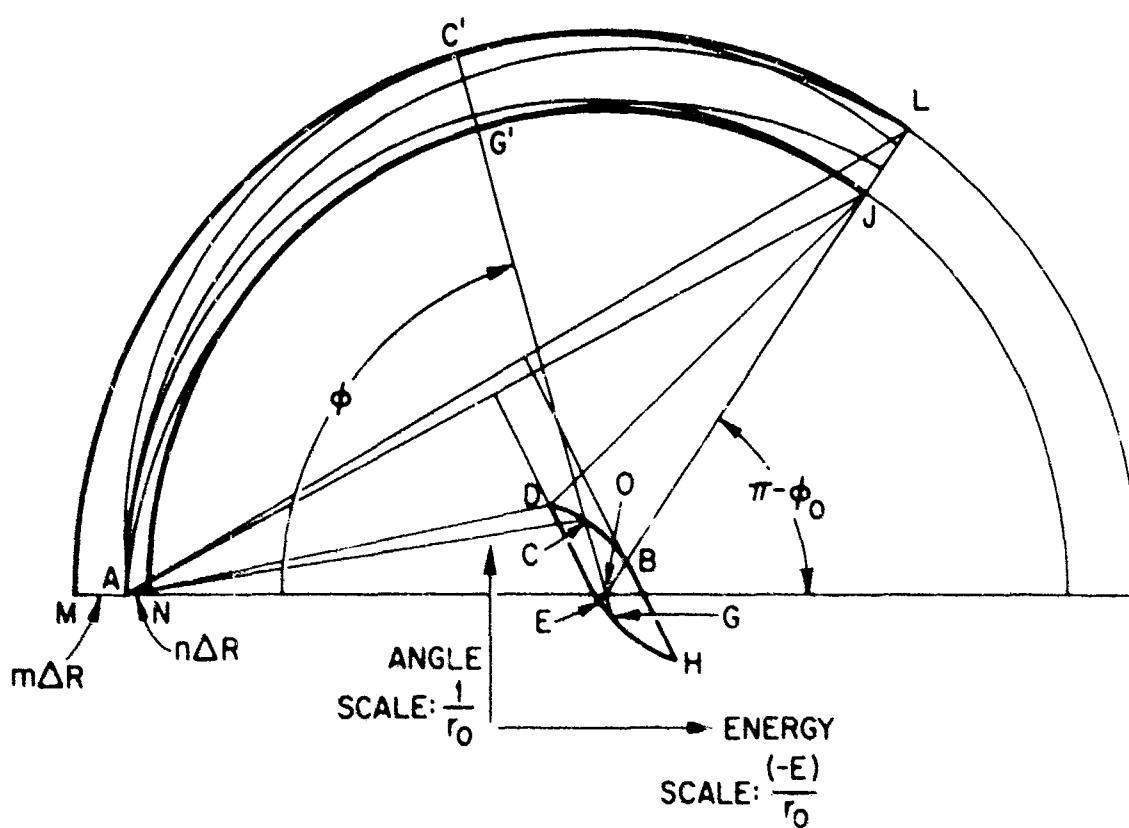
$$AP' = 2(a + \Delta a_+) = 2(r_0 + \frac{m}{2} \Delta R)$$

$$\Delta a_+ = \frac{m}{2} \Delta R; OF' = m\Delta R$$

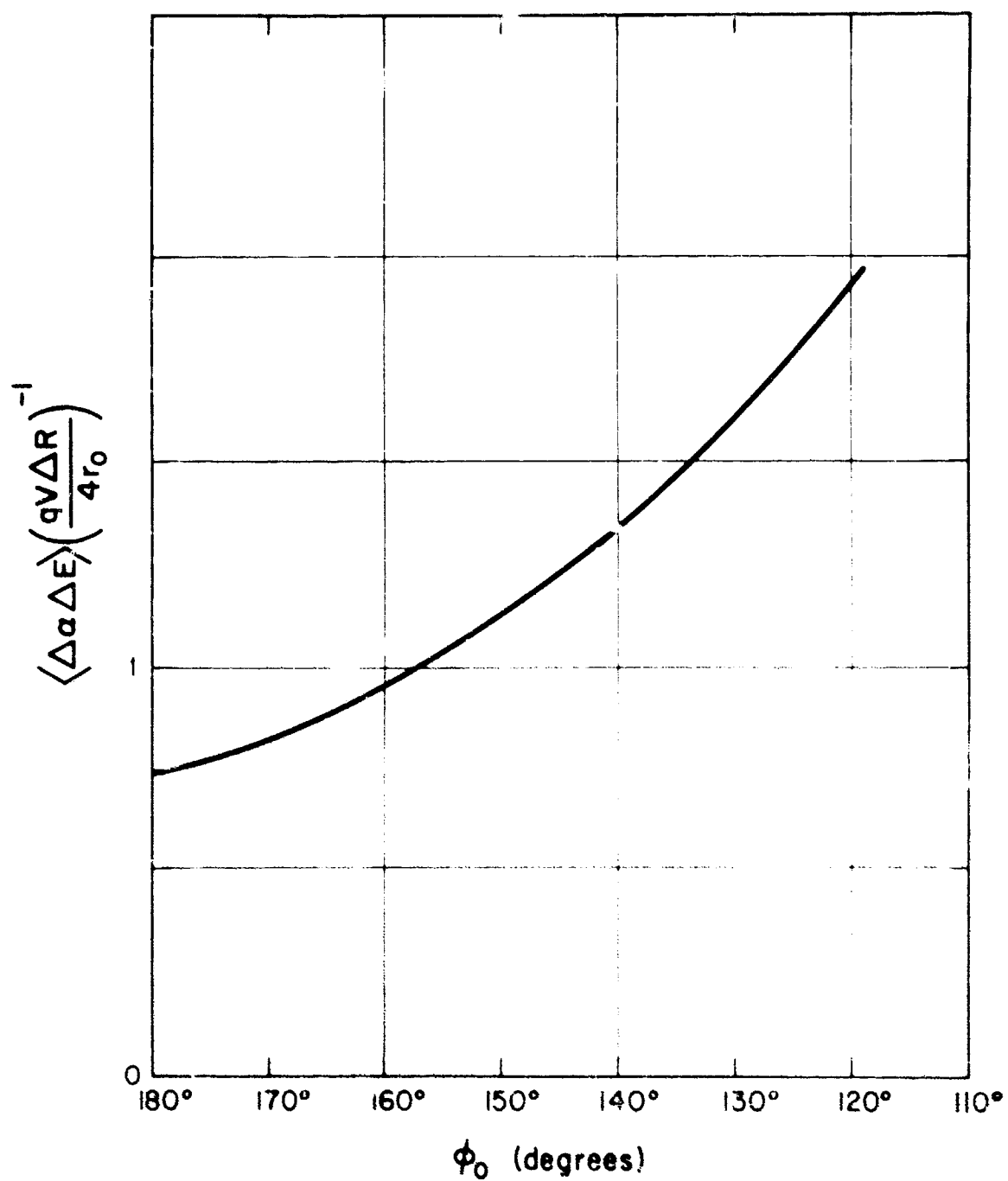


LOCUS OF ALLOWED TRAJECTORY CENTERS

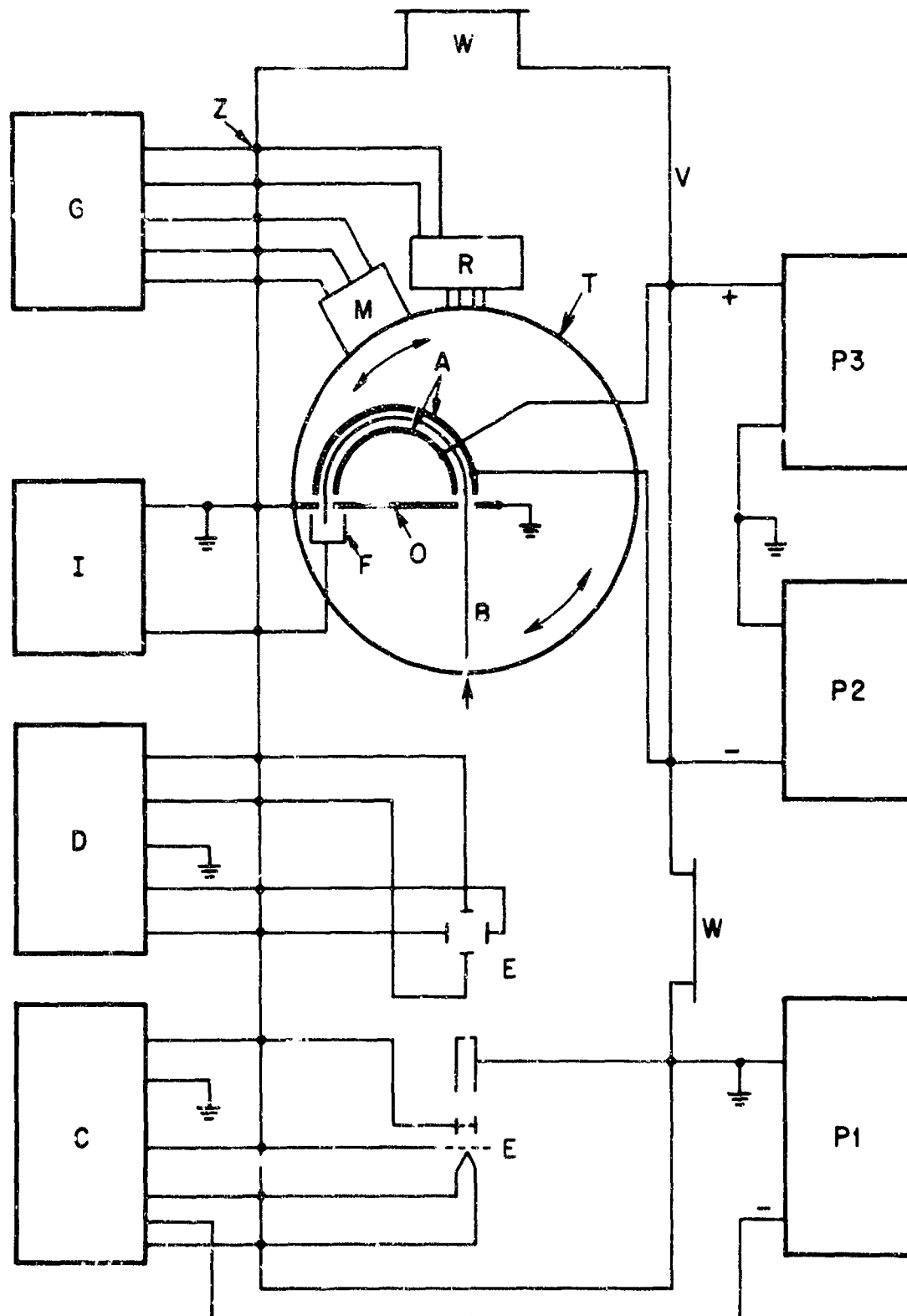
ARBITRARY POINT OF INCIDENCE



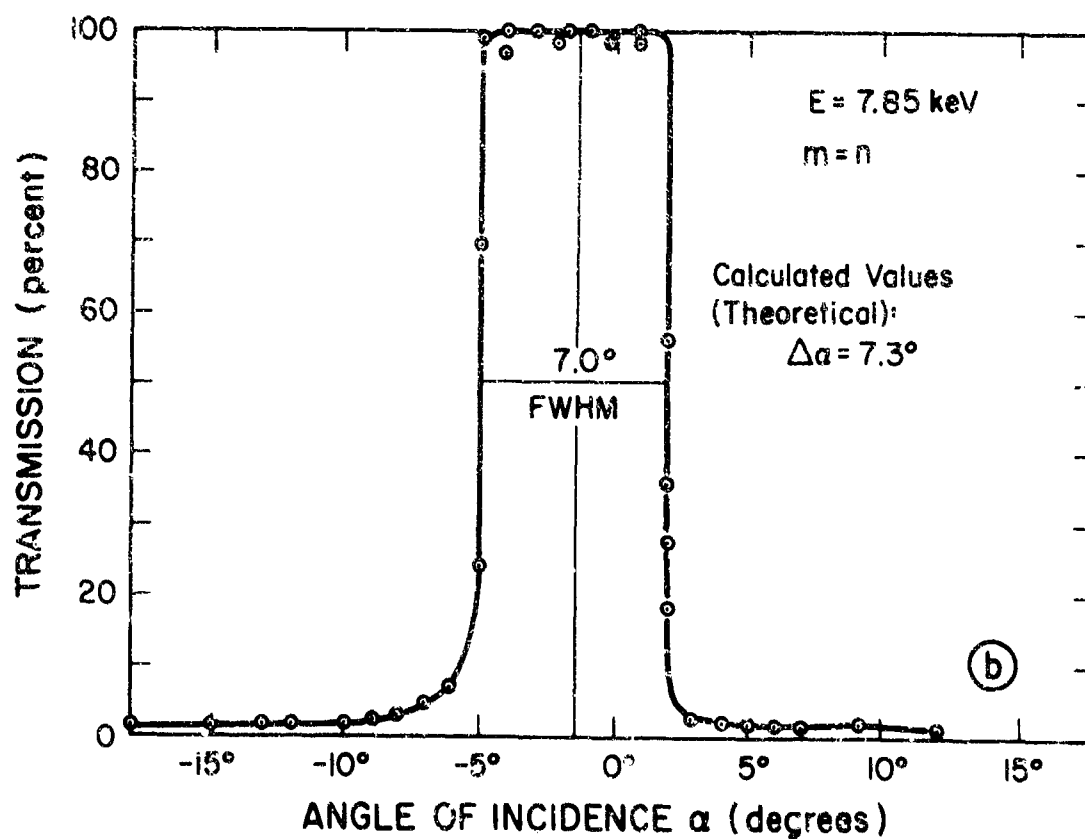
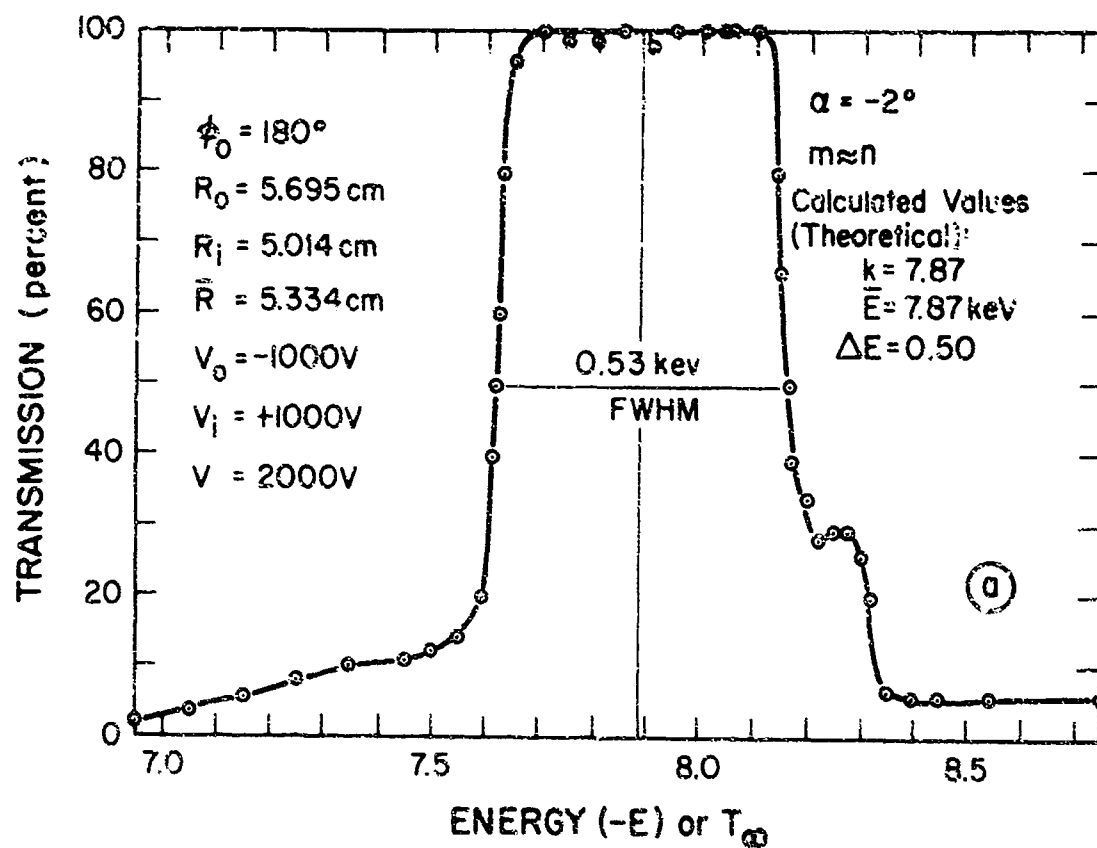
DEPENDENCE OF GEOMETRICAL-ENERGY FACTOR ON ANALYZER PLATE CENTRAL ANGLE



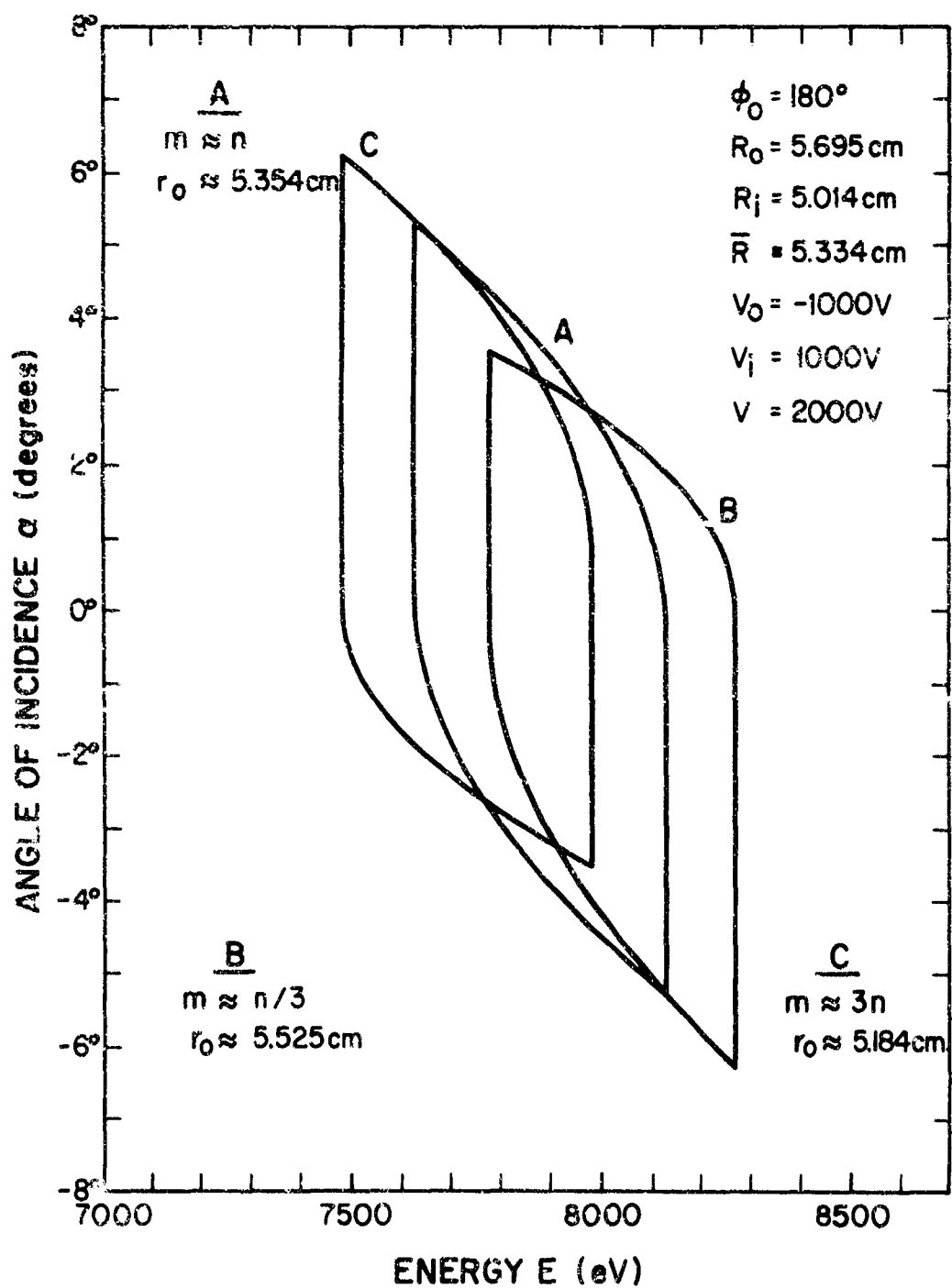
EXPERIMENTAL SETUP



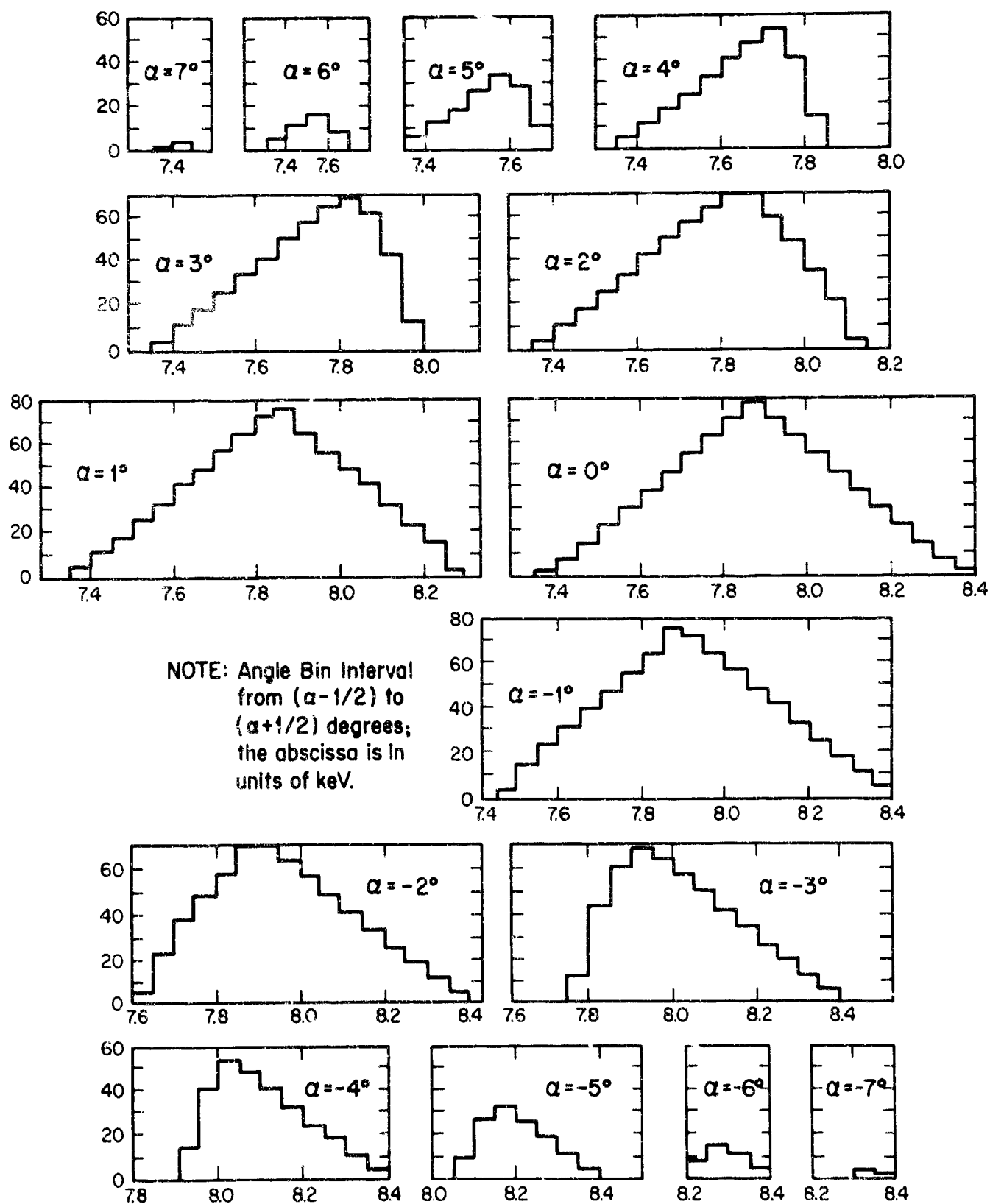
TRANSMISSION OF ELECTROSTATIC ANALYZER



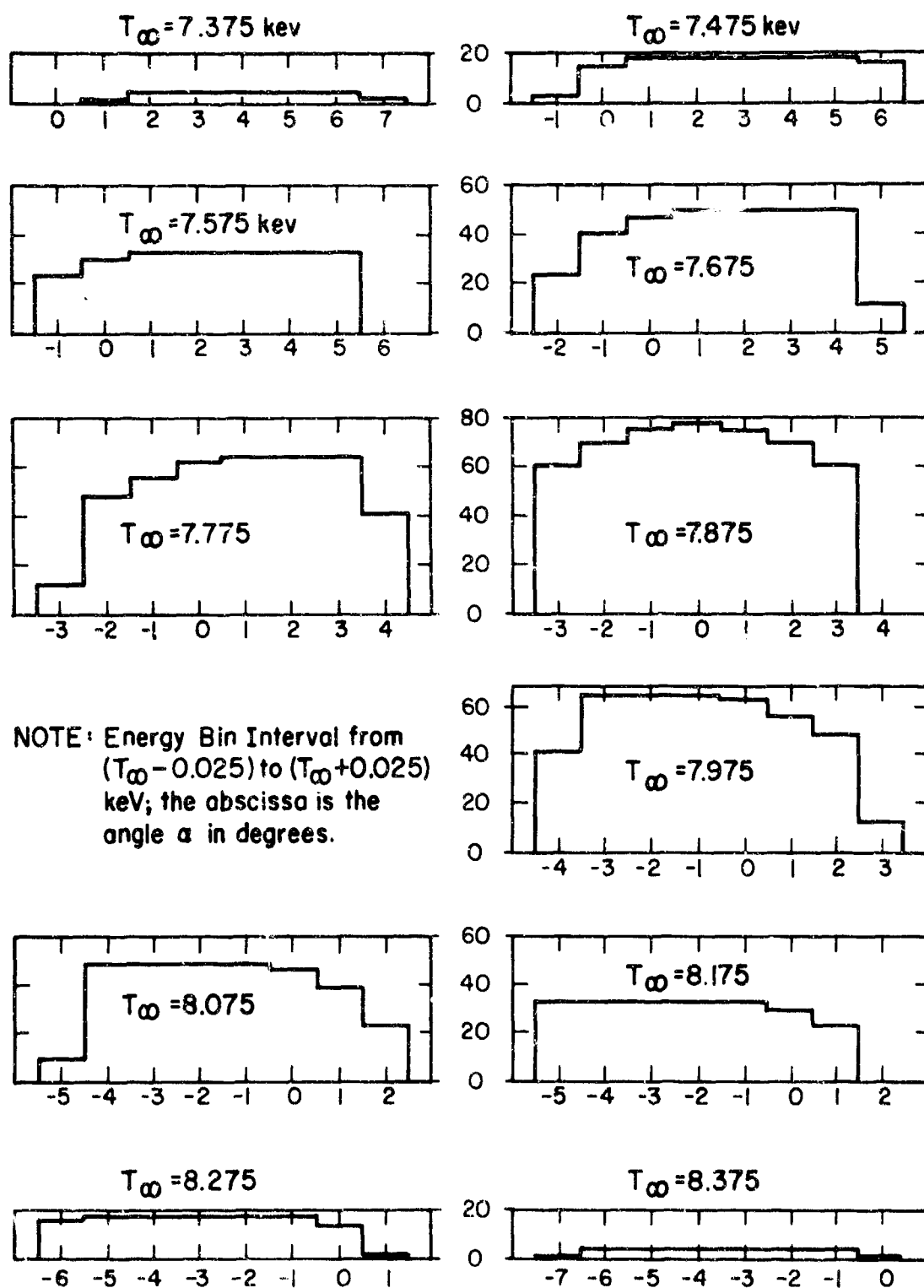
ENERGY-ANGLE TRANSMISSION DIAGRAMS FOR THE ELECTROSTATIC ANALYZER



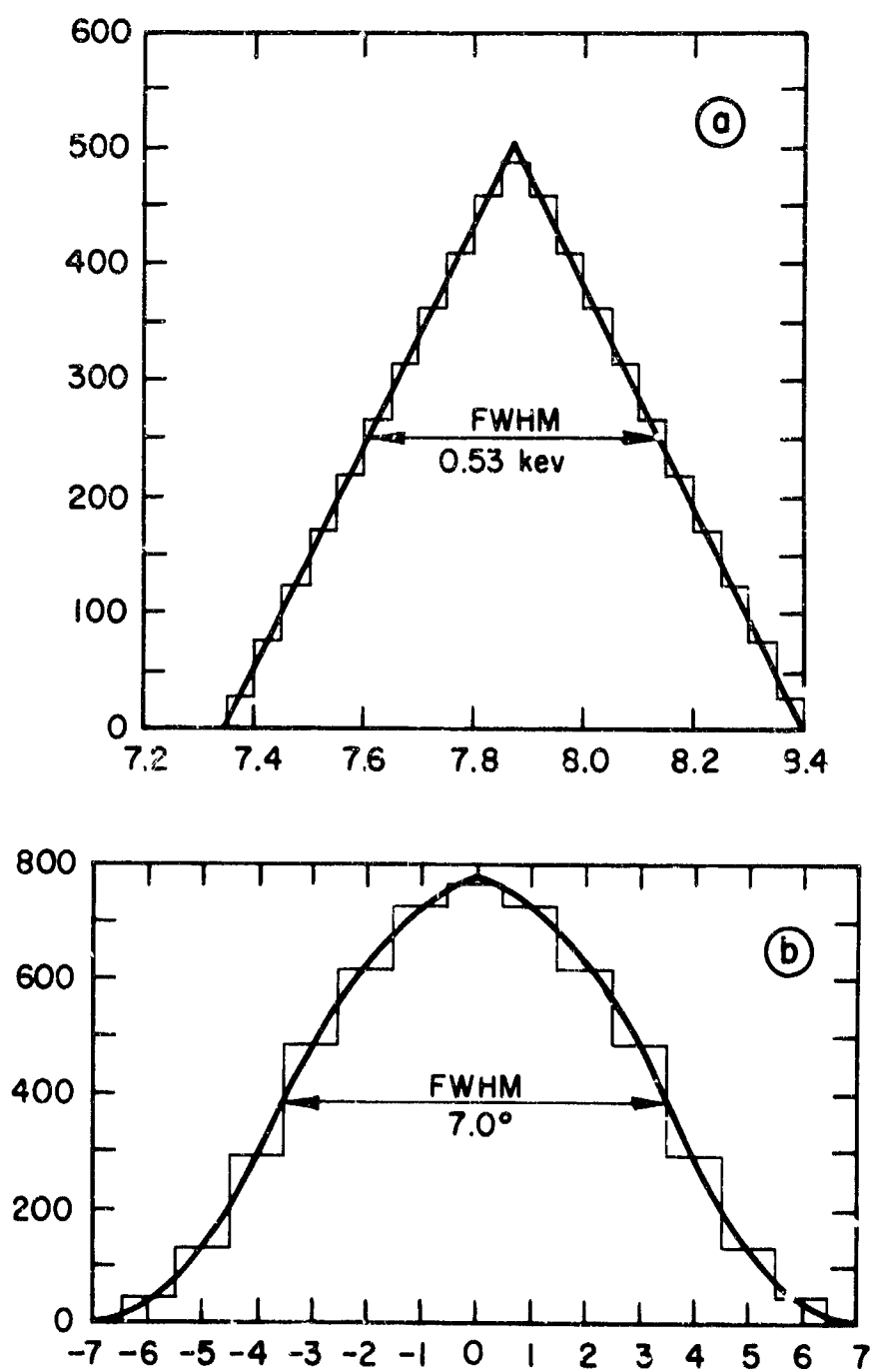
ENERGY RESPONSE FUNCTIONS



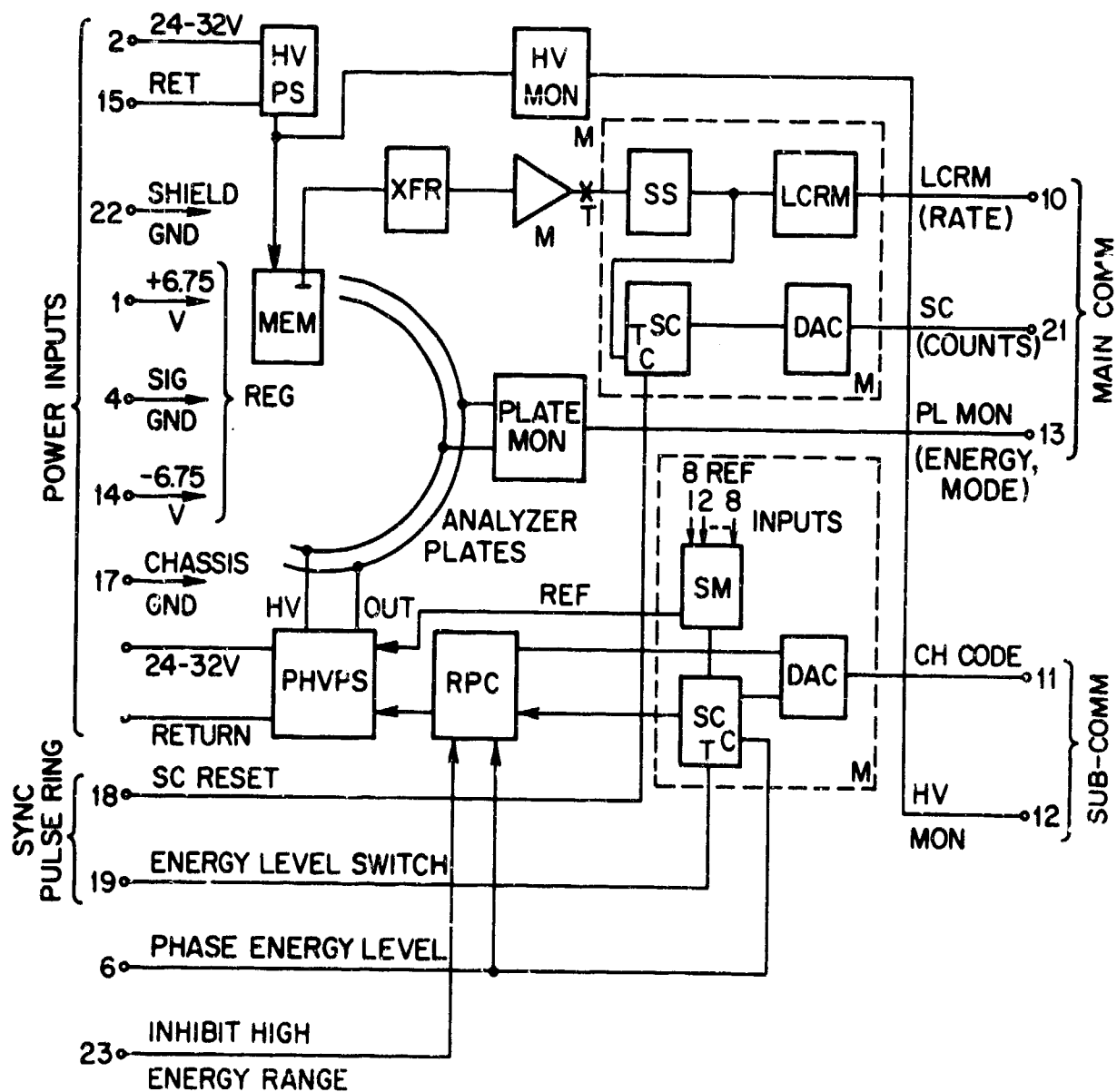
ANGLE RESPONSE FUNCTIONS



INTEGRATED RESPONSE FUNCTIONS



BLOCK DIAGRAM OF ELECTROSTATIC ANALYZER



Unclassified

Security Classification

DOCUMENT CONTROL DATA - R&D		
(Security classification of title, body of abstract and indexing annotation must be entered when the overall report is classified)		
1. ORIGINATING ACTIVITY (Corporate author) American Science and Engineering, Inc. 11 Carleton Street Cambridge, Massachusetts 02142		2a. REPORT SECURITY CLASSIFICATION Unclassified
		2b. GROUP
3. REPORT TITLE RESEARCH DIRECTED TOWARD THE STUDY AND ANALYSIS OF ELECTROSTATIC ANALYZER DATA		
4. DESCRIPTIVE NOTES (Type of report and inclusive dates) Scientific. Final. 5 March 1968 - 15 July 1969		Approved 11 December 1969
5. AUTHOR(S) (First name, middle initial, last name) William P. Reidy		
6. REPORT DATE 15 August 1969	7a. TOTAL NO. OF PAGES 185	7b. NO. OF REFS 11
8a. CONTRACT OR GRANT NO. F19628-68-C-0287	9a. ORIGINATOR'S REPORT NUMBER(S) ASE-2255	
b. PROJECT, TASK, WORK UNIT NOS. 000D-63-01, 5710		
c. DOD ELEMENT 6143001F, 6164601H	9b. OTHER REPORT NO(S) (Any other numbers that may be assigned this report)	
d. DOD SUBELEMENT 680100	AFCRL-69-0369	
10. DISTRIBUTION STATEMENT 1 - This document has been approved for public release and sale: its distribution is unlimited.		
11. SUPPLEMENTARY NOTES This research was supported in part by the Defense Atomic Support Agency and in part by the Air Force In-House Laboratory Independent Research Fund.		12. SPONSORING MILITARY ACTIVITY Air Force Cambridge Research Laboratories (CRP) L.G. Hanscom Field Bedford, Massachusetts 01730
13. ABSTRACT Section I - The OV3-2 satellite was instrumented with two electron electrostatic analyzers to measure the auroral electron spectrum between 10 and 100 kev, the electron pitch angle distribution, and the precipitated electron flux. The design and calibration of these instruments are documented. Initially the satellite measurements were tape recorded and played back at selected recording stations. After failure of the recording and playback system, real time recordings were made at Churchill and Thule. The analysis of this data is presented: including spectral form, spatial distribution, and limited pitch angle distributions. Section II - Aerobee rocket 15.735 was instrumented with a high resolution ($\Delta E = 10$ eV, rapid (300 milliseconds per energy sweep) to measure the auroral electron spectrum between 2 and 35 kev and a thin window ionization chamber to measure the total energy deposition. The rocket was launched during the breakup of a visible aurora and penetrated a diffuse auroral region. The energy spectra temporal variation, and the variation in pitch angle distribution as a function of energy are presented.		

DD FORM 1473
1 NOV 65

Unclassified

Security Classification

Unclassified

Security Classification

14.	KEY WORDS	LINK A		LINK B		LINK C	
		ROLE	WT	ROLE	WT	ROLE	WT
	Aurora Precipitated Electrons Electron Spectra Pitch Angle Distribution						

Unclassified

Security Classification